


Cite this: *Chem. Sci.*, 2024, 15, 7870

# Advances and challenges in the electrochemical reduction of carbon dioxide

Jingyi Han, Xue Bai, Xiaoqin Xu, Xue Bai, Anaer Husile, Siying Zhang, Luoluo Qi and Jingqi Guan \*

The electrocatalytic carbon dioxide reduction reaction (ECO<sub>2</sub>RR) is a promising way to realize the transformation of waste into valuable material, which can not only meet the environmental goal of reducing carbon emissions, but also obtain clean energy and valuable industrial products simultaneously. Herein, we first introduce the complex CO<sub>2</sub>RR mechanisms based on the number of carbons in the product. Since the coupling of C–C bonds is unanimously recognized as the key mechanism step in the ECO<sub>2</sub>RR for the generation of high-value products, the structural–activity relationship of electrocatalysts is systematically reviewed. Next, we comprehensively classify the latest developments, both experimental and theoretical, in different categories of cutting-edge electrocatalysts and provide theoretical insights on various aspects. Finally, challenges are discussed from the perspectives of both materials and devices to inspire researchers to promote the industrial application of the ECO<sub>2</sub>RR at the earliest.

Received 22nd March 2024

Accepted 30th April 2024

DOI: 10.1039/d4sc01931h

rsc.li/chemical-science

## 1. Introduction

In the late 2023, the 28th United Nations Climate Change Conference (COP28) conducted the first “global carbon inventory” of the world’s efforts to address climate change.<sup>1</sup> The parties unanimously decided to accelerate the pace of reducing greenhouse gas emissions by 2030,<sup>2</sup> calling on governments to advance the effective implementation of carbon reduction actions to achieve the ultimate goal of the Paris Agreement as soon as possible,<sup>3</sup> *i.e.*, in addition to natural autonomous pathways such as bioenergy with carbon capture and storage (BECCS), industrial technologies of carbon capture, utilization and storage (CCUS) are to be eagerly promoted alternatively.<sup>4</sup> With the depletion of traditional fossil fuels, the energy crisis has become an extreme urgency.<sup>5</sup>

As an ideal solution, the electrocatalytic carbon dioxide reduction reaction (ECO<sub>2</sub>RR) can not only end the artificial carbon cycle, but also convert renewable power such as solar energy and wind energy into beneficial chemical energy products, including clean fuels and industrial raw materials to achieve a virtuous cycle of turning waste into treasure as a whole.<sup>6–9</sup> However, as depicted in Fig. 1, to date, the related research in the field of ECO<sub>2</sub>RRs is still in the emerging stage, which is far from mature compared with other electrochemical technologies such as hydrogen production through the electrolysis of water, and the prerequisite for its practical application is a robust catalyst with high electrochemical activity and

high selectivity toward the target product.<sup>10–13</sup> Noteworthy, the complexity of the reaction mechanism of the CO<sub>2</sub>RR should not be underestimated, and a large number of studies have confirmed that the C–C coupling step is crucial for the advancement of the ECO<sub>2</sub>RR and has a high degree of structural sensitivity.<sup>14–17</sup> Therefore, the in-depth exploration of the influence of the electronic structure of materials on the ECO<sub>2</sub>RR catalytic performance has always been the main direction of researchers.

In this review, the reaction mechanisms of the ECO<sub>2</sub>RR are first classified based on the number of carbon atoms in the products. On this basis, we thoroughly discuss the profound insights gained on the structure–activity relationship, and the most cutting-edge catalysts reported in recent years have been comprehensively reviewed according to the detailed categories, including atomically-dispersed catalysts, alloys, metal–organic frameworks (MOFs) and covalent organic frameworks (COFs). In terms of theoretical calculations, authoritative opinions are representatively classified. Finally, we analyze the remaining challenges from both the material and device perspectives, with a view to inspire researchers to help pave a new stage in the field of ECO<sub>2</sub>RR.

## 2. ECO<sub>2</sub>RR mechanisms

In the process of carbon dioxide reduction, due to the extremely high stability of C=O chemical bonds and the competition of hydrogen evolution reaction (HER), the carbon dioxide reduction process faces major challenges, which seriously hinders the effective implementation.<sup>18–20</sup> Therefore, it is urgent to design

Institute of Physical Chemistry, College of Chemistry, Jilin University, Changchun 130021, PR China. E-mail: guanjq@jlu.edu.cn



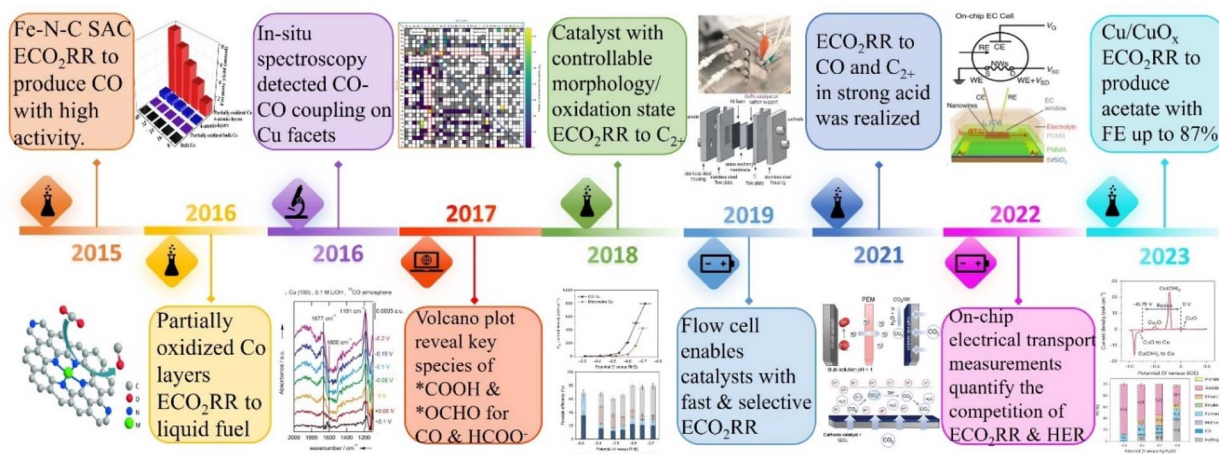


Fig. 1 Timeline of the major developments in the ECO<sub>2</sub>RR.

an efficient catalyst to overcome the high activation energy barrier. However, although there are more and more experimental and theoretical studies on various catalysts, the available catalysts need to have a large overpotential for specific products, and their selectivity is usually very low. On different catalysts under different conditions, different products will be produced, such as CO, formate, methane and ethanol.<sup>21</sup> In addition, the electrochemical CO<sub>2</sub>RR process involves multi-electron transfer processes, and the product is very complex, making the subsequent product separation and purification processes very difficult. Therefore, it is important to understand the reaction mechanism and reaction intermediates, which is related to the design and modification of catalysts.<sup>22</sup> Table 1 lists the half-reactions that may occur on the cathode surface during the electrochemical reduction of CO<sub>2</sub> and their equilibrium potentials relative to the standard hydrogen electrode (SHE) in electrolytes at pH 7.<sup>19</sup>

Theoretical calculations and modeling can provide information such as binding energy, free energy and activation energy of the intermediates, which is helpful to evaluate the feasibility of each reaction step of the synthesized catalyst and screen out the key intermediates conducive to the reaction.<sup>23</sup>

**Table 1** The possible half-reactions on the surface of the cathode during the electrochemical reduction of CO<sub>2</sub> and their equilibrium potential relative to SHE in the electrolyte at pH 7

CO <sub>2</sub> reduction half reaction	The equilibrium potential relative to SHE at pH 7
CO <sub>2</sub> + 2H <sup>+</sup> + 2e <sup>-</sup> → HCOOH + H <sub>2</sub> O	$E_{\text{redox}}^0 = -0.610 \text{ V}$
CO <sub>2</sub> + 2H <sup>+</sup> + 2e <sup>-</sup> → CO + H <sub>2</sub> O	$E_{\text{redox}}^0 = -0.530 \text{ V}$
2CO <sub>2</sub> + 2H <sup>+</sup> + 2e <sup>-</sup> → H <sub>2</sub> C <sub>2</sub> O <sub>4</sub>	$E_{\text{redox}}^0 = -0.913 \text{ V}$
CO <sub>2</sub> + 4H <sup>+</sup> + 4e <sup>-</sup> → HCHO + H <sub>2</sub> O	$E_{\text{redox}}^0 = -0.480 \text{ V}$
CO <sub>2</sub> + 6H <sup>+</sup> + 6e <sup>-</sup> → CH <sub>3</sub> OH + H <sub>2</sub> O	$E_{\text{redox}}^0 = -0.380 \text{ V}$
CO <sub>2</sub> + 8H <sup>+</sup> + 8e <sup>-</sup> → CH <sub>4</sub> + 2H <sub>2</sub> O	$E_{\text{redox}}^0 = -0.240 \text{ V}$
2CO <sub>2</sub> + 12H <sup>+</sup> + 12e <sup>-</sup> → C <sub>2</sub> H <sub>4</sub> + 4H <sub>2</sub> O	$E_{\text{redox}}^0 = -0.349 \text{ V}$
2CO <sub>2</sub> + 12H <sup>+</sup> + 12e <sup>-</sup> → C <sub>2</sub> H <sub>5</sub> OH + 3H <sub>2</sub> O	$E_{\text{redox}}^0 = -0.329 \text{ V}$
2CO <sub>2</sub> + 14H <sup>+</sup> + 14e <sup>-</sup> → C <sub>2</sub> H <sub>6</sub> + 4H <sub>2</sub> O	$E_{\text{redox}}^0 = -0.270 \text{ V}$
3CO <sub>2</sub> + 18H <sup>+</sup> + 18e <sup>-</sup> → C <sub>3</sub> H <sub>7</sub> OH + H <sub>2</sub> O	$E_{\text{redox}}^0 = -0.310 \text{ V}$
2H <sup>+</sup> + 2e <sup>-</sup> → H <sub>2</sub>	$E_{\text{redox}}^0 = -0.42 \text{ V}$

Electrochemical reduction method is one of the key means to determine the reaction intermediates. Pure metals such as Al, Fe, Ni, Pt and Ti can reduce CO<sub>2</sub> to CO, but the HER rate during the reduction process is much higher than the reduction rate of CO<sub>2</sub>, while Ag, Au and Zn will produce CO with high current efficiency.<sup>24</sup> Formate is the main product of the catalytic reduction on metals such as Hg, In and Sn.<sup>25</sup> Cu-based catalysts can reduce CO<sub>2</sub> to hydrocarbons and alcohols. Fig. 2 shows the mechanism of CO<sub>2</sub>RR on metal electrocatalysts.<sup>26</sup> This section introduces the main mechanisms of electroreduction of CO<sub>2</sub> to HCOOH/HCOO<sup>-</sup>, CO, HCHO, CH<sub>3</sub>OH, CH<sub>4</sub>, C<sub>2</sub>H<sub>4</sub>, CH<sub>3</sub>CH<sub>2</sub>OH and CH<sub>3</sub>CH<sub>2</sub>CH<sub>2</sub>OH.

## 2.1. Reduction of CO<sub>2</sub> to C<sub>1</sub> products

The products of CO<sub>2</sub> reduction to C<sub>1</sub> include HCOOH/HCOO<sup>-</sup>, CO, HCHO, CH<sub>3</sub>OH and CH<sub>4</sub>.<sup>27–31</sup> The formation of HCOOH/HCOO<sup>-</sup> can be divided into three steps. First, CO<sub>2</sub> molecules are inserted into the metal–hydrogen bond and then combined with one or two oxygen atoms to the metal electrode, followed by further protonation to form formate (Fig. 3a).<sup>32</sup> Second, the surface hydroxyl group reacts with CO<sub>2</sub> to form a carbonate intermediate, thereby forming HCOO<sup>-</sup> (Fig. 3b).<sup>33</sup> Finally, \*CO<sub>2</sub><sup>-</sup> radicals react with adjacent water molecules to form formate/formate salts (Fig. 3c).<sup>34</sup> The reduction of CO<sub>2</sub> to CO is carried out by forming \*COOH intermediates. The \*COOH intermediate is formed by the proton coupling of \*COO<sup>-</sup>, electron transfer or single electron transfer, and then protonation. Further, proton-coupled electrons are transferred to the adsorbed \*COOH intermediate, resulting in dissociation to form CO (Fig. 3d). Hansen *et al.* found that \*COOH was reduced to \*CO, but it was inhibited by the first step of weak COOH binding.<sup>35</sup> The formation of HCHO, CH<sub>3</sub>OH and CH<sub>4</sub> is carried out by the transfer of 4, 6 and 8 electrons, respectively. The initial \*CO is converted to \*CHO, \*CH<sub>2</sub>O and \*CH<sub>3</sub>O by hydrogenation, and \*CH<sub>3</sub>O is further hydride oxygenated to CH<sub>4</sub>,<sup>36</sup> which can also be produced by the multi-step hydrogenation of \*COH. \*CH<sub>2</sub>O is desorbed to form HCHO, and \*CH<sub>3</sub>O is hydrogenated to CH<sub>3</sub>OH (Fig. 3e).<sup>37</sup>



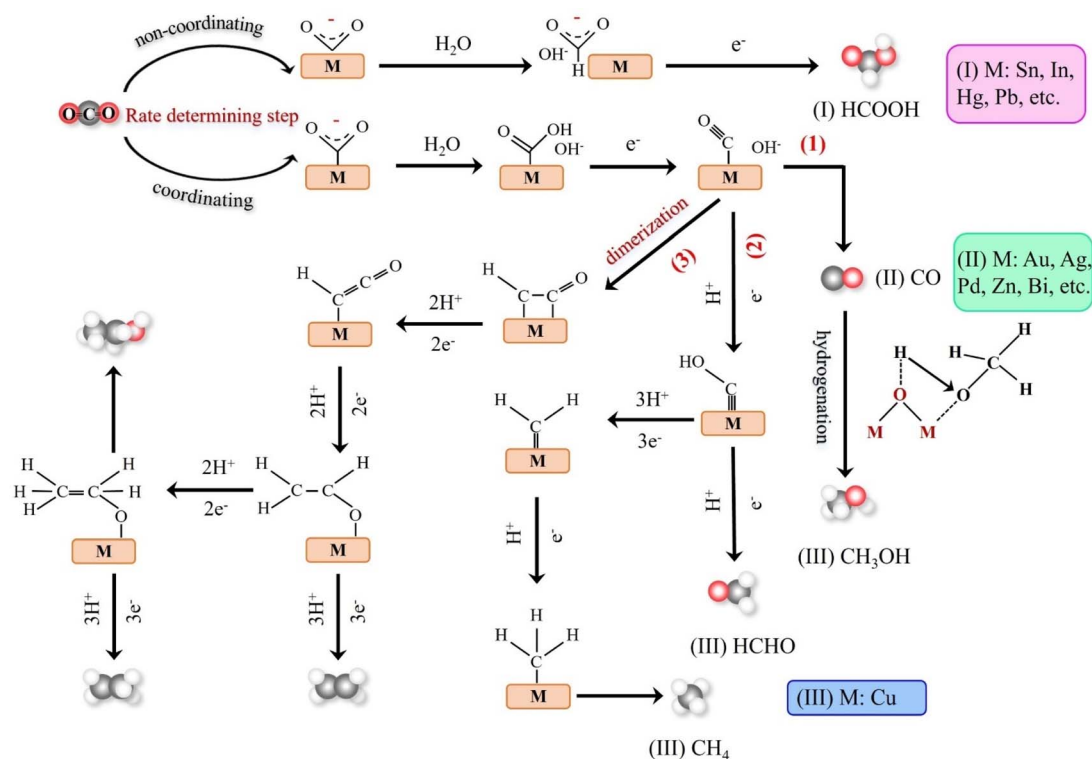


Fig. 2 Schematic mechanism of various metal electrocatalysts for the CO<sub>2</sub>RR.

## 2.2. Reduction of CO<sub>2</sub> to C<sub>2</sub> products

C<sub>2</sub> products mainly include C<sub>2</sub>H<sub>4</sub>, CH<sub>3</sub>CHO and CH<sub>3</sub>CH<sub>2</sub>-OH.<sup>38–40</sup> At low negative potentials, the formation of C<sub>2</sub> products is a complex process with multiple reaction pathways. Nie *et al.* proposed that the formation of C<sub>2</sub>H<sub>4</sub> is the result of the coupling of two \*CH<sub>2</sub> intermediates or the insertion of CO in the Fischer-Tropsch-like step.<sup>41</sup> Another pathway is that the \*CO intermediate is dimerized to form the \*C<sub>2</sub>O<sub>2</sub> intermediate, which is then transformed into \*COCHO by electron transfer and finally hydride oxygenated to form C<sub>2</sub>H<sub>4</sub>.<sup>42</sup> The formation of CH<sub>3</sub>CH<sub>2</sub>OH has the same reaction intermediate as C<sub>2</sub>H<sub>4</sub>. Researchers proposed that \*CHO dimerization is the main pathway of ethanol on Cu (100) at low potentials.<sup>43</sup> The intermediate of vinyl alcohol can be further reduced to C<sub>2</sub>H<sub>4</sub> or CH<sub>3</sub>CHO and C<sub>2</sub>H<sub>5</sub>OH (Fig. 4).

## 2.3. Reduction of CO<sub>2</sub> to C<sub>3</sub> products

The reduction of CO<sub>2</sub> to C<sub>3</sub> long-chain products (such as propanol) has always been a difficult problem to overcome.<sup>44</sup> When CO<sub>2</sub> is reduced to propanol, the following steps may be carried out. The adsorbed C<sub>2</sub> intermediate undergoes a C–C coupling reaction with adjacent C<sub>1</sub> intermediate, followed by proton or electron transfer to produce propionaldehyde, which is finally reduced to propanol (Fig. 5).<sup>45</sup> Although C<sub>2+</sub> products are eagerly awaited due to their peak economic value, the generation of C<sub>2+</sub> by ECO<sub>2</sub>RR remains challenging at this stage. Table 2 lists the formation rates and FEs obtained so far for different C<sub>2+</sub> products to provide a more comprehensive overview.

## 3. Structure–activity relationships

The electronic structure of the catalyst is key to optimizing the catalytic processes that fundamentally dominate their various electrocatalytic properties, including activity, selectivity, and stability.<sup>62–65</sup> Therefore, the structure–performance relationship of the catalyst as the core of electrocatalysis is of great significance. However, the factors affecting the electronic state of the catalytic center are complicated. The combination of active metal elements, defect site engineering and coordination environment optimization between adjacent atoms have been developed as the main means to effectively regulate the electronic structure.<sup>66–68</sup> The in-depth understanding about the structure–performance relationship not only broadens the way for the rational development of new catalytic materials with more potential and pertinence but also provides a strong theoretical guidance for revealing the mechanism of electrocatalytic reactions. Furthermore, theoretical modulation of electrocatalysts can effectively adjust the local hindrance and electronic structure to manipulate the entire workflow of carbon dioxide in the electroreduction process, including local migration, adsorption, activation, hydrogenation, and desorption of the products, thus providing great possibilities and versatility for the realization of carbon dioxide electroreduction. Therefore, reasonable theoretical modulation strategy is the key to improve the catalyst performance. Electrocatalytic reactions generally occur at the interface or surface of the catalyst, and differences in the catalyst structure can affect the strength between the catalyst surface and the adsorbate. At the same



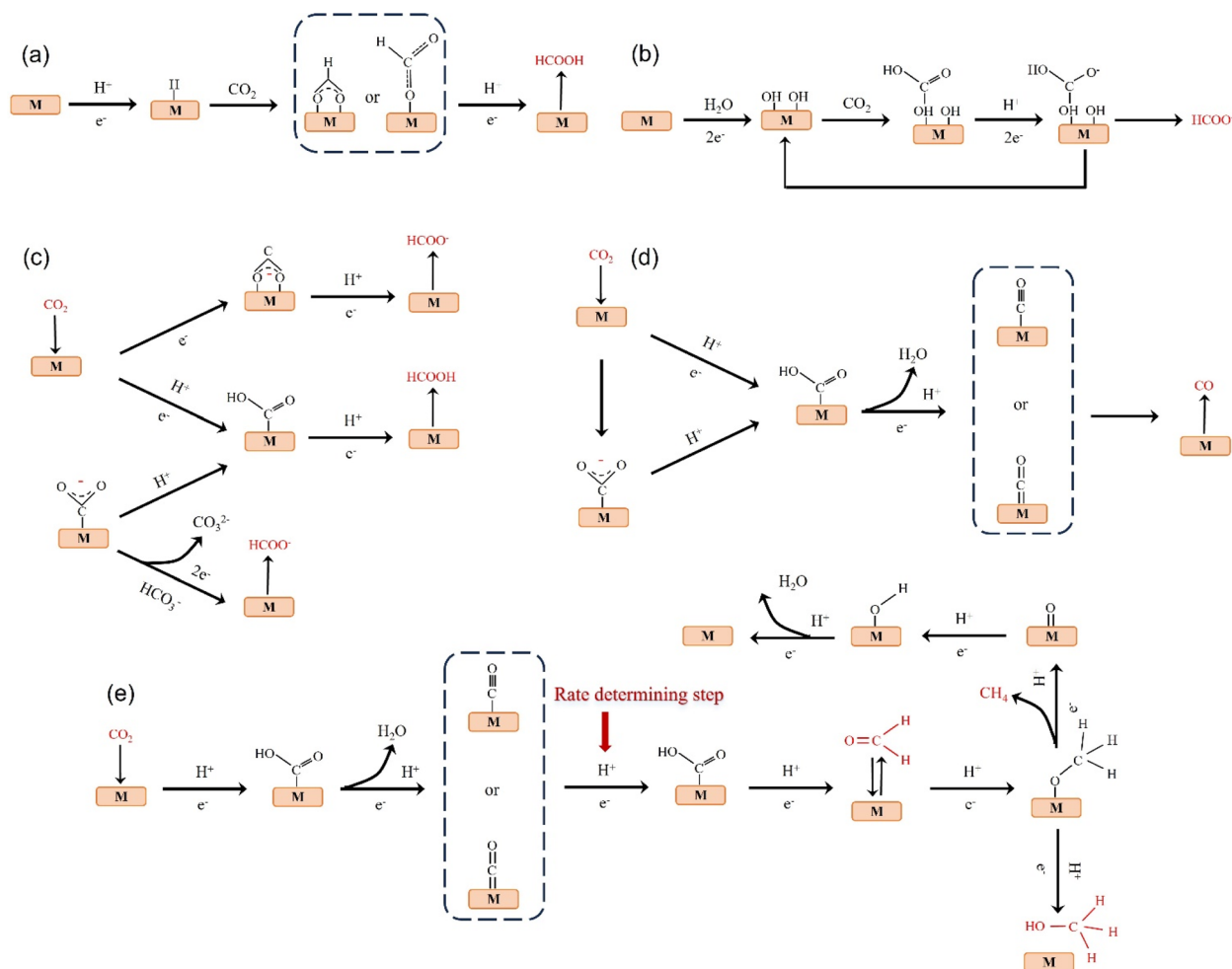


Fig. 3 (a) Monodentate or bidentate intermediate route for HCOOH formation. (b) Surface-bound carbonate intermediate route for the formation of HCOOH/formate. (c) \*CO<sub>2</sub><sup>-</sup> radical intermediate route for the formation of formate. (d) Possible reaction pathway of CO<sub>2</sub> reduction to CO. (e) Possible reaction pathways for the reduction of CO<sub>2</sub> to HCHO, CH<sub>3</sub>OH and CH<sub>4</sub>.

time, the catalyst geometry or electronic structure engineering all produce synergistic effects, influencing the catalytic activity, stability, and selectivity. In addition, changes in the electronic structure of catalysts can directly affect the spin change and change the way catalysts bind to the adsorbent, leading to a decrease in the reaction energy and ultimately an increase in the catalytic activity.<sup>69–72</sup> Therefore, we also combine theoretical modulation to conduct a more profound and comprehensive analysis of the structure activity relationship of ECO<sub>2</sub>RR catalysts.

### 3.1. Metal centers

Metal sites play an important role as the main foundation for adsorbing CO<sub>2</sub> and activating it into different products.<sup>73–76</sup> Since various metal elements have their distinct state of electron clouds in different shell orbitals, they congenitally have significant differences in the CO<sub>2</sub>RR electrocatalytic activity, including current density, stability, and even the types and selectivity of generated products. To date, researchers have researched single-atom catalysts (SACs) covering most of the

transition metal elements like Mo, Fe, Co, Ni, Cu, and Zn, precious metal elements like Au, Ag, Pt, and Ir, and p-block elements like Bi, Sn, and Sb to explore their intrinsic CO<sub>2</sub>RR electrocatalytic properties (Fig. 6).<sup>77</sup> As far as single metal elements are concerned, it commonly possesses the ability to convert CO<sub>2</sub> into CO (g), especially transition metals. Notably, certain metals can reduce CO<sub>2</sub> to produce different products simultaneously.<sup>78</sup> For example, in addition to CO, Co-SACs and Sn-SACs can yield second liquid product CH<sub>3</sub>OH and HCOOH, respectively.<sup>79</sup> However, the determinants of product selectivity remain unclear. The well-designed Zn-N<sub>4</sub>-C structure can generate CH<sub>4</sub> with high economic value.<sup>80</sup> This Zn SAC exhibited remarkable CO<sub>2</sub>RR activity with high faradaic efficiency of 85% toward CH<sub>4</sub> and can maintain this level up to 35 hours. Density functional theory (DFT) calculations revealed that the Zn site follows a unique CO<sub>2</sub>RR mechanism, where the initial activation of CO<sub>2</sub> is more inclined to the O-binding intermediate \*OCHO rather than the C-binding intermediate \*COOH, which is conducive to the hydrogenation of CO<sub>2</sub> to CH<sub>4</sub>. It has been reported that Co, Cu, Mo, In, Sn and Sb can rarely reduce





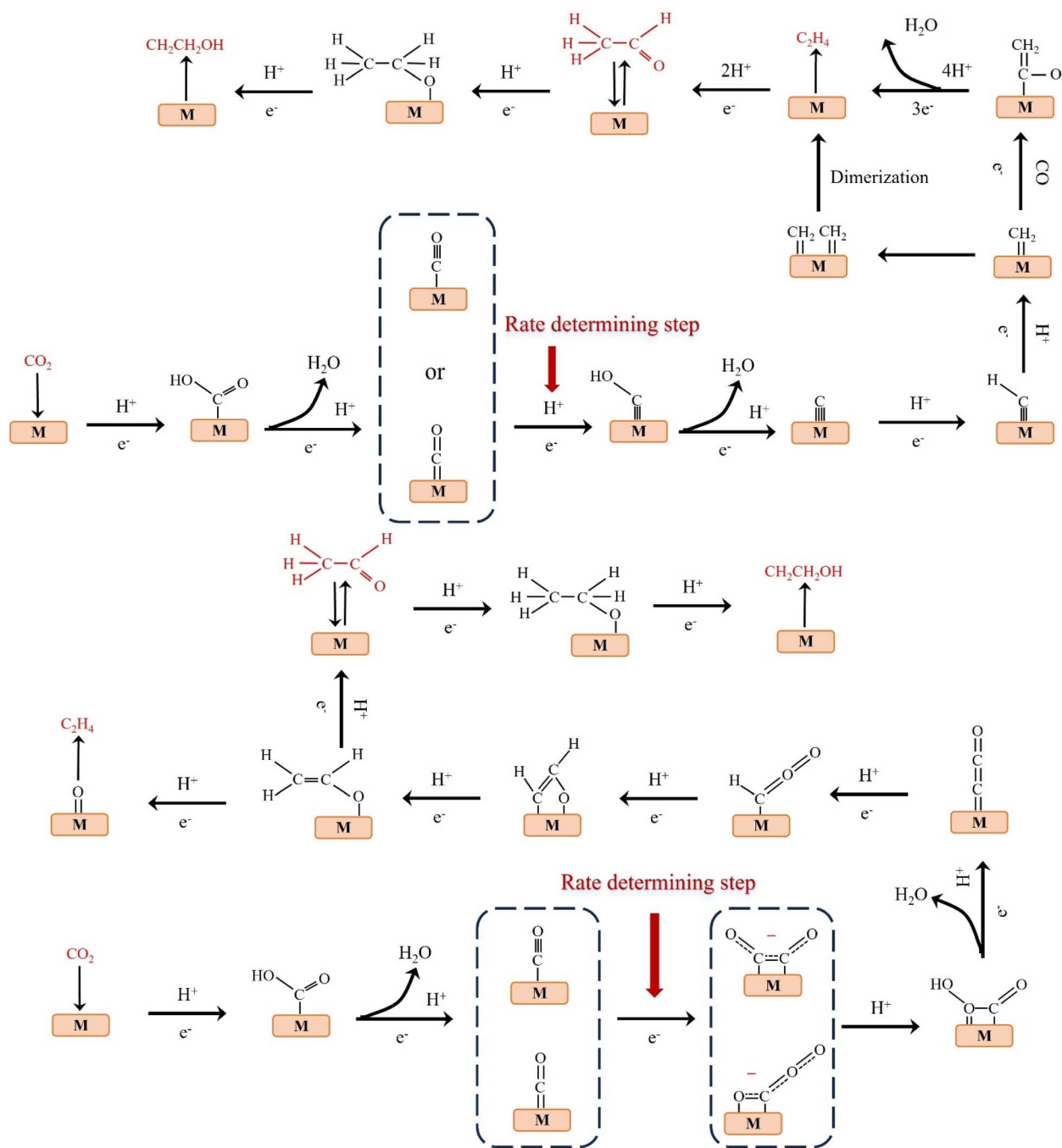


Fig. 4 Possible reaction paths for electrocatalytic CO<sub>2</sub> reduction to produce C<sub>2</sub>H<sub>4</sub>, CH<sub>3</sub>CHO, and C<sub>2</sub>H<sub>5</sub>OH.

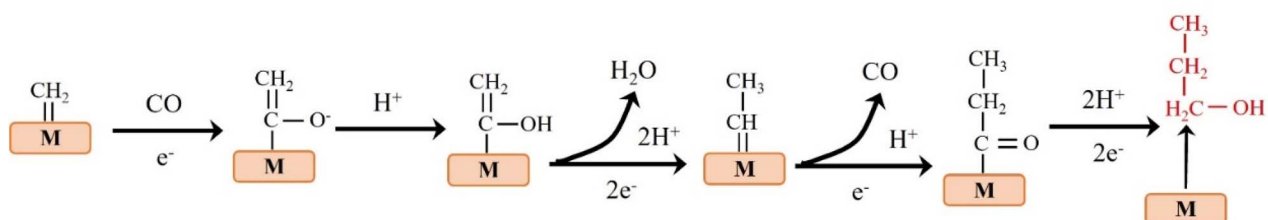
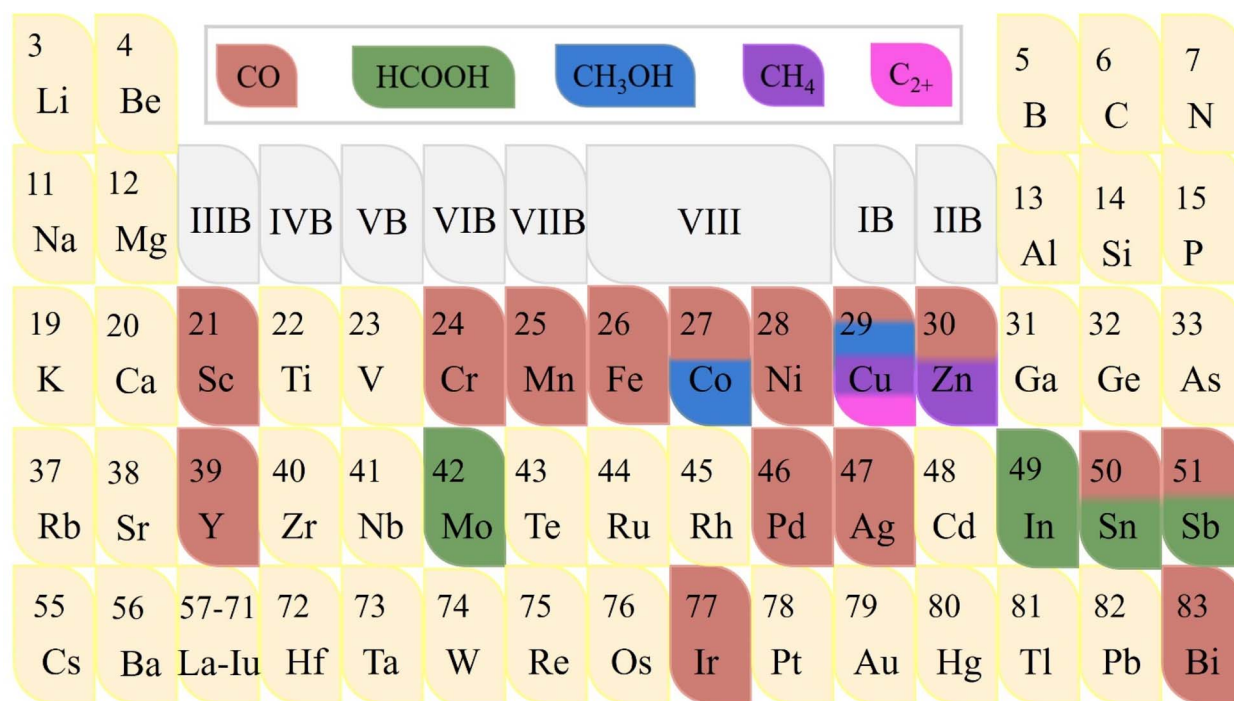


Fig. 5 Possible reaction pathway for electrocatalytic CO<sub>2</sub> reduction to C<sub>3</sub>H<sub>7</sub>OH.



Table 2 Summary of advanced catalysts for ECO<sub>2</sub>R to C<sub>2+</sub> products

Catalyst	FE of C <sub>2+</sub> products (%)	Formation rate of C <sub>2+</sub> $r_{C_{2+}}$ (mmol cm <sup>-2</sup> h <sup>-1</sup> )	Geometric area normalized $j_{C_{2+}}$ (mA cm <sup>-2</sup> )	Electrolyte	Ref.
Cu/Pd-1%	66.2	1.45	463.2	1 M KOH	46
CuO NS	85.6	0.74	237	1 M KOH	47
CuAg-wire-6%	85.1	0.8	264.5	1 M KOH	48
dCu <sub>2</sub> O/Ag2.3%	82.1	2.06	656.8	1 M KOH	49
Li <sub>2-x</sub> CuO <sub>2</sub>	90.6	0.65	200	1 M KOH	50
Cu <sub>3</sub> N <sub>x</sub>	81.7	0.99	307	1 M KOH	51
Cu(OH) <sub>2</sub> -D	86.8	0.65	217	1 M KOH	52
Cu-CuI	71	1.13	381	1 M KOH	53
Nanoporous Cu	62	1.25	411	1 M KOH	54
CuPb-0.7/C	73.6	1.01	294.4	1 M KOH	55
CuO NS	58.6	1.32	410.2	1 M KHCO <sub>3</sub>	56
Ag-Cu/GDY	55.1	—	24.98	1 M KHCO <sub>3</sub>	57
N-doped graphene quantum dots	47.75	—	~90	1 M KOH	58
N-functionalized GO	45.3	—	~1.3	0.1 M KHCO <sub>3</sub>	59
N-functionalized GO	45	—	~50	1 M KOH	60
SnO <sub>2</sub> nanoparticles	10.4	—	150	1 M KHCO <sub>3</sub>	61

Fig. 6 The known product distribution of the reported elements for the ECO<sub>2</sub>RR.

CO<sub>2</sub> to liquid C1 products including HCOOH and CH<sub>3</sub>OH.<sup>81</sup> For example, atomically-dispersed Bi sites follow another reaction mechanism in which the energy barrier advantage of forming \*COOH intermediate is obvious, making the Bi center have higher activity and selectivity for converting CO<sub>2</sub> into HCOOH.<sup>82</sup> Another element used to produce HCOOH is In, which also follows a similar reaction pathway.<sup>83</sup> Interestingly, for the N-C structure, high concentrations of In atoms have been verified to be more inclined to generate HCOOH, while highly dispersed In sites have the ability to accelerate the formation of CO. Unlike In, the selectivity of HCOOH at atomic Sb sites differs

slightly from that of pure metal, while the activity advantage of the former is significant.<sup>84</sup> Theoretical calculations revealed that the intermediate species formed on the Sb-N<sub>4</sub> structure favors forming HCOO\* rather than COOH\*, thus providing a pathway to generate formate with FE<sub>formate</sub> up to 94% at -0.8 V vs. RHE. In particular, due to the dense electron distribution with rich energy of the d and f orbitals in the inner layer, Cu has a strong effect of localization and exchange interaction, thus exhibiting remarkable ability of reducing CO<sub>2</sub> to C<sub>2</sub>, C<sub>3</sub> and even more carbon products.<sup>85</sup> Interestingly, the type and yield of products on the same metal-based material are closely related



to the morphology. For instance, Irabien *et al.* systematically focused on the effect of particle size in the range of 25–80 nm on the conversion efficiency and selectivity of continuous ECO<sub>2</sub>RR on Cu-based nanoparticles.<sup>20</sup> They found that when the particle size was reduced to 25 nm, the ethylene yield and Faraday efficiency with high economic value reached the peak, which were 1148  $\mu\text{mol m}^{-2} \text{s}^{-1}$  and 92.8%, respectively. Simultaneously, the competitive HER was weakened, which strongly verified the inextricable relationship between the material morphology like particle size and the electrocatalytic activity of ECO<sub>2</sub>RR.

Building on single metal sites, introducing additional metal sites to construct heteronuclear active centers can combine the property advantages of various metals.<sup>86</sup> Multinuclear electrocatalysts have a variety of active centers including top and bridging sites, thus providing more diversified adsorption modes for CO<sub>2</sub> and intermediates.<sup>87</sup> Moreover, the coordination between various metal atoms and adjacent ligands is rather flexible, and the d-band center can be regulated through the interaction of electron orbitals, thereby optimizing the adsorption energy of the intermediate species so that it possesses properties particular for SACs to effectively break their inevitable linear scale barrier.<sup>88</sup> The asymmetric multinuclear active centers not only have a significantly enhanced charge density gradient but also locally generate torque, which is conducive to the efficient overlap of atomic orbitals when activating active linear molecules, resulting in the leap of the overall electrocatalytic CO<sub>2</sub>RR performance and showing more potential for practical applications. For example, due to the superior intrinsic activity of Ni and Fe at high and low potentials, respectively, Ren *et al.* designed a Ni/Fe-N-C bimetallic material, which can maintain a high selectivity of CO at a wide potential span from  $-0.4 \text{ V}$  to  $-1 \text{ V}$ , and a high FE<sub>CO</sub> of 98% can be obtained at  $-0.7 \text{ V}$ .<sup>89</sup> Gong *et al.* screened Zn and Co elements,<sup>90</sup> in which the Co site is beneficial for the formation of \*COOH, while the Zn site is beneficial for the desorption of \*COOH. The bimetallic site of Zn/Co-N-C can simultaneously reduce the energy barrier of both the processes to greatly promote the conversion of CO<sub>2</sub> to CO.

### 3.2. Vacancy defects

Vacancies not only have unique electronic properties but also generate a fresh coordination structure to cooperatively optimize the electronic and band structure of the active center to upgrade the chemical properties.<sup>91</sup> Furthermore, vacancy defects provide additional adsorption and active sites for reactive species and moderate the free energy of CO<sub>2</sub> activation and product desorption. Additionally, the defect sites play a crucial role in the electrochemical performance and stability. Due to their high controllable preparation characteristics, vacancy defect engineering is widely used in geometric/electronic structure modulation. In general, vacancies applied in CO<sub>2</sub>RR can be classified into cationic and anionic vacancies.<sup>92</sup> Due to the relatively low energy required to generate anionic vacancies such as O, S, and N, they have been extensively explored combined with theoretical calculations.<sup>93–95</sup> For example, a Cu–

Sn diatom-site electrocatalyst stabilized by double oxygen vacancies on CeO<sub>2–x</sub> was constructed by Chen *et al.* Theoretical calculations emphasized the importance of the synergistic effect of copper and tin in lowering the activation energy and promoting the formation of the intermediate \*OCHO, thus explaining its high formate selectivity (Fig. 7a and b).<sup>96</sup> Besides, a sacrificial protection strategy to stabilize the interfacial crystalline CuO by embedding active amorphous SnO<sub>2</sub> (c-CuO/a-SnO<sub>2</sub>) was reported by Guo *et al.* DFT calculations demonstrated that the loss of oxygen in the heterostructure mainly originates from amorphous SnO<sub>2</sub>, avoiding the reduction of c-CuO. Meanwhile, the production of O<sub>v</sub> in c-SnO<sub>2</sub> leads to off-domain s-orbital electrons around the tin atom, which provides additional electrons in higher orbitals than the unoccupied d-orbitals of Cu<sub>2+</sub> (Fig. 7c and d). Therefore, a-SnO<sub>2</sub> can effectively retain Cu<sub>2+</sub> as a reservoir for oxygen species, thus avoiding oxygen loss from c-CuO, greatly improving the electrocatalytic activity, selectivity, and stability.<sup>97</sup>

The cation vacancies of various metal atoms that act as shallow transport acceptors outperform in catalytic processes, which can effectively tune the band structure, thus giving them unexpected properties without creating new intermediate species.<sup>98</sup> For instance, Lu *et al.* synthesized Ni-N<sub>3</sub>-V single-atom catalysts with vacancy defects at the Ni site. DFT calculations showed that the presence of vacancy defects in Ni-N<sub>3</sub>-V SACs could significantly improve their electrocatalytic activity for CO<sub>2</sub> reduction (Fig. 7e and f).<sup>99</sup> Besides, Xie *et al.* synthesized dynamically reconstructed tri-copper vacancy aggregates confined in copper nanowires. Theoretical calculations showed that triple copper vacancies lead to charge transfer from the surroundings to locations near the vacancies, increasing their local charge density. The charge density difference between the two \*CO on the triple-copper vacancy copper sheet and the pristine copper sheet shows that the different charge distributions of different copper atoms near the defect clusters lead to different charge distributions of the bonded neighboring \*CO, which alleviate the electrostatic repulsion and promote the C–C coupling (Fig. 7g). As a result, the triple copper vacancy binding enriches and redistributes the local negative charge, enhances the adsorption of \*CO intermediates, and lowers the energy barrier for CO–CO coupling, thereby increasing the C<sub>2+</sub> yield.<sup>100</sup> Furthermore, Hu *et al.* designed a Se vacancy-containing bimetallic electrocatalyst denoted as CuInSe<sub>2</sub>. The Se vacancies facilitate electron delocalization, promote electron redistribution, slightly adjust the energy band structure, and optimize the CO<sub>2</sub>RR pathway of the bimetallic selenium compound. As a result, the Se-deficient CuInSe<sub>2</sub> possessed a highly selective CO generation ability in aqueous solution, and the V-CuInSe<sub>2</sub> cathode exhibited satisfactory performance in zinc–CO<sub>2</sub> batteries in water. The CO Faraday efficiency was as high as 91%. In addition, water-based zinc–CO<sub>2</sub> cells based on V-CuInSe<sub>2</sub> cathodes reached a discharge voltage of  $\approx 0.55 \text{ V}$  and had a good lifetime.<sup>62</sup> Although many achievements have been made at the theoretical level, the studies on cation vacancy defects are still limited and need to be further enriched.<sup>101</sup>

**3.2.1. Anionic vacancies.** Among various types of vacancies, oxygen vacancy (V<sub>O</sub>) is the most prevalent due to its low



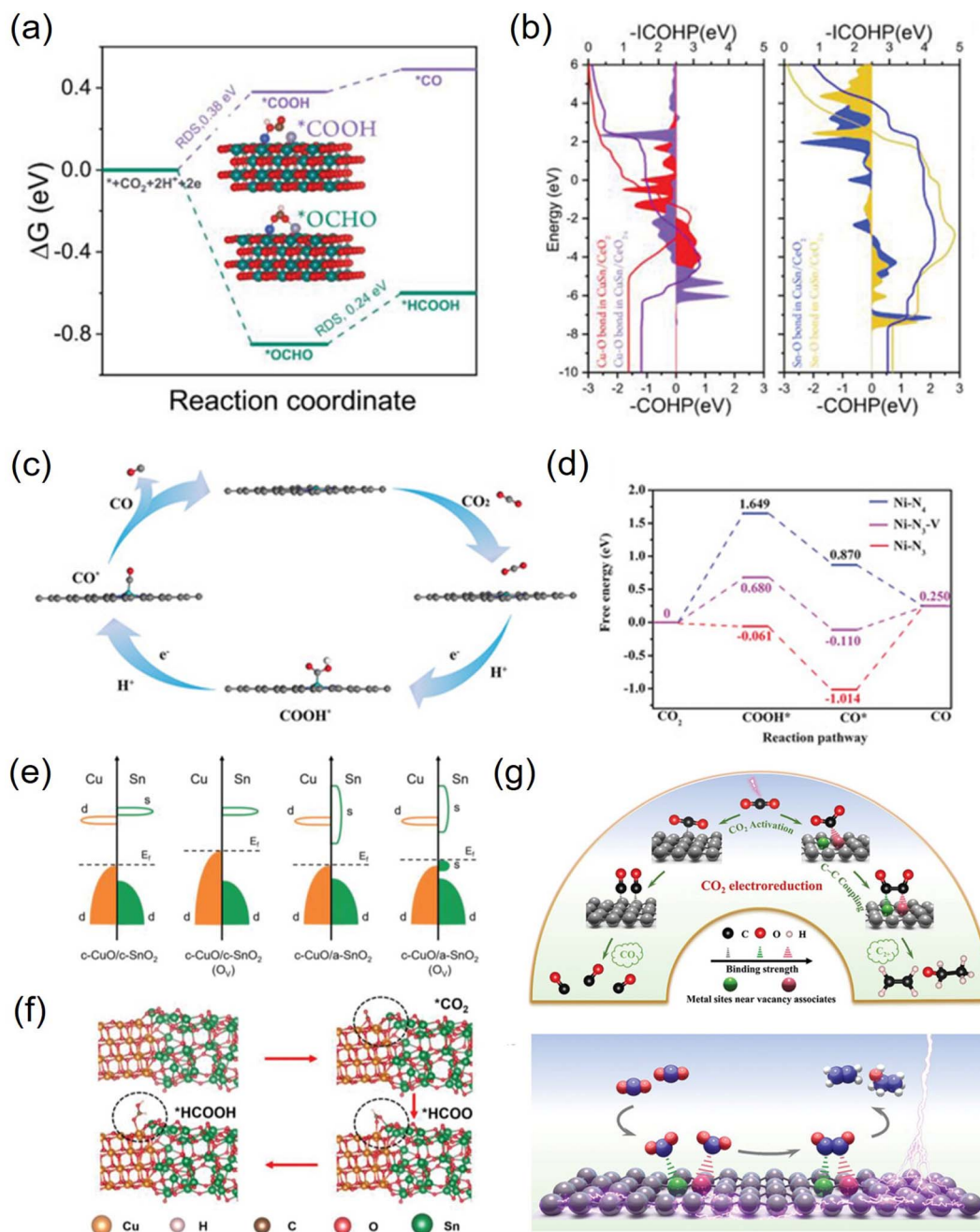


Fig. 7 (a) Free energy profiles of the CO<sub>2</sub>RR on CuSn/CeO<sub>2-x</sub>. (b) The COHP and ICOHP of Cu–O and Sn–O bonds in CuSn/CeO<sub>2</sub> and CuSn/CeO<sub>2-x</sub>. (c) Band structures before and after the formation of O<sub>v</sub> for c-CuO/c-SnO<sub>2</sub> and c-CuO/a-SnO<sub>2</sub>. (d) The typical adsorption process of formate on c-CuO/a-SnO<sub>2</sub>. (e) The proposed reaction paths of Ni-N<sub>3</sub>-V for CO<sub>2</sub> electroreduction to CO. (f) Calculated free-energy diagram for the conversion of CO<sub>2</sub> to CO. (g) Facilitating CO<sub>2</sub> electroreduction to C<sub>2+</sub> production through reconstructed Cu vacancy associates. (a and b) Reproduced with permission.<sup>96</sup> Copyright 2023, Wiley-VCH Verlag. (c and d) Reproduced with permission.<sup>97</sup> Copyright 2023, Wiley-Blackwell. (e and f) Reproduced with permission.<sup>99</sup> Copyright 2019, John Wiley and Sons Ltd. (g) Reproduced with permission.<sup>100</sup> Copyright 2024, Wiley-Blackwell.

formation energy barrier.<sup>102</sup> Since the O atoms of CO<sub>2</sub> can populate the V<sub>O</sub>, efficient trapping of CO<sub>2</sub> molecules can be achieved. Through the chemisorption, the C=O bond is stretched to activate the CO<sub>2</sub> molecule, and the energy barrier of the intermediate species is stabilized to a low value.<sup>103</sup> For example, Gao *et al.* prepared an atomic-layered CO<sub>3</sub>O<sub>4</sub>

material and deliberately created oxygen vacancies on the surface to conduct targeted investigation on its role, revealing that the V<sub>O</sub>-rich material surpasses the contrast sample without V<sub>O</sub> in all the catalytic properties (Fig. 8a–e).<sup>104</sup> The current density of the former is double that of the latter; the FE<sub>HCOOH</sub> is drastically increased from 67.3% to 87.6%, and it





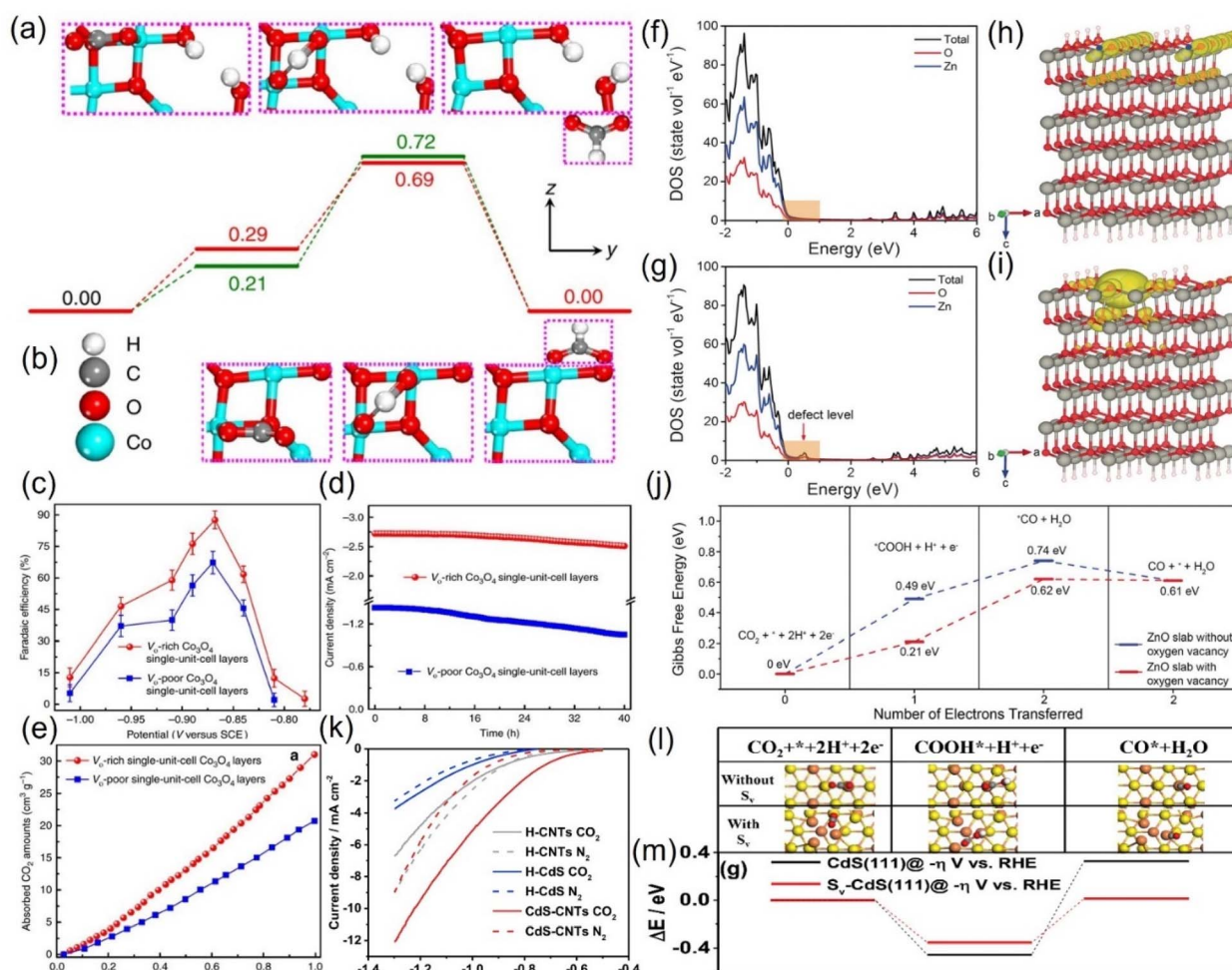


**Fig. 8** Gibbs free energy diagrams of (a)  $V_{O}$ -rich and (b)  $V_{O}$ -poor single-unit-cell  $Co_3O_4$  layers. (c)  $FE_{HCOOH}$  at different applied potentials. (d) Chronoamperometry tests and (e)  $CO_2$  adsorption isotherms of  $VO$ -rich/poor single-unit-cell  $Co_3O_4$  layers. (f and g) DOS. (h and i) Charge density distribution and (j) Gibbs free energy diagrams of (f and h) ZnO slab and (g and i) ZnO slab with oxygen vacancy. (k) LSV curves. (l) Models of different intermediates and (m) DFT calculation results of corresponding intermediates during  $CO_2RR$  on CdS without/with S-vacancy ( $S_v$ ). (a–e) Reproduced with permission.<sup>104</sup> Copyright 2017, Springer Nature. (f–j) Reproduced with permission.<sup>105</sup> Copyright 2018, John Wiley and Sons Ltd. (k–m) Reproduced with permission.<sup>107</sup> Copyright 2020, Royal Society of Chemistry.

can sustain the high  $FE_{HCOOH}$  for up to 40 hours (Fig. 8c and d). Revealed by the  $CO_2$  adsorption isotherm, the remarkable upgradation can be attributed to the abundant  $CO_2$  adsorption sites additionally provided by the  $V_O$  (Fig. 8e). Combined with DFT calculations, they found that  $V_O$  has the effect of stabilizing  $HCOO^-$  radicals, reducing the energy barrier to initiate the rate-limiting step (the electron transfer from  $HCO_3^-$ ) from 0.51 eV to 0.4 eV (Fig. 8a and b). Zeng *et al.* introduced  $V_O$  on the surface of ZnO nanosheets *via*  $H_2$  plasma etching, and the current density ( $16.1 \text{ mA cm}^{-2}$ ) and  $FE_{CO}$  (83%) of the obtained  $V_O$ -ZnO nanosheets were 5 and 1.9 times higher than that of untreated ZnO, respectively, which could operate enduringly without deactivation.<sup>105</sup> Combined with the calculation results, they concluded that  $V_O$  increases the number of charges near the valence band of ZnO, improves the capture capacity of  $CO_2$ , and switches the rate-determining step to the desired surface reaction (Fig. 8f–j).

Besides oxygen vacancies, other anion vacancies have been discovered.<sup>106</sup> For example, Li and colleagues synthesized CdS with ample S vacancies ( $V_S$ ) by pyrolyzing the mixtures of cadmium chloride and thiourea with serial ratios.<sup>107</sup> At the optimal  $V_S$  concentration, the current density of  $V_S$ -CdS at 1 V *vs.* RHE can be as high as  $20.5 \text{ mA cm}^{-2}$ , and the  $FE_{CO}$  can reach 95% with an error less than 0.5% (Fig. 8k). In contrast, the activity of the compared traditional CdS is much lower, indicating that the  $V_S$  is the main contributor to the performance improvement. The  $V_S$  was theoretically revealed to be more prone to adsorb the key intermediate species  $*COOH$ , essentially reducing the difficulty of CO generation (Fig. 8l and m).

**3.2.2. Cationic vacancies.** Cation vacancies profoundly modify the electronic structure and surface properties of catalysts by regulating the removal of metal cations, thereby altering the reaction pathway or reducing the reaction energy barrier, making them more prone to  $CO_2RR$ .<sup>108</sup> Particularly, since



oxygen in the environment destroys the anion hole to induce its loss of efficacy, cations that circumvent this adverse situation appear to be preferable.<sup>66</sup> However, the application of cationic vacancies in electrocatalysis has been rarely reported so far. Since their formation barriers are more unfavorable than those of anionic vacancies, their controllable preparation is more complicated and challenging. To overcome these obstacles, researchers have creatively developed novel strategies to accurately construct cationic vacancies. Using strong acid or alkali to targetedly etch metal sites effectively induces the formation of atomic cationic vacancies (Fig. 9a).<sup>101</sup> Due to the strong acid/base solubility of Zn, Mo, Al and Mn atoms, this method is well suited to weed them out. For layered materials, small molecular organics have been developed to effectively assist in the removal of metal atoms, followed by high-temperature annealing or ultrasonic treatment to produce the desired vacancies. For instance, Qu *et al.* successfully fabricated N-doped Ti<sub>3</sub>C<sub>2</sub> MXene nanosheets with abundant Ti vacancies (V<sub>Ti</sub>) through NH<sub>3</sub>-assisted etch-pyrolysis method (Fig. 9b).<sup>109</sup> It

showed extraordinary electrocatalytic CO<sub>2</sub>RR activity even in untreated seawater with FE<sub>CO</sub> and *j*<sub>CO</sub> (the current density corresponding to the CO), achieving a high level of 92% and 16.2 mA cm<sup>-2</sup>, respectively, as well as durability over 40 hours, which is comparable to the top level in precious metal-based catalysts. DFT calculation results revealed that V<sub>Ti</sub> had the expected modification effect on the metal site, greatly reducing the formation energy barrier of critical \*COOH intermediates and optimized the desorption energy barrier of \*CO to lower the desorption threshold of the product CO, thus significantly improving the efficiency of the CO<sub>2</sub>-to-CO pathway (Fig. 9c–f). In addition, plasma etching is being sought as a new technology.<sup>110</sup> Specifically, it can be conceptually summarized as a two-step procedure: (1) chemical reactions occur through the interaction of the feed gas with the plasma to produce new species. (2) These generated reactants interact with the substrate surface to remove specific materials.<sup>111</sup> It has the following multiple advantages: (1) there is low time consumption and it can maintain the dryness and cleanliness during the operation. (2)

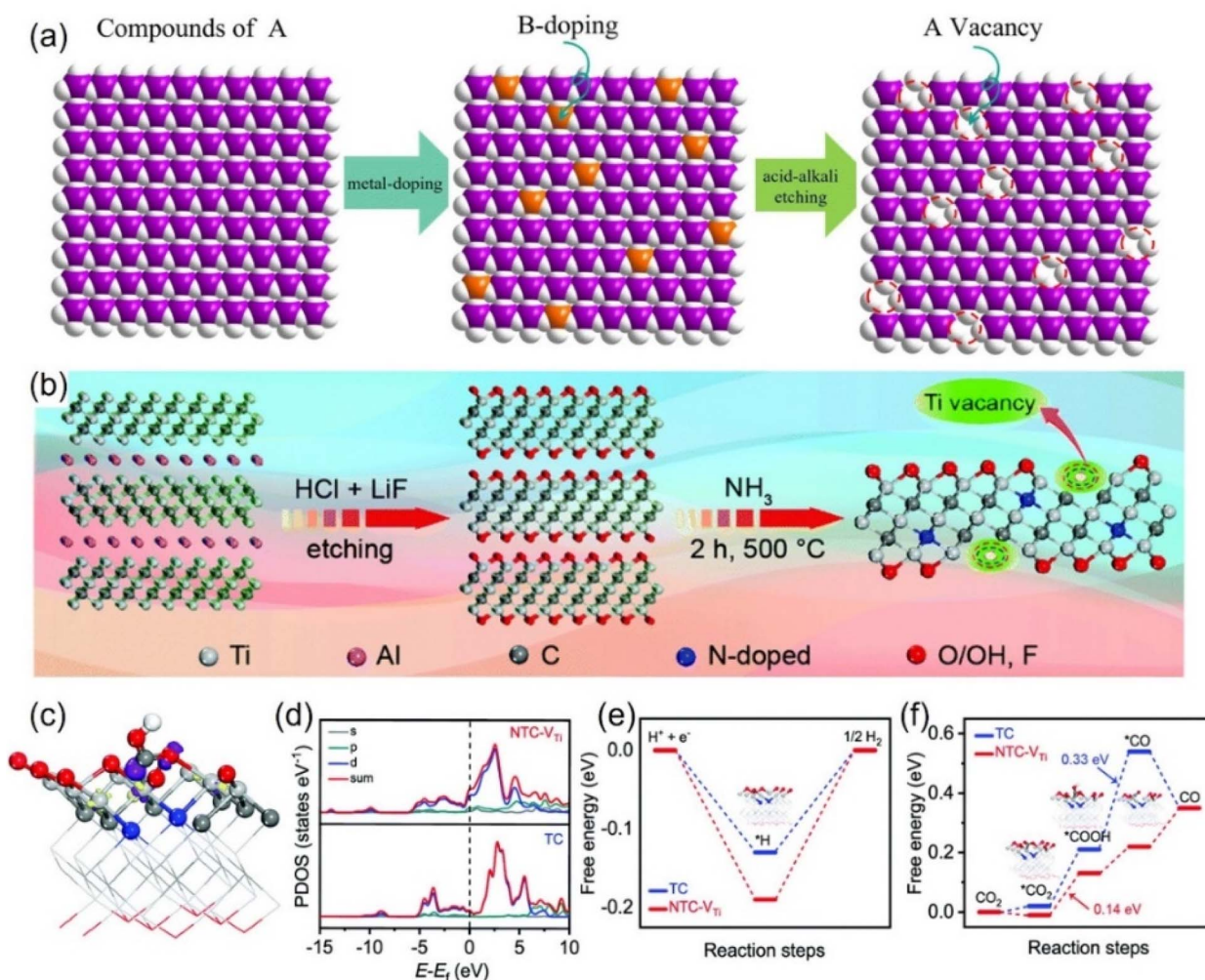


Fig. 9 Schematic diagrams of preparing vacancies through (a) strong acid alkali for targeted-etching and (b) NH<sub>3</sub>-assisted etch-pyrolysis. (c) Electron density model (purple: electron accumulation; yellow: electron depletion). (d) Calculated DOS diagrams of \*COOH adsorbed on NTC-V<sub>Ti</sub>. Free energy diagrams of (e) the HER and (f) CO<sub>2</sub>RR. (a) Reproduced with permission.<sup>101</sup> Copyright 2023, the Royal Society of Chemistry. (b–f) Reproduced with permission.<sup>109</sup> Copyright 2020, the Royal Society of Chemistry.





The multi-functional characteristics make it possible to prepare the target vacancy defects with high precision on almost any material surface. (3) The etching rate can be well controlled. (4) The selectivity of implementing target atoms is high.<sup>112</sup> Furthermore, some niche preparation methods such as chemical reduction, electrochemical stripping and hydrothermal heat treatment routes have also been reported.<sup>113–115</sup>

### 3.3. Strain effect

The Sabatier principle points out that the difficulty of combining the key reaction species and active sites has a direct and profound effect on the reaction rate, and a moderate binding energy barrier will significantly increase the yield and selectivity of the target product.<sup>116</sup> In addition, through theoretical modeling, the location of the d-band center has a significant impact on the adsorption strength of species, *i.e.*, the decrease in the d-band center position will weaken the adsorption between the active site and the intermediate species, and *vice versa*.<sup>117</sup>

Strain engineering is a highly suitable means to regulate the central position of the d-band, and a variety of CO<sub>2</sub>RR active metals have intense strain response. Furthermore, the strain

effect has the unique advantage of breaking through the linear scaling barrier, which will break the original equilibrium space queue between catalyst atoms and cause it to deviate. This will directly fluctuate the binding energy barrier of the key intermediate, which is conducive to the adsorption and activation of CO<sub>2</sub> and the desorption of products and greatly reduces the overall reaction difficulty.<sup>118</sup> These advantages make strain engineering an urgent optimization strategy to be developed. For example, changing the thickness of the Cu sheet on the upper layer of Pt resulted in significant differences in the cell parameters of Cu (3.61 Å) and Pt (3.92 Å), which directly led to the geometric tensile strain of the surface lattice, thus obtaining a more reactive surface with dramatically enhanced the adsorption intensity of the \*CO species, even profoundly altering the optimal reactive pathway.<sup>119</sup> Similarly, Wang *et al.* prepared Ag@Cu NPs with Ag as the core coated with Cu shells with a series of thicknesses by controlling the heating time in the synthesis method of polyol reduction. Ag@Cu-20 with a moderate thickness of Cu layer obtained by heating for 20 min shows the highest selectivity to ethylene, which is much better than that of the corresponding SACs (Fig. 10a).<sup>120</sup> This can be attributed to the surface lattice tensile strain effect, which optimizes the surface activity of the

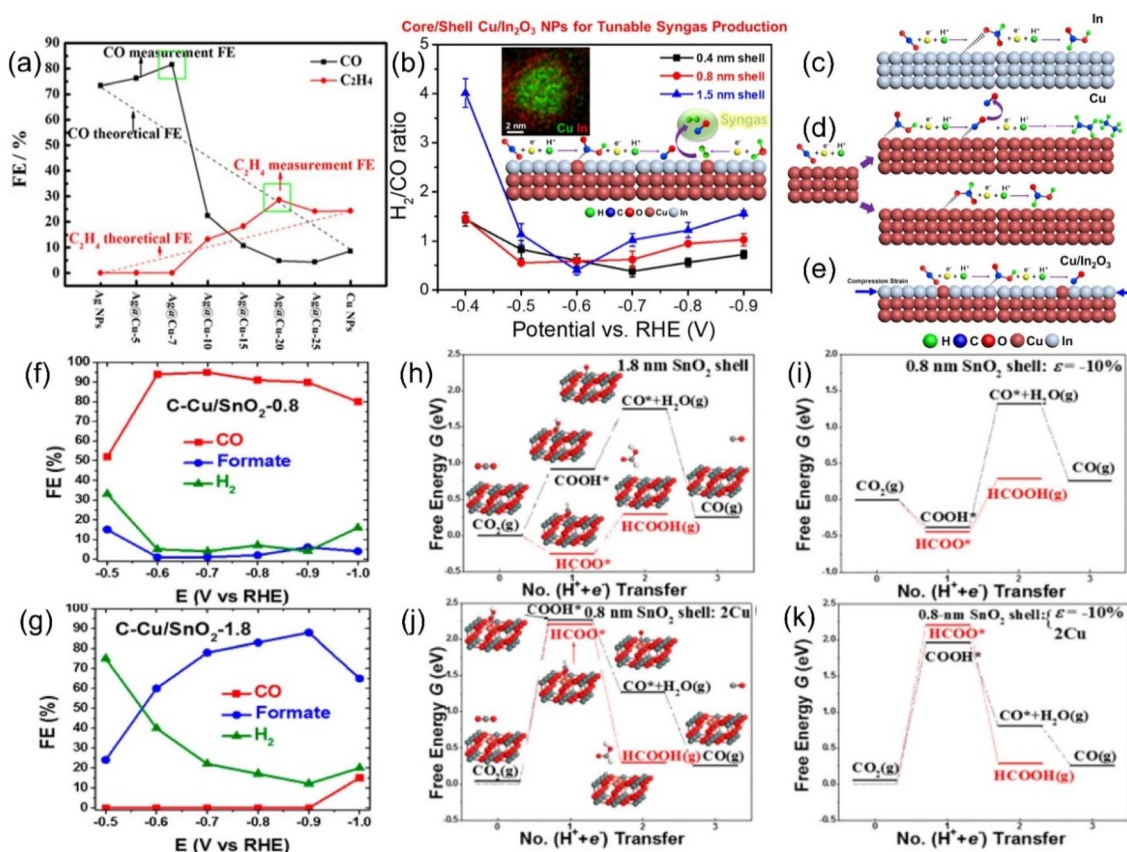


Fig. 10 Theoretical linear “dilution effects” and test values of FEs of CO (black) and C<sub>2</sub>H<sub>4</sub> (red). (b) H<sub>2</sub>/CO ratios generated by C–Cu/In<sub>2</sub>O<sub>3</sub> catalysts. Schematic diagrams of the possible ECO<sub>2</sub>RR pathways on (c) In foil, (d) Cu NPs and (e) Cu/In<sub>2</sub>O<sub>3</sub> NPs. FEs of various products for the ECO<sub>2</sub>RR of (f) C–Cu/SnO<sub>2</sub>-0.8 and (g) C–Cu/SnO<sub>2</sub>-1.8. Free energy diagrams of two ECO<sub>2</sub>RR pathways on SnO<sub>2</sub> shells of different thickness with 10% uniaxial compression of (h) 1.8 nm and (i) 0.8 nm; and 0.8 nm SnO<sub>2</sub> shells with (j) both surface Cu atoms and (k) 10% uniaxial compression. (a) Reproduced with permission.<sup>120</sup> Copyright 2017, American Chemical Society. (b–e) Reproduced with permission.<sup>121</sup> Copyright 2018, American Chemical Society. (f–k) Reproduced with permission.<sup>122</sup> Copyright 2017, American Chemical Society.



material to hydrocarbons and the adsorption strength of  $^*CO$ . Unfortunately, as the shell thickens, the tensile strain decreases due to its short-range properties, resulting in a decrease in the Faraday efficiency of  $C_2H_4$  after the peak. In another similar core-shell system of Cu coated with  $In_2O_3$ , both the current density and the Faraday efficiency of the by-product  $H_2$  and the target product  $CO$  can be adjusted by tuning the shell thickness (Fig. 10b).<sup>121</sup> It has been reported that the synergistic effect of compressive strain and Cu doping effect promotes the formation of  $^*COOH$  rather than the  $HCOO^*$  intermediate, thus boosting the precipitation of  $CO$  (Fig. 10c-e). Interestingly, Sun *et al.* reported another Cu-based material wrapped by  $SnO_2$ . When the thickness of  $SnO_2$  is 1.8 nm, the material is more inclined to exhibit the activity of Sn with the higher selectivity of  $HCOOH$ , while when it becomes thinner than 0.8 nm, the  $FE_{CO}$  overwhelmingly reaches 93% (Fig. 10f and g).<sup>122</sup> Combined with various characterization and theoretical calculation results, this unique phenomenon is attributed to the lattice mismatch between  $SnO_2$  and Cu, resulting in a large compressive strain of up to 10% in the shell (Fig. 10h-k).

Furthermore, the electrocatalytic reduction of carbon dioxide to multi-carbon products involves complex multiple proton and C-C coupled electron transfers, which are not only determined by the intrinsic reactivity of the catalyst but are also related to the spin state of the electrons. Yao *et al.* observed the electrocatalytic activity of spin-enhanced carbon dioxide reduction over oxide-derived copper (OD-Cu) catalysts (Fig. 11a). Due to the magnetic nature of the Cu site, the Faraday efficiency of  $CO_2RR$  could be increased by 15% using the OD-Cu catalyst. In addition, the stray field of copper polarizes the electron spins transferred from the neighboring copper, facilitating the conversion of the C-C coupling reaction on the Cu-Cu site to  $C_2$  products (*e.g.*, ethane), thereby reducing the generation overpotential of the  $C_2$  products.<sup>123</sup> Metal-nonmetal hybridized diatomic catalysts were designed and synthesized by An *et al.* Combining spin-polarized DFT and hydrogen electrode computational models, the hybridized M-B diatomic centers are superior to single and double M centers in driving  $CO_2RR$ , especially C-C coupling. The electronic spin state of the metal may be particularly important in regulating the selectivity of  $CO_2RR$  and the C-C coupling

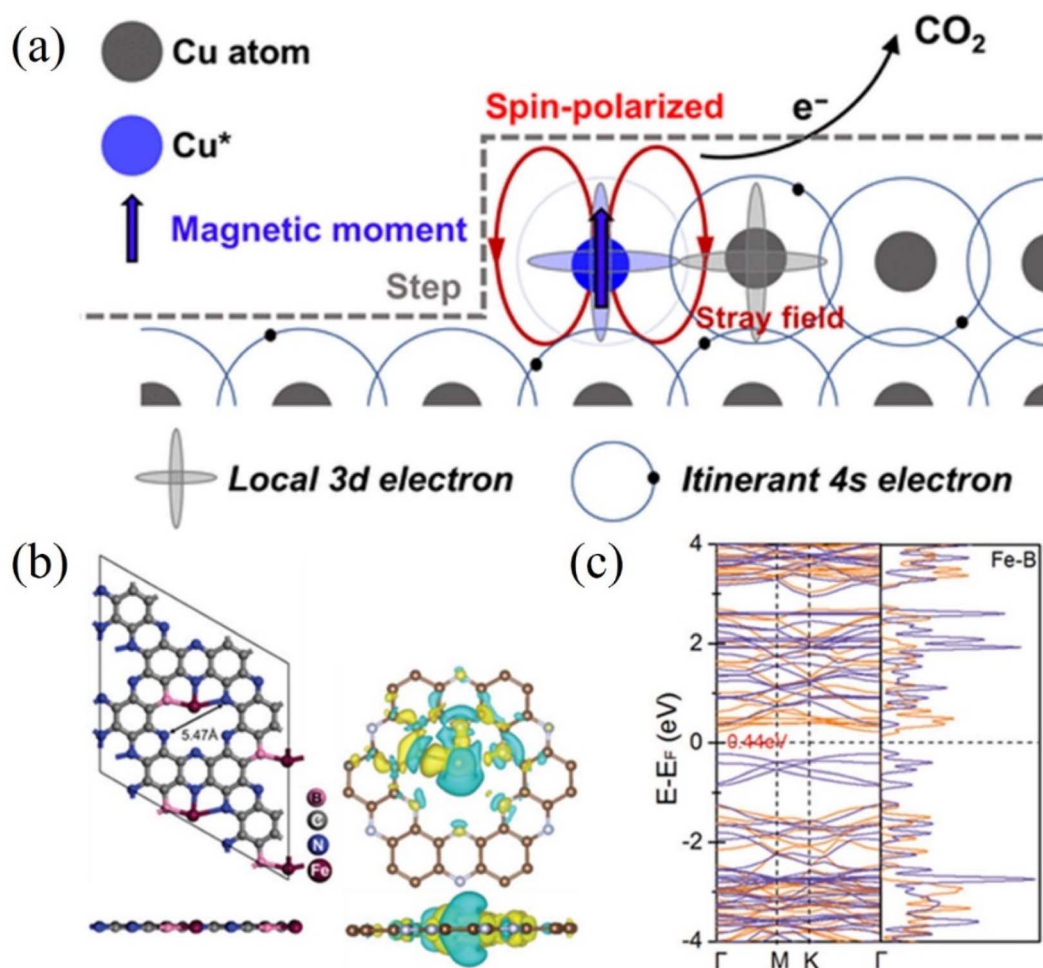


Fig. 11 (a) Spin-related catalysis for the  $CO_2RR$  in the OD-Cu catalyst. (b) Optimized structure of  $Fe@B-C_2N$  along with the iso-surface of charge density difference. Yellow: charge accumulation; cyan: charge depletion. (c) DFT-calculated electronic band structure and density of states of  $Fe@B-C_2N$  near the Fermi level using the HSE06 functional. (a) Reproduced with permission.<sup>123</sup> Copyright 2023, Chinese Chemical Society. (b and c) Reproduced with permission.<sup>124</sup> Copyright 2021, Wiley-VCH Verlag.





potential. Under ambient conditions, the high spin moments of the M-B diatomic site M favor the promotion of C-C coupling and protonation in CO<sub>2</sub>RR (Fig. 11b and c). The enhanced spin state of the metal led the authors to predict Fe@B-C<sub>2</sub>N as an active catalyst for the conversion of CO<sub>2</sub>RR to C<sub>2</sub>.<sup>124</sup> Chen *et al.* investigated the effect of oxidation states of Fe ions with different spins in FeN<sub>4</sub>C on the electrochemical mechanism of CO<sub>2</sub> conversion to CO/HCOOH. Potential energy analysis revealed that among the two oxidation states with different spins, the rate-limiting step of CO/HCOOH generation catalyzed by intermediate-spin Fe<sup>II</sup>N<sub>4</sub>C<sub>M</sub> has lower potential barriers (0.72/0.52 eV). In addition, the overpotentials (−0.03/0.29 V) on Fe<sup>II</sup>N<sub>4</sub>C<sub>M</sub> for <sup>\*</sup>CO/<sup>\*</sup>HCOOH generation are also significantly lower than that of other cases. Both confirm that Fe<sup>2+</sup> ions with intermediate spins in FeN<sub>4</sub>C are favorable for the conversion of CO<sub>2</sub> to CO/HCOOH.<sup>125</sup>

### 3.4. Coordination environment

The coordination environment composed of metal active sites as the core and adjacent bonding atoms is considered to be the universal knob for regulating the electrocatalytic performance. The spatial site of these atoms will create a variety of three-dimensional structures that have a fatal impact on the interaction strength between the CO<sub>2</sub> molecules/intermediate species and the reaction site. Moreover, the lattice distortion and charge transfer between the atoms in the coordination environment directly affect the geometry and electronic structure of the active site, thus endowing the material with a wide range of catalytic properties and even fundamentally changes the reaction pathway of electrocatalytic CO<sub>2</sub>RR.<sup>126</sup> Therefore, the

in-depth analysis of the coordination environment to clarify the key factors affecting its configuration and the essential way in which it impacts the catalytic process is of great significance, which is helpful to promote the precise regulation of the coordination environment and open up the way for the rational design of a new generation of high-performance industrial grade catalysts.

**3.4.1. Basic N-doping M-N-C structure.** Among the various coordination atoms, N has the highest probability of appearance, with abundant storage and high selectivity of doping sources. In addition, the doped N atoms fill the overall electron cloud density of the coordination environment to reinforce the active metal site and give them more flexible redox capacity.<sup>127</sup> Therefore, a series of isolated M-N-C coordination structures have been fully studied as the most classical configurations. As far as the current technology is concerned, the controllability of the coordination number of the active metal sites can be achieved by regulating the pyrolysis temperature, but the overall repeatability of the bonding motifs is still not achieved. Fig. 12 shows all possible M-N-C combinations that have been verified, including different coordination numbers and N-atom formations. However, so far, there is no consistent conclusion between theory and experiment as to which configuration has the best electrocatalytic activity for CO<sub>2</sub>RR.<sup>66</sup>

At the theoretical level, DFT calculations predicted that the Ni-N-C<sub>3</sub> configuration has the best electroactivity of CO<sub>2</sub>RR.<sup>128</sup> Compared with the Ni-C<sub>4</sub> structure, the introduction of an N atom increases the overall charge capacity, enhancing the reduction ability of CO<sub>2</sub> molecules, optimizing the binding energy of CO\*, and thus reducing the desorption difficulty of

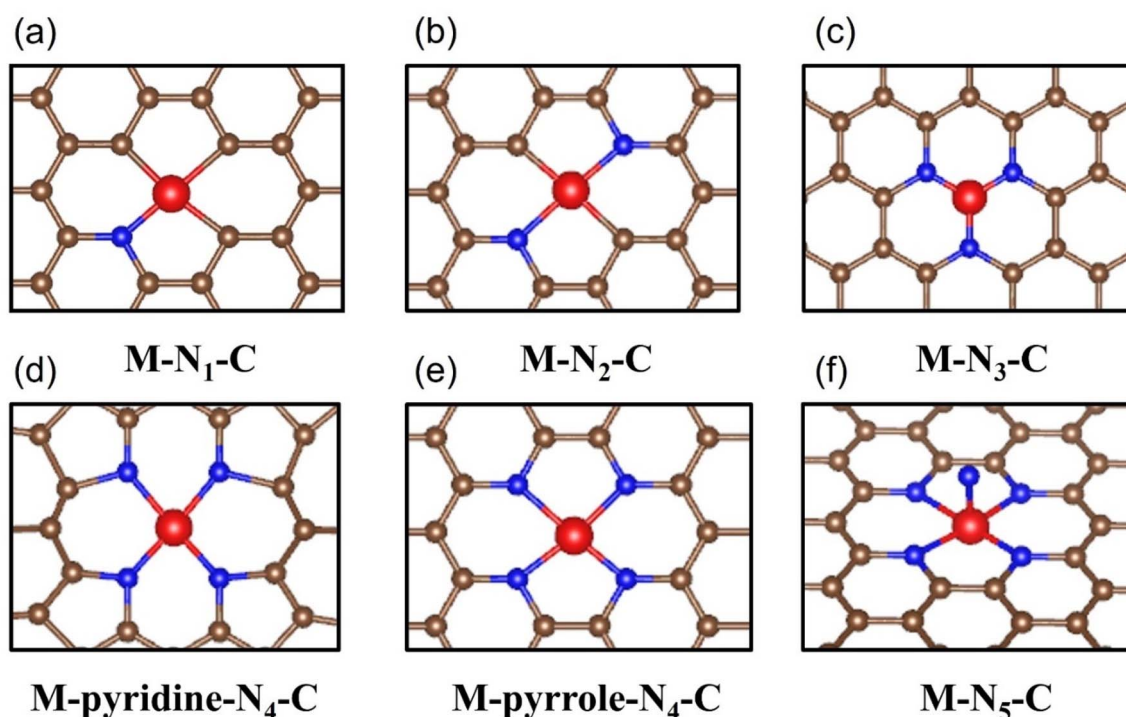


Fig. 12 Schematic diagrams of all reported M-N-C configuration types including (a) M-N<sub>1</sub>-C, (b) M-N<sub>2</sub>-C, (c) M-N<sub>3</sub>-C, (d) M-pyridine-N<sub>4</sub>-C, (e) M-pyrrole-N<sub>4</sub>-C and (f) M-N<sub>5</sub>-C.



CO. However, Ni-N<sub>4</sub> has a lower work function in the charge-neutral state, which makes it more difficult to replenish its charge to the same Fermi level. In another calculation model, when selecting different rate-determining steps, the structure with the highest catalytic potential for CO<sub>2</sub>RR was determined to be highly coordinated M-N<sub>4</sub>/N<sub>5</sub>.<sup>129</sup> For example, Luo *et al.* selected grand canonical potential kinetics (GCP-K) as the basic algorithm for theoretical prediction to obtain the result of Ni-N<sub>4</sub> exhibiting the best catalytic performance (Fig. 13a).<sup>130</sup> This conclusion has also been verified from the experimental results that under -1.05 V vs. RHE, such a structure can convert CO<sub>2</sub> to CO with nearly 100% selectivity, and  $j_{\text{CO}}$  is as high as 40 mA cm<sup>-2</sup>, which is superior to low coordination configuration with 2N or 3N. The coordination environment of other metals also follows a similar rule. For instance, Li *et al.* reported that the

Fe<sub>CO</sub> and  $j_{\text{CO}}$  in the Co-N<sub>4</sub> configuration in the wider potential range from -0.5 V to -1.0 V vs. RHE always occupy one place in the group of Co-N<sub>4-x</sub> configurations.<sup>131</sup> As shown in Fig. 13d and e, the same M-N<sub>4</sub> configuration while using diverse N-containing ligands will result in differences in the final coordination motifs with vastly different intrinsic activity. For example, when pyrrolic N is used as the ligand, Fe<sup>3+</sup> is bonded ultra-firmly to achieve the rapid adsorption of CO<sub>2</sub>, while in the case of pyridinic N, the catalytic performance is exactly the opposite and the electron cloud of Fe<sup>3+</sup> is regulated more actively, causing it to be more inclined to absorb electrons and be reduced to Fe<sup>2+</sup> (Fig. 13b-f).<sup>132</sup>

The experimental evaluation reveals that M-N<sub>x</sub> has better electrocatalytic CO<sub>2</sub>RR ability than M-N<sub>4</sub> because the former has a higher Gibbs free energy for side reaction, leading to HER with

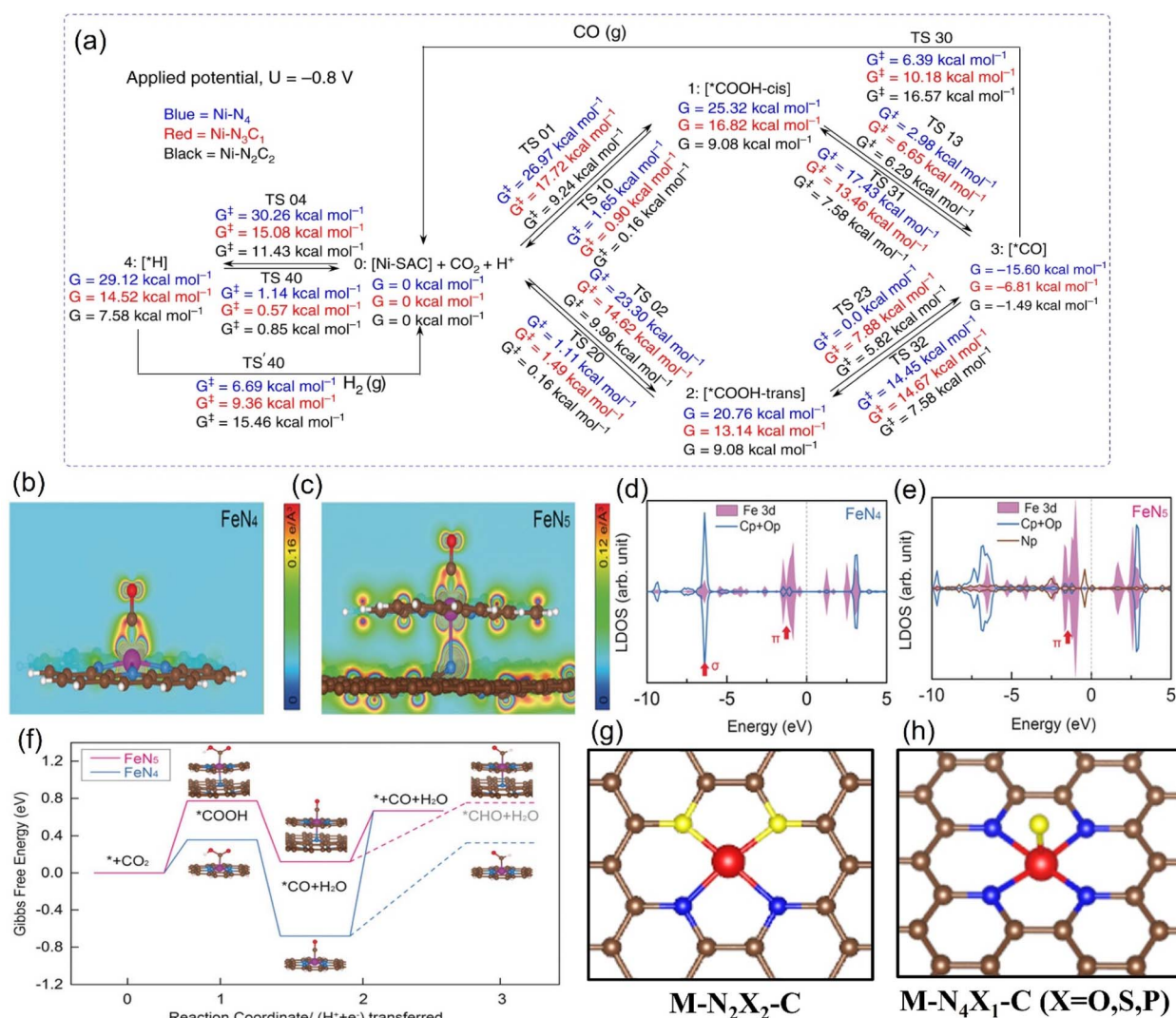


Fig. 13 (a) Schematic representation of calculated free energies with GCP-K as the basic algorithm. Partial charge density of (b) the O-C-Fe-N plane adsorbing CO within the energy range from -1.56 to -0.82 eV for FeN<sub>4</sub> model and (c) the O-C-Fe-N-pyrrolic N plane adsorbing CO within the energy range from -3.31 to -0.99 eV for the FeN<sub>5</sub> model. (d and e) Calculated DOS diagrams of the (d) FeN<sub>4</sub> model and (e) FeN<sub>5</sub> model adsorbing CO and (f) free energy diagram for the ECO<sub>2</sub>RR to CO. Schematic diagrams of (g) N-heteroatom co-doped M-N<sub>2</sub>X<sub>2</sub>-C configuration and (h) axially-coordinated M-N<sub>4</sub>X<sub>1</sub>-C configuration. (a) Reproduced with permission.<sup>130</sup> Copyright 2020, Springer Nature. (b-f) Reproduced with permission.<sup>132</sup> Copyright 2019, John Wiley and Sons Ltd.



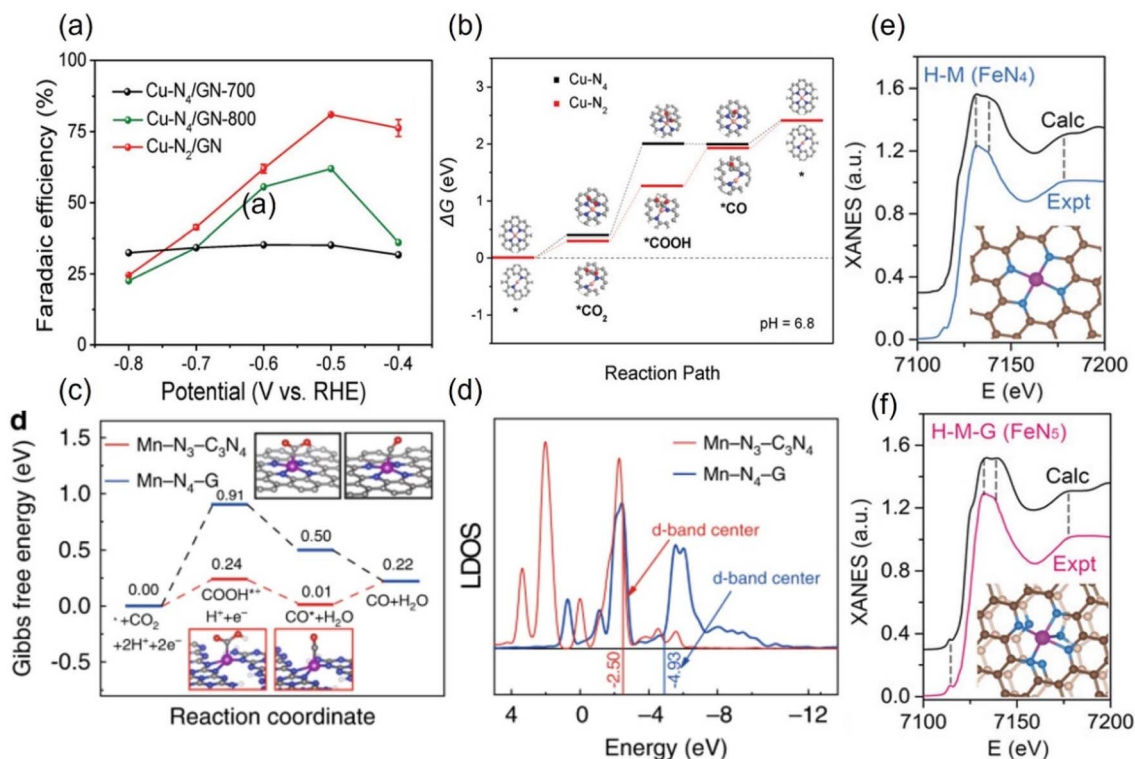


Fig. 14 (a)  $FE_{CO}$  diagrams and (b) calculated free energy diagrams for the  $ECO_2RR$  of Cu in Cu-N<sub>4</sub> and Cu-N<sub>2</sub>. (c) Calculated free energy diagrams for the  $ECO_2RR$  and (d) calculated DOS diagrams of Mn in Mn-N<sub>3</sub>-C<sub>3</sub>N<sub>4</sub> and Mn-N<sub>4</sub>-G. Comparison of the experimental with the calculated XANES data of (e) FeN<sub>4</sub> and (f) FeN<sub>5</sub>. (a, and b) Reproduced with permission.<sup>135</sup> Copyright 2019, Wiley-VCH Verlag. (c and d) Reproduced with permission.<sup>137</sup> Copyright 2020, Springer Nature. (e and f) Reproduced with permission.<sup>132</sup> Copyright 2019, John Wiley and Sons Ltd.

less probability, while the formation energy barrier of the active \*COOH species is lower.<sup>133</sup> For example, in a series of N-coordinated configurations of Co metal atoms (Co-N<sub>2</sub>-C, Co-N<sub>3</sub>-C, and Co-N<sub>4</sub>-C), Co-N<sub>2</sub>-C has prominent CO<sub>2</sub>RR activity, with a TOF value of up to 18 200 h<sup>-1</sup>.<sup>134</sup> Similarly, the catalytic performance of Cu-N<sub>2</sub> with  $FE_{CO}$  is up to 81%, better than that of Cu-N<sub>4</sub> configuration when applying a small potential of -0.5 V vs. RHE (Fig. 14a).<sup>135</sup> As explained by the difference in the geometric structure of different coordination modes, the chemical bond coordinated by double N atoms is not as long as that of four N atoms, which makes the electron transfer of metal sites and adsorbed intermediates faster, thus accelerating the activation of key \*CO<sub>2</sub> species (Fig. 14b). In addition, some metals show the advantage of catalyzing CO<sub>2</sub>RR in the three-N coordination environment. For example, the rate-limiting step of Ni-N<sub>3</sub>, the process of activating CO<sub>2</sub> to a \*COOH intermediate, has an easier barrier to cross than that of Ni-N<sub>4</sub>.<sup>136</sup> Combined with various *in situ* characterizations, the electrons in the metal center of the Mn-N<sub>3</sub>-C<sub>3</sub>N<sub>4</sub> coordination structure constructed on three-dimensional carbon nanotubes will rearrange after adsorbing CO<sub>2</sub> molecules, resulting in an increase in the oxidation state.<sup>137</sup> After a round of CO<sub>2</sub>RR cycle, the oxidation state will be reduced back to the initial state, which verifies the efficient CO<sub>2</sub>RR on this configuration. The  $FE_{CO}$  and the corresponding current density can reach 98.8% and 14 mA cm<sup>-2</sup> at a low bias of 0.44 V vs. RHE, respectively. The local

density of states analysis demonstrates that the d-band center of Mn-N<sub>3</sub>-C<sub>3</sub>N<sub>4</sub> is closer to the Fermi level than that of the Mn-N<sub>4</sub> configuration supported on two-dimensional graphene, which greatly reduces the difficulty of CO<sub>2</sub> capture and activation (Fig. 14c and d). Interestingly, on the basis of the planar configuration of M-N<sub>4</sub>, the structure of M-N<sub>5</sub> formed by bonding an additional N atom in the axial direction has been developed (Fig. 14f).<sup>132</sup> For example, the oxidation state of the typical Fe-N<sub>5</sub> group obtained by the synchrotron X-ray absorption spectroscopy (XAS) is significantly higher than that of the common Fe-N<sub>4</sub>, thus effectively promoting the process of catalyzing CO<sub>2</sub>RR.<sup>132</sup> This conclusion has been reasonably explained *via* theoretical calculations, *i.e.*, the d-electron transfer between the Fe site and the additional N atom is more active, which weakens the bonding energy of the former and the \*CO species and makes it easier for CO to detach from the output (Fig. 14e and f). It is concluded that even small differences in the coordination environment can have an unpredictable and crucial effect on the electrocatalytic activity of CO<sub>2</sub>RR.

**3.4.2. Heteroatom-doping M-NX-C structure.** The types of M-NX-C structures formed by introducing other coordination elements on the basis of M-N-C are more variable, and the space to be developed is broader. At present, there is still a lack of targeted research in this field, but the coordination of heterogeneous atoms has been recognized as a feasible means to break the symmetry of the overall electron distribution and





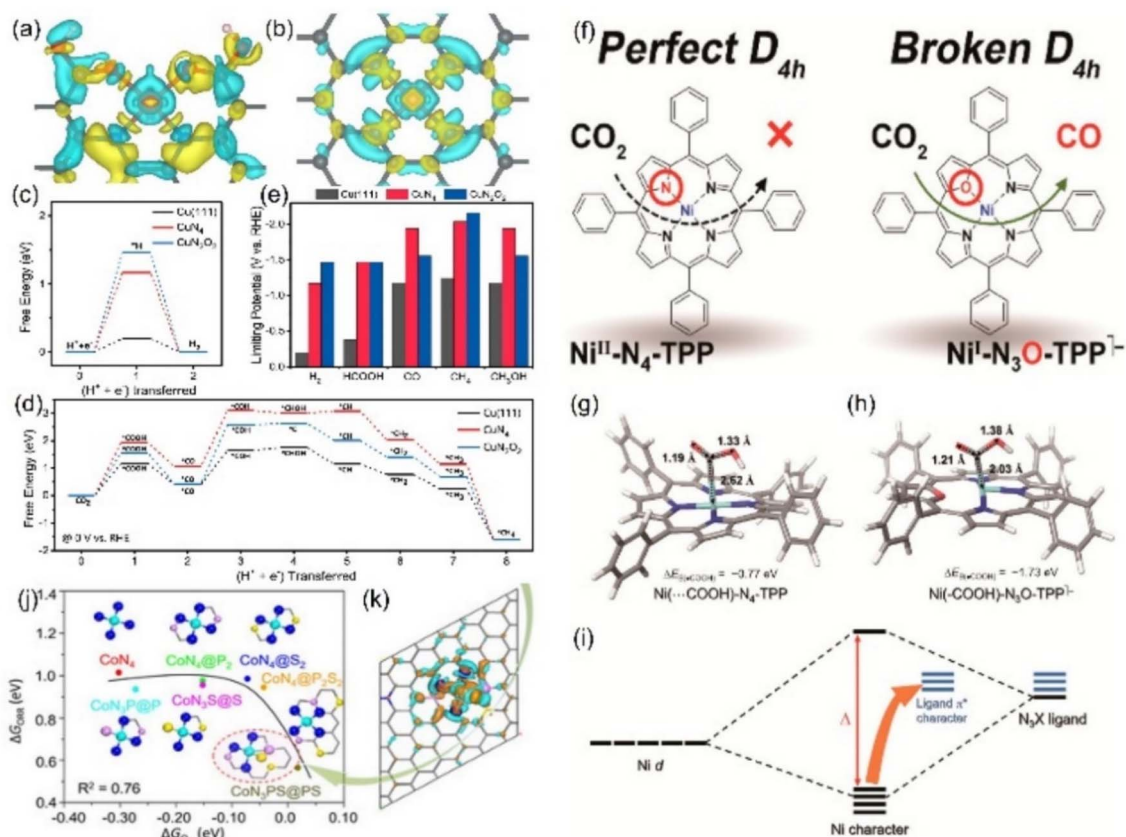


Fig. 15 Charge densities of (a)  $\text{CuN}_2\text{O}_2$  and (b)  $\text{CuN}_4$  (yellow: increase in the number of electrons; blue: the depletion zone). Free energy diagram of (c) the HER and (d)  $\text{ECO}_2\text{RR}$  to  $\text{CH}_4$  and (e) summary of the limiting potentials of various products. (f) Schematic diagrams of  $\text{Ni-N}_4\text{-TPP}$  and  $\text{Ni-N}_3\text{O-TPP}$ . DFT-optimized structures of adsorbing  $^*\text{COOH}$  in (g)  $\text{Ni-N}_4\text{-TPP}$  and (h)  $\text{Ni-N}_3\text{O-TPP}$ . (i) Schematic diagram of the molecular orbital. (j) The linear relationship for the overpotential as a function of the  $\text{O}_2^*$  adsorption energy and (k) charge density difference of the Co site of  $\text{CoN}_3\text{PS}$ . (a–e) Reproduced with permission.<sup>139</sup> Copyright 2021, Springer Nature. (f–i) Reproduced with permission.<sup>140</sup> Copyright 2021, American Chemical Society. (j and k) Reproduced with permission.<sup>142</sup> Copyright 2020, John Wiley and Sons Ltd.

unlock unfamiliar  $\text{CO}_2\text{RR}$  pathways and even the product types.<sup>138</sup> For instance, Cai *et al.* established a coordination environment for  $\text{Cu-N}_2\text{O}_2$  using the chelating assistance of organic ligands.<sup>139</sup> Due to the strong covalent interaction between the  $\text{Cu}^{2+}$  center and the adjacent O atoms, the electrons of the whole group can be favorably redistributed, and the binding energy of the 2p orbital of the active Cu site is reduced, which enables its conversion from  $\text{Cu}^{2+}$  to  $\text{Cu}^+$  or  $\text{Cu}^0$  with lower oxidation states. The lower positive charge density makes the binding energy barrier of  $\text{Cu-N}_2\text{O}_2$  to the key  $^*\text{H}$  of the side reaction HER increase compared with the  $\text{Cu-N}_4$  configuration, while decreasing it for all the  $\text{CO}_2\text{RR}$  intermediate species (Fig. 15a–e). In addition, Kim *et al.* ingeniously obtained a well-defined  $\text{Ni-N}_3\text{O}$  configuration by directly destroying the symmetric structure of tetraphenylporphyrin ( $\text{N}_4\text{-TPP}$ ), denoted as  $\text{Ni-N}_3\text{O-TPP}$  (Fig. 15f).<sup>140</sup> Theoretical calculations reveal that the polarization effect of O doping reduces the chemical valence state of the Ni center, thereby obtaining an ideal bonding strength with the key  $^*\text{COOH}$  species compared with  $\text{Ni-N}_4$  configuration synthesized through a similar method ( $\text{Ni-N}_4\text{-TPP}$ ) (Fig. 15g–i). In another report with the similar idea, S atom replaces the two diagonal pyrrole N atoms in the porphyrin

framework, resulting in a steep increase in the electron transport capacity of the Fe site compared to the traditional  $\text{Fe-N}_4$  configuration.<sup>141</sup> In addition, the electronic state density of the active site has been optimized by additional co-doping P and S atoms on the basis of N coordination in making the active Co sites bonded with atoms of three elements ( $\text{CoN}_3\text{PS}$ ), and its ORR electrocatalytic activity can be compared to the cutting-edge level of precious metals (Fig. 15j and k).<sup>142</sup>

Other elements except N can also be axially doped to construct the same coordination configuration as  $\text{M-N}_5$ , as discussed in the previous section (Fig. 11h). For example, Han's team reported the  $\text{Cd-N}_4\text{S}_1$  structure that exhibits completely different  $\text{CO}_2\text{RR}$  catalytic properties in comparison with the  $\text{Cd-N}_5$  configuration.<sup>143</sup> Although both the axial S and N atom play a significant role in activity optimization, the S atom reduces the Gibbs free energy threshold of the rate-limiting step due to its extremely high spin density state with charge delocalization effect (Fig. 16a–c). In addition to the fact that the Cd atom is instinctively inclined to form this configuration due to its large radius, the beneficial effect of the fifth axial heteroatom also acts on other metals. For instance, Xin *et al.* chose organic diphenyl sulfide as the S source to axially incorporate the fifth S





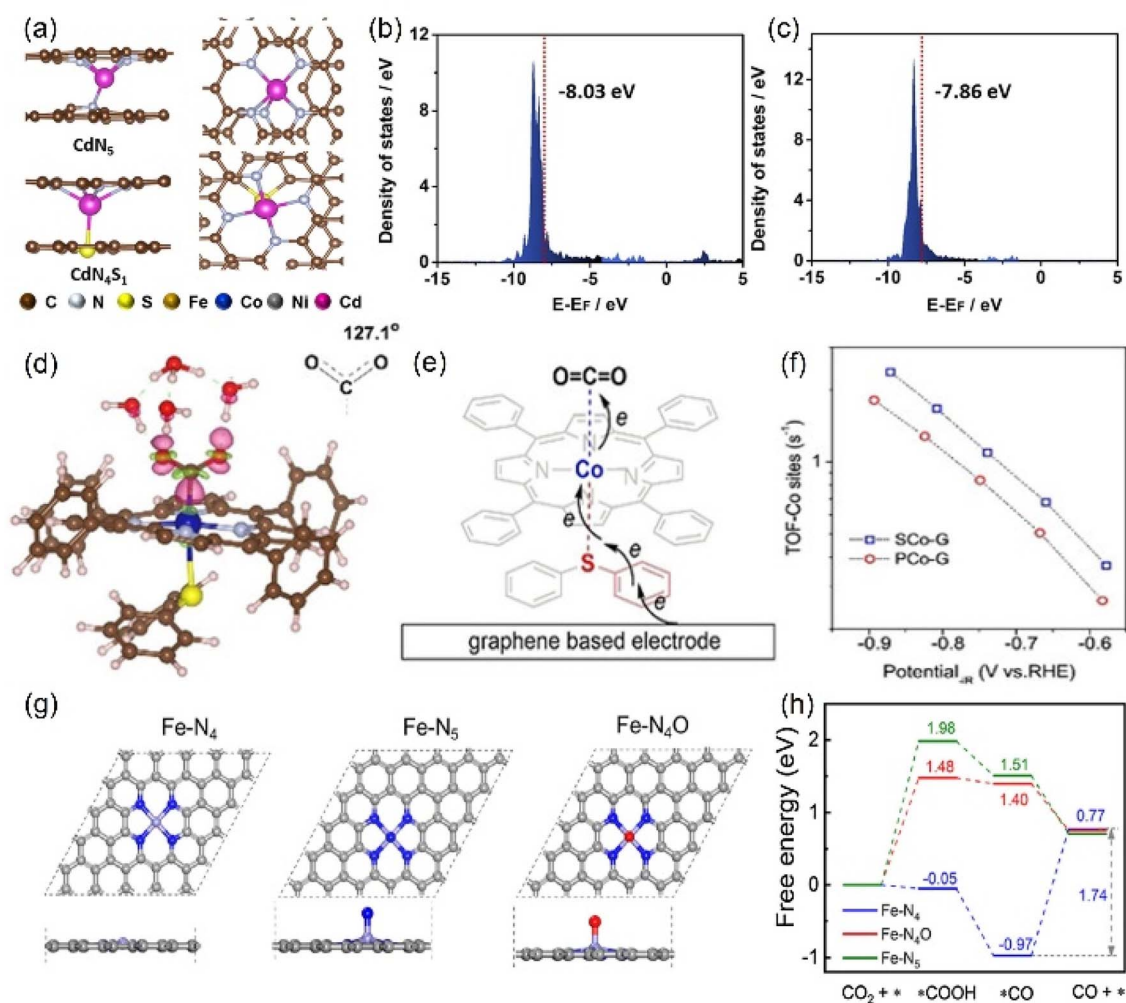


Fig. 16 (a) The side and top structures and (b) the partial density of states of Cd site of  $\text{CdN}_4\text{S}_1$  and  $\text{CdN}_5$  configurations (red line: the d-band center). (d) Charge density difference diagram exhibiting  $\text{CO}_2$  activation on the Co atom in  $\text{Co-N}_4\text{S}_1$ . (e) Schematic diagram of the possible electron transfer pathways of the  $\text{CO}_2$  activation from graphene,  $\text{Co-N}_4\text{S}_1$  to  $\text{CO}_2$ . (g) The side and top structures and (h) Gibbs free energy diagram of the  $\text{ECO}_2\text{RR}$  to  $\text{CO}$  of  $\text{Fe-N}_4$ ,  $\text{Fe-N}_5$  and  $\text{Fe-N}_4\text{O}$  configurations. (a–c) Reproduced with permission.<sup>143</sup> Copyright 2021, John Wiley and Sons Ltd. (d–f) Reproduced with permission.<sup>144</sup> Copyright 2020, John Wiley and Sons Ltd. (g and h) Reproduced with permission.<sup>145</sup> Copyright 2020, Elsevier.

atom to enhance the electron transfer capacity (Fig. 16d and e). The TOF value of  $\text{Co-N}_4\text{S}_1$  ( $2.4 \text{ s}^{-1}$ ) at  $-0.87 \text{ V}$  is 1.5 times that of  $\text{Co-N}_4$  (Fig. 16f).<sup>144</sup> In addition, when O is used as the axial ligand of the Fe center, it exhibits excellent stability at low potentials. This can be attributed to the fact that the adsorption energy of  $^*\text{CO}$  species on the  $\text{Fe-N}_4\text{O}$  configuration is much lower than that of  $\text{Fe-N}_4$  or  $\text{Fe-N}_5$ , which makes the precipitation process smoother (Fig. 16g and h).<sup>145</sup> More and more related studies have shown that it is infinitely possible to design different types of coordination environments to develop new areas of electrocatalytic  $\text{CO}_2\text{RR}$ . More in-depth research in this direction will be dominant in the future.

## 4. Categories of catalysts for $\text{ECO}_2\text{RR}$

Thanks to the indefatigable efforts of researchers, great achievements have been achieved in recent decades in

improving the activity of  $\text{ECO}_2\text{RR}$  catalysts. Herein, the most advanced and capable  $\text{ECO}_2\text{RR}$  catalysts are representatively classified as atomically-dispersed catalysts, alloys, MOFs and COFs, providing a comprehensive overview of their inherent characteristics and achievements in electrocatalytic performance. Herein, we present more intuitive summaries and comparisons of the cutting-edge  $\text{ECO}_2\text{RR}$  catalysts in Table 3 in combination with structure–activity optimization strategies to provide researchers with the most frontier research level and design inspiration.

### 4.1. Atomically-dispersed catalysts

Atomically-dispersed metal catalysts (ADMCs) are known to have the highest atomic utilization among common catalytic systems. Compared with bulk metal structures, ADCMs exhibit new or optimized electrocatalytic properties due to their unique geometric, electronic properties, and uniform active sites,



having been widely used in electrocatalytic CO<sub>2</sub>RR. However, owing to high cohesion energy and large surface tension, dispersed metal atoms tend to agglomerate and lose their catalytic activity.<sup>199</sup> The strong fixation of the conductive carrier is essential for maximizing the activity and stability of ADMCs.

**4.1.1. SACs for ECO<sub>2</sub>RR to generate CO.** Single-atom catalysts (SACs) are the first atomically-dispersed catalysts to be proposed and studied widely. Theoretical calculations have shown that most metal atoms, including s, d, ds, and p regions, have electrocatalytic CO<sub>2</sub>RR activity toward the product, mainly CO. However, the electrocatalytic activity needs to be improved, such as CO selectivity and catalytic stability. On carbon-based materials, metal atoms are mainly connected with the substrate through heteroatoms (N, O, S, P, *etc.*) to form stable SACs.<sup>200</sup> Changing the types and coordination environment of center metal atoms can improve the electrocatalytic CO<sub>2</sub> reduction activity.

Due to the non-delocalization characteristic of the 3s orbital, CO is less adsorbed on Mg than other transition metals (Fe, Co, *etc.*), which is beneficial for the high selectivity of CO.<sup>201</sup> According to the simulation of CO generation path, the energy barrier of CO desorption on Mg-C<sub>3</sub>N<sub>4</sub> was only 0.13 eV (Fig. 17a–c). The electron transfer number of Mg-C<sub>3</sub>N<sub>4</sub> to CO is 0.1 e, which is much smaller than the corresponding Fe-C<sub>3</sub>N<sub>4</sub> and Co-C<sub>3</sub>N<sub>4</sub> (Fig. 17d–f). However, the FE<sub>CO</sub> can reach 90% at large applied voltages. In addition, the SA Ca has almost no CO<sub>2</sub>RR activity due to the large activation barrier.

Zhao *et al.* synthesized Ni SAs/N-C by the calcination of Ni-MOF, in which the uniformly dispersed Ni-N<sub>3</sub>C<sub>1</sub> is the active center of electrocatalysis.<sup>202</sup> When the voltage is −0.89 V, the FE of CO<sub>2</sub> reduction to CO reaches a maximum of 71.9%. Further, a SAC named Ni-N<sub>3</sub>-C, where Ni is bonded to three N atoms and has a carbon defect site at an adjacent site, prepared by a two-step process of high-temperature annealing and ion exchange, showed enhanced CO selectivity.<sup>203</sup> The obvious unsaturated coordination greatly accelerated the rate-determining step (RDS), the formation of COOH\*, and the FE of CO reached 95.6%, higher than that of Ni-N<sub>4</sub> without carbon defects.

The controllable uniform reaction site represents high reaction selectivity. The precise control of the types of coordination nitrogen atoms (pyridine nitrogen, pyrrole nitrogen, graphite nitrogen, *etc.*) can further improve the unity of the coordination structure of metal atoms. By self-assembly, Zheng *et al.* used melamine and cyanuric acid as raw materials to obtain metallic SAs coordinated with four pyrrole nitrogen.<sup>80</sup> In the electrocatalytic CO<sub>2</sub>RR process, the FE (98.5%) of CO on pyrrole-type Ni-N<sub>4</sub> was higher than the corresponding Fe, Cu, and Co. Pyridine-type Fe-N<sub>4</sub> on C<sub>3</sub>N<sub>4</sub> also displayed high CO selectivity at −0.6 V.<sup>204</sup> Instead of pyridine nitrogen, high-valent Fe(III) is more easily stabilized by pyrrole nitrogen, exhibiting faster CO<sub>2</sub> adsorption and weaker CO adsorption.<sup>205</sup> During the electrocatalytic process, Fe could remain in its high valence and not be reduced due to the strong coupling effect. When the voltage was greater than −0.5 V, Fe lost a pyrrole N ligand and was reduced. The low-valence single Ni(I) atom, with 9 d electrons, exhibited high inherent CO<sub>2</sub> reduction activity, with FE<sub>CO</sub> of 97% and stability of up to 100 h at an overpotential of

0.61 V.<sup>206</sup> During the CO<sub>2</sub>RR process, the transfer of electrons from the Ni(I) orbital to the 2p orbital of carbon formed CO<sub>2</sub><sup>δ−</sup> species, causing the activation of CO<sub>2</sub> and lowering the barrier for CO<sub>2</sub> reduction. Using the template method, Li *et al.* synthesized a high-metal-content single-atom catalyst Co-N<sub>5</sub>/HNPCSSs, in which Co was coordinated with five nitrogen and uniformly dispersed on the hollow carbon sphere (Fig. 17g–j).<sup>131</sup> Over a wide voltage range, the catalyst produced CO with a selectivity of more than 90%, and the selectivity reached a maximum of 99.4% at −0.79 V. The improved CO selectivity was attributed to the strong adsorption of COOH\* and the suitable adsorption of CO\* at Co-N<sub>5</sub> sites (Fig. 17k). As the most used MOF precursor, ZIF-8 can effectively isolate the agglomeration of single atoms during calcination.<sup>207</sup> The Zn-N<sub>4</sub> site reduced the reaction barrier of \*COOH generation and converted CO<sub>2</sub> to CO with an FE of 95%.<sup>208</sup> Single Mn, Zn, Fe, or Cr atoms are all potential catalysts that can reduce CO<sub>2</sub> to CO.

Due to the participation of multiple electrons in adsorption and desorption reactions, rare-earth-based materials will produce strong adsorption with CO<sub>2</sub>RR intermediates, showing a poor electrocatalytic activity. However, owing to the strong metal-carrier interaction, rare earth metals can be easily fixed on the carrier, facilitating the synthesis of single atoms, which gives them CO<sub>2</sub>RR activity. Due to large atomic radii and abundant electron orbitals, isolated Sc and Y tend to adsorb at large defect sites and form five- or six-coordinated configurations. Liu *et al.* synthesized Sc- and Y-SACs (Y<sub>1</sub>/NC and Sc<sub>1</sub>/NC), where each metal atom was simultaneously bonded to three nitrogen atoms and three carbon atoms.<sup>209</sup> In the process of CO<sub>2</sub>RR, Y<sub>1</sub>/NC and Sc<sub>1</sub>/NC reached the highest FE<sub>CO</sub> of 88.3% and 81.3% at −0.58 V and −0.68 V, respectively.

**4.1.2. DACs for ECO<sub>2</sub>RR to generate CO.** Diatomic catalysts (DACs) and multi-atom catalysts are the extension of SACs, which provide more possibilities for the adsorption of reaction intermediates. Unlike SACs, the introduction of the second and the third metal atoms can not only further regulate the electronic structure but also add new adsorption active sites, breaking the limit of linear relationship. According to the types of metals, DACs are mainly divided into homologous binuclear and heterologous binuclear metals.<sup>210–212</sup>

The dispersion of Pd atoms with strong CO adsorption on the Au surface in the form of diatomic Pd–Pd would adjust the CO adsorption strength to moderate and further enhance the CO selectivity (Fig. 18a).<sup>213</sup> Pb<sub>2</sub> DACs could be prepared by anion replacement deposition, and the distance between Pd and Pd was 1.96 Å, indicating the formation of a dual-nuclear site.<sup>214</sup> At an applied voltage of −0.85 V, Pb<sub>2</sub> DACs presented high selectivity for CO with an FE of 98.2%, which was much higher than that of the corresponding single atom catalyst (65%) and nanostructured catalyst (80%). The CO poisoning reaction of Pd nanoparticles was not conducive to CO<sub>2</sub>RR, resulting in a large reaction barrier. However, for Pd-based atomically-dispersed catalysts, the activation of CO<sub>2</sub> to COOH\* was the RDS, and both isolated Pd<sub>1</sub> and Pd'<sub>1</sub> exhibited greater free energy of RDS than Pd<sub>2</sub>. The enhanced electrocatalytic activity was attributed to the electron transfer between Pd–Pd.



Table 3 Comparison of ECO<sub>2</sub>RR performance on advanced catalysts combined with optimization strategies

Catalyst	Optimization strategy	FE (%)	Current density (mA cm <sup>-2</sup> )	Applied potential (V vs. RHE)	Electrolyte	Device	Ref.
B-CuO	Modulating the electronic structure of the active center	C <sub>2+</sub> (62.1)	-139	-0.62	1 M KOH	Flow cell	146
Cu(B)		C <sub>2</sub> H <sub>4</sub> (52)	-70	-1.1	0.1 M KOH	H-cell	147
PDI@Cu(Cu-C)		CH <sub>4</sub> (38.9)	-145	-1.0	0.1 M KHCO <sub>3</sub>	Flow cell	148
Cu <sub>1.5</sub> /GDY		CH <sub>4</sub> (57.3)	-312	-1.7	1 M KOH	Flow cell	149
Cu-N-C-900		CH <sub>4</sub> (38.6)	-38.3	-1.6	0.1 M KHCO <sub>3</sub>	H-cell	150
PSB-CuN <sub>3</sub>		HCOO <sup>-</sup> (97.9)	-127.7	-1.1	0.5 M KHCO <sub>3</sub>	Flow cell	151
Cu-on-Cu <sub>3</sub> N		C <sub>2</sub> H <sub>4</sub> (39)	-23	-0.95	0.1 M KHCO <sub>3</sub>	H-cell	152
Cu <sub>3</sub> N <sub>x</sub>		C <sub>3</sub> H <sub>7</sub> OH (6)	-307	-1.15	1 M KOH	Flow cell	153
Cu <sub>3</sub> P		C <sub>2</sub> H <sub>4</sub> (56)	-0.5	-0.2	0.5 M KHCO <sub>3</sub>	H-cell	154
P <sub>0.075</sub> -Cu		HCOO <sup>-</sup> (8)	-17.57	-1.6	0.1 M KHCO <sub>3</sub>	H-cell	155
P-doped Cu		C <sub>2</sub> H <sub>4</sub> (30.7)	-210	—	1 M KOH	Flow cell	156
Oxide-derived Cu		C <sub>2</sub> H <sub>4</sub> (40)	-11	-1.0	0.1 M KHCO <sub>3</sub>	H-cell	157
CuO-derived Cu		C <sub>2+</sub> (60.1)	-400	—	1 M KOH	Flow cell	158
CuS <sub>x</sub> -DSV		C <sub>2</sub> (7)	-20	-1.05	0.1 M KHCO <sub>3</sub>	H-cell	159
Cu <sub>2</sub> S-Cu-V		C <sub>3</sub> H <sub>7</sub> OH (15.4)	-400	—	1 M KOH	Flow cell	160
SNC@Cu <sub>1.96</sub> S	C <sub>2+</sub> alcohol (32)	-21	-0.84	0.5 M KHCO <sub>3</sub>	H-cell	161	
Sm <sub>x</sub> -Cu <sub>y</sub>	HCOOH (92.1)	-300	—	1 M KOH	Flow cell	162	
Cu <sub>2</sub> -CuN <sub>3</sub>	C <sub>2</sub> H <sub>5</sub> OH (51)	-28.2	-1.1	0.1 M KHCO <sub>3</sub>	H-cell	163	
Cu-N-C	C <sub>2</sub> H <sub>5</sub> OH (55)	-16.2	-1.2	0.1 M CsHCO <sub>3</sub>	Flow cell	164	
Cu <sub>2</sub> P <sub>2</sub> O <sub>7</sub>	C <sub>2</sub> H <sub>4</sub> (41.8)	-200	—	0.1 M KOH	MEA-based	165	
V <sub>8c</sub> -Cu <sub>2-x</sub> Se	C <sub>2</sub> H <sub>5</sub> OH (68.1)	-10.96	-0.8	0.5 M KHCO <sub>3</sub>	H-cell	166	
Cu <sub>1.63</sub> Se(1/3)	CH <sub>3</sub> OH (77.6)	-41.5	-2.1	[Bmim]PF <sub>6</sub> (30 wt.)/CH <sub>3</sub> CN/ H <sub>2</sub> O (5 wt.)	H-cell	166	
BiCuSeO	HCOOH (93.4)	-267	-1.1	1 M KOH	Flow cell	167	
Cu <sub>2</sub> Se	CH <sub>3</sub> CH <sub>2</sub> OH (84)	-50	-0.6	0.3 M NaHCO <sub>3</sub>	H-cell	168	
Cu <sub>2</sub> Te	CH <sub>4</sub> (63)	-300	—	1 M KHCO <sub>3</sub>	Flow cell	169	
CuO <sub>x</sub> V <sub>o</sub>	C <sub>2</sub> H <sub>4</sub> (63)	-30	-1.4	0.1 M KHCO <sub>3</sub>	H-cell	170	
O <sub>2</sub> , 10 min plasma Cu	C <sub>2+</sub> (60)	—	—	0.1 M CsHCO <sub>3</sub>	H-cell	171	
e-CuOH/FCI	C <sub>2</sub> H <sub>4</sub> (36.3)	-18.5	-1.0	0.1 M KHCO <sub>3</sub>	H-cell	172	
Cu <sub>2</sub> O <sub>Cl</sub>	C <sub>3</sub> -C <sub>4</sub> (10)	-7	-1.6	0.1 M KCl	H-cell	173	
Cu <sub>2</sub> KI	C <sub>2</sub> H <sub>4</sub> (44.5)	-40	-1.15	0.1 M KHCO <sub>3</sub>	H-cell	174	
O <sub>2</sub> plasma-activated Cu foil	C <sub>2</sub> H <sub>4</sub> (60)	-2	-0.9	0.1 M KHCO <sub>3</sub>	H-cell	175	
V <sub>o</sub> -rich ZnO nanosheets	CO (83)	-16.1	-1.1	0.1 M KHCO <sub>3</sub>	H-cell	105	
Nb <sub>4</sub> N <sub>5</sub> -NO/NC	CO (91)	-2.8	-0.8	0.1 M KHCO <sub>3</sub>	H-cell	176	
Ni-N <sub>3</sub> -V	CO (90)	-65	-0.9	0.5 M KHCO <sub>3</sub>	H-cell	177	
Bi <sub>2</sub> S <sub>3</sub> -Bi <sub>2</sub> O <sub>3</sub> @rGO	HCOOH (90.1)	—	-0.9	0.1 M KHCO <sub>3</sub>	H-cell	178	
V <sub>o</sub> -SnO <sub>2</sub> /CF	HCOOH (86)	-30	-1	0.1 M KHCO <sub>3</sub>	H-cell	179	
H-InO <sub>x</sub> NRS	HCOOH (91.7)	—	-0.7	0.5 M KHCO <sub>3</sub>	H-cell	180	
SnO <sub>x</sub>	HCOOH (88.6)	-15	-0.98	0.5 M KHCO <sub>3</sub>	H-cell	181	





Table 3 (Contd.)

Catalyst	Optimization strategy	FE (%)	Current density (mA cm <sup>-2</sup> )	Applied potential (V vs. RHE)	Electrolyte	Device	Ref.
CdS		CO (100 ± 0.5)	-20.5	-1.1	0.5 M KHCO <sub>3</sub>	H-cell	182
Cu/CeO <sub>2-x</sub> HDs		CH <sub>4</sub> (54)	—	-1.2	0.1 M KHCO <sub>3</sub>	H-cell	183
CdS-CNTs		CO (92)	-11.4	-1.2	0.1 M KHCO <sub>3</sub>	H-cell	106
De-Al <sub>3</sub> Cu		CO (94.3)	—	-0.43	0.5 M KHCO <sub>3</sub>	H-cell	184
Cu <sub>v</sub> -Cu <sub>2</sub> O		C <sub>2</sub> H <sub>4</sub> (51)	-15.7	-0.76	0.1 M KHCO <sub>3</sub>	H-cell	185
Bi/Bi <sub>2</sub> O <sub>3</sub> -CP		HCOOH (90.4)	—	-0.87	0.5 M KHCO <sub>3</sub>	H-cell	186
Vo-rich SnO <sub>2</sub>		CO (92.5)	-44.2	-1.1	0.5 M KHCO <sub>3</sub>	H-cell	187
Iodide-mediated Cu		C <sub>2</sub> H <sub>4</sub> and oxygenates (25)	—	—	0.1 M KHCO <sub>3</sub>	H-cell	188
Cu-CuI	Strain engineering can break the queue of the original equilibrium between atoms to optimize the energy barrier of key reactive species	C <sub>2</sub> H <sub>4</sub> (71)	-832.4	-1.0	1 M KOH	Flow cell	189
Cu/Cu <sub>2</sub> OF		CH <sub>3</sub> COOH (27)	-15	-0.3	1 M KOH	Flow cell	190
Ag <sub>2</sub> S-Cu <sub>2</sub> O/Cu		CH <sub>3</sub> OH (67.4)	-122.7	-1.18	BMImBF <sub>4</sub> /H <sub>2</sub> O (molar ratio 1 : 3)	H-cell	191
Cu <sub>2</sub> O@Cu-MOF		CH <sub>4</sub> (63.2)	-14	-1.71	0.1 M KHCO <sub>3</sub>	H-cell	192
Cu(OH) <sub>2</sub> /CuO		C <sub>2</sub> H <sub>4</sub> (64.5)	-26.2	-0.9	0.1 M KHCO <sub>3</sub>	H-cell	173
3D dendritic Cu-Cu <sub>2</sub> O/Cu		C <sub>2</sub> (80.7)	-11.5	-0.4	0.1 M KCl	H-cell	193
Ag-Cu <sub>2</sub> O <sub>ppb</sub>		C <sub>2</sub> H <sub>5</sub> OH (34.15)	-4	-1.2	0.2 M KCl	H-cell	194
Tin-based oxides SnO <sub>x</sub> /Sn		HCOO <sup>-</sup> (64)	-3	-1.399	0.1 M KHCO <sub>3</sub>	H-cell	195
GDE							
Pd/SnO <sub>2</sub> NSs		CH <sub>3</sub> OH (55)	-1.45	-0.24	0.1 M NaHCO <sub>3</sub>	H-cell	196
SnO <sub>2</sub> -0.8/C-Cu		CO (93)	-4.6	-0.7	0.5 M KHCO <sub>3</sub>	H-cell	122
Cu/SnO <sub>x</sub> -CNT (6.2 SnO <sub>x</sub> )		CO (89)	-11.3	-0.99	0.1 M KHCO <sub>3</sub>	H-cell	197
Cu/SnO <sub>x</sub> -CNT (30.2 SnO <sub>x</sub> )		HCOOH (77)	-4	-0.99	0.1 M KHCO <sub>3</sub>	H-cell	197
Zn <sub>2</sub> SnO <sub>4</sub> /SnO <sub>2</sub>		HCOOH (77)	-5.77	-1.08	0.1 M KHCO <sub>3</sub>	H-cell	198



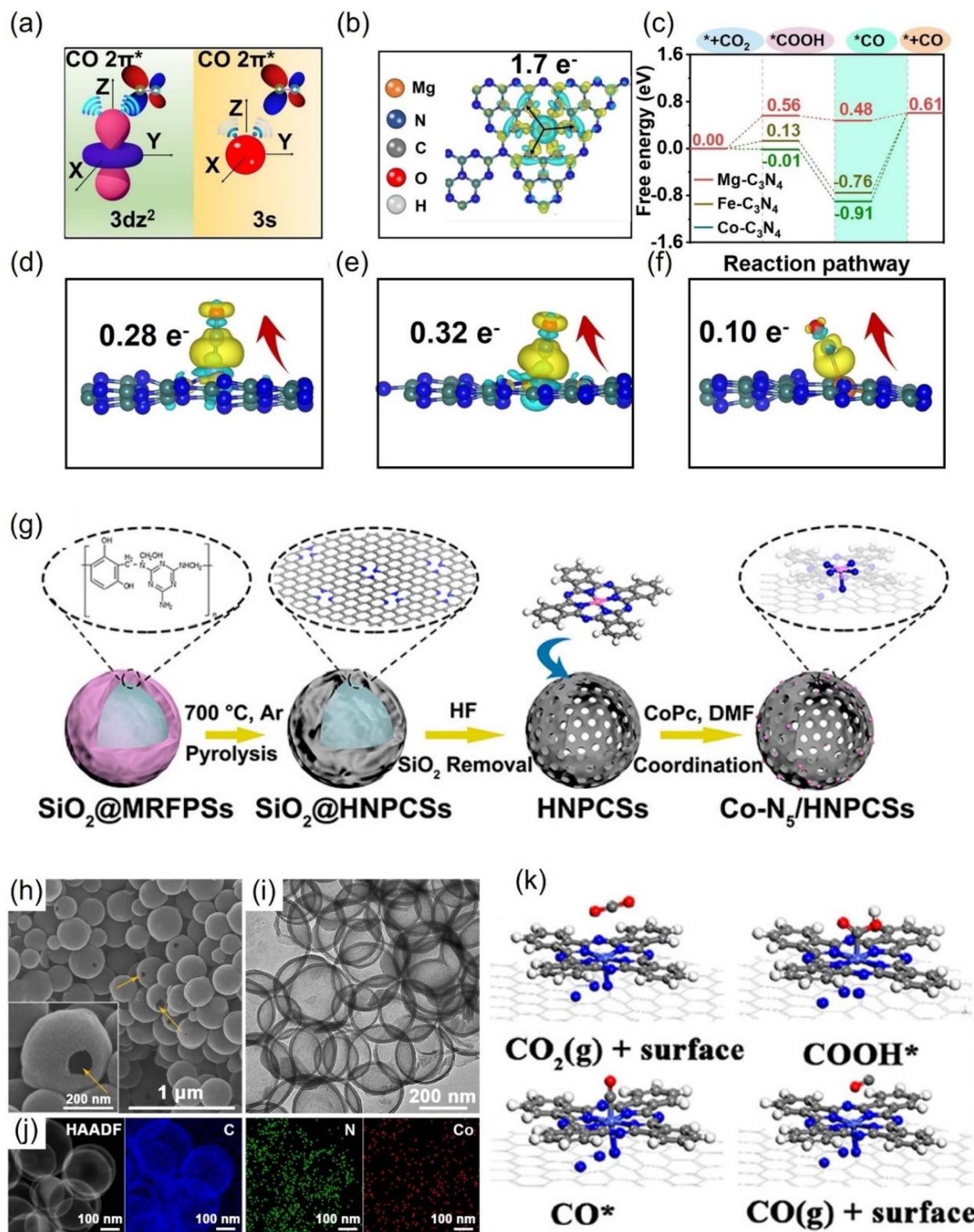
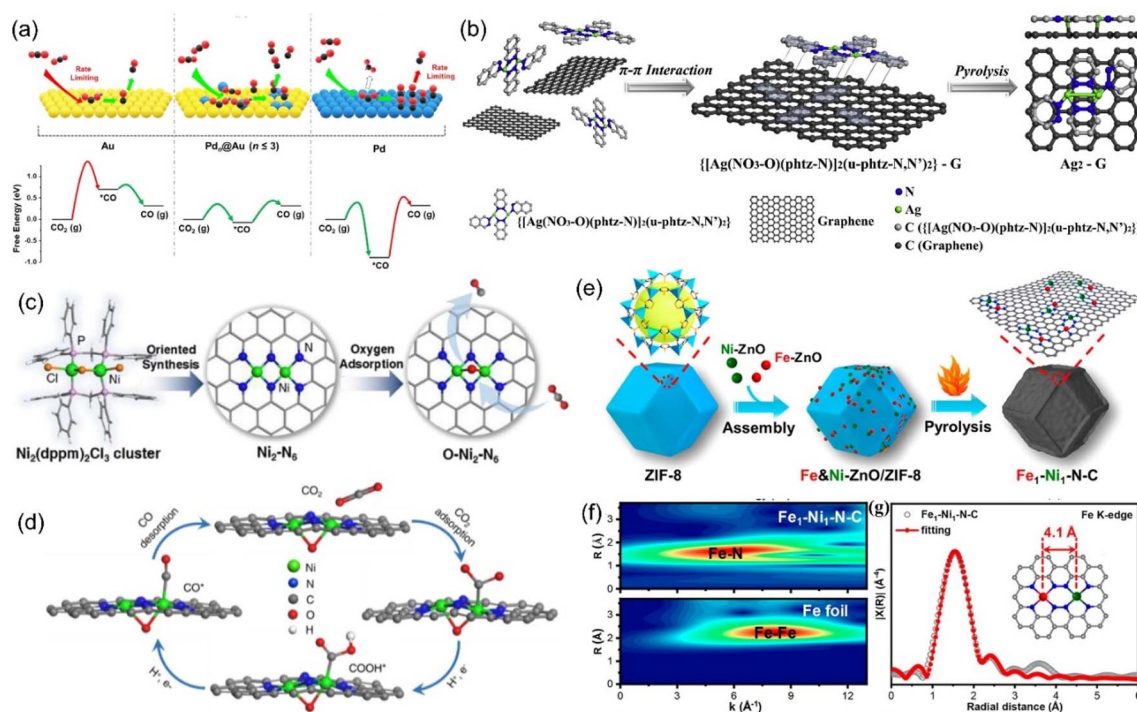


Fig. 17 (a) Comparison of the schematic diagram for CO adsorbed on  $3d_{z^2}$  and  $3s$  orbitals. (b) The charge density differences and Bader charge transfer for  $\text{Mg-C}_3\text{N}_4$ . (c) Free energy diagram and (d–f) charge density differences and Bader charge transfer for CO adsorbed on  $\text{Co-C}_3\text{N}_4$ ,  $\text{Fe-C}_3\text{N}_4$  and  $\text{Mg-C}_3\text{N}_4$ . (g) Schematic illustration, (h) SEM, (i) TEM, (j) HAADF-STEM and EDS images and (k) optimized structures for the intermediates. (a–f) Reproduced with permission.<sup>201</sup> Copyright 2021, Wiley-VCH GmbH. (g–k) Reproduced with permission.<sup>131</sup> Copyright 2018, American Chemical Society.





**Fig. 18** (a) Illustration of the concept using atomically-dispersed Pd sites on Au surface to enhance  $\text{CO}_2$  reduction. (b) Synthetic illustration of the  $\text{Ag}_2\text{-G}$  catalyst. (c) The synthesis process of the  $\text{Ni}_2\text{-N}_6$  catalyst and (d) proposed reaction pathways on  $\text{O-Ni}_2\text{-N}_6$ . (e) Synthetic illustration of  $\text{Fe}_1\text{-Ni}_1\text{-N-C}$ ; (f) WT plots for Fe element. (g) Fe K-edge EXAFS spectrum. (a) Reproduced with permission.<sup>213</sup> Copyright 2019, American Chemical Society. (b) Reproduced with permission.<sup>215</sup> Copyright 2020, Elsevier B.V. All rights reserved. (c and d) Reproduced with permission.<sup>218</sup> Copyright 2021, American Chemical Society. (e–g) Reproduced with permission.<sup>221</sup> Copyright 2021, American Chemical Society.

The  $\text{AgN}_3\text{-AgN}_3$  sites can be obtained by fixing a binuclear Ag precursor to graphene through the  $\pi\text{-}\pi$  interaction (Fig. 18b).<sup>215</sup> Two Ag atoms interact with C and O at the same time, stabilizing the  $\text{CO}^*$  intermediate and reducing the reaction barrier for the formation of  $^*\text{COOH}$ . At  $-0.7$  V, the current density of  $11.87$   $\text{mA cm}^{-2}$  could be achieved, and the FE of CO reached 93.4%. When metal oxides or sulfides and alloys are used as the support, dispersed atom-based catalysts are more likely to achieve high loading capacity. Jiao *et al.* synthesized Cu-APC, with atomic copper pair ( $\text{Cu}_1^0\text{-Cu}_1^{x+}$ ) sites by adding Cu onto Te defects of the  $\text{Pd}_{10}\text{Te}_3$  alloy nanowires.<sup>216</sup> In the copper pair,  $\text{Cu}_1^{x+}$  adsorbed water molecules in the electrolyte and promoted the adsorption and activation of  $\text{CO}_2$  at the adjacent  $\text{Cu}_1^0$  sites. In  $0.2$  M  $\text{NaHCO}_3$ , the  $\text{FE}_{\text{CO}}$  of  $0.10\%$ -Cu-APC was 92%, while the original APC mainly showed HER, implying that the  $\text{Cu}_1^0\text{-Cu}_1^{x+}$  was the active site of  $\text{CO}_2\text{RR}$ .

The synergistic effect of heteronuclear metal atoms on the electronic structure is obvious. Without direct bonding, M1 and M2 are merely adjacent and are connected by bridging bonds ( $\text{M1-X-M2}$ ), exhibiting enhanced  $\text{CO}_2\text{RR}$  activity than the individual M1 or M2. The active sites of catalysts can change from a single atom to an atomic pair by changing the synthetic conditions. For example, when Fe-ZIF-8 was calcined in pure argon, the product was SAC  $\text{Fe}_1\text{-N}_4\text{-C}$ , and the iron content was 0.155 wt%.<sup>217</sup> However, when hydrogen was introduced into argon, Fe atoms underwent a transition from single-core to dual-core. When the hydrogen content was 5%, 80% of the iron

in the product was in the form of atomic pair ( $\text{Fe}_2\text{-N}_6$ ), and the iron content was 0.313 wt%. The orbital coupling between the two Fe sites reduced the energy gap between the antibonding state and the bonding state in  $^*\text{CO}$  adsorption, improving the selectivity of electrocatalytic products. Similarly,  $\text{Ni}_2\text{-N}_6$  was successfully synthesized using  $\text{Ni}_2$  organic molecules as the precursor, where two of the Ni atoms share two nitrogen atoms (Fig. 18c).<sup>218</sup> In the process of  $\text{CO}_2$  adsorption, the two complex-unsaturated Ni atoms tended to adsorb oxygen in the solution to form an oxygen bridge bond ( $\text{Ni-O-Ni}$ ), generating more active  $\text{O-Ni}_2\text{-N}_6$  (Fig. 18d).

Due to the strong Fe-CO interaction, the desorption of  $\text{CO}^*$  on Fe-SACs was the RDS for  $\text{CO}_2\text{RR}$ , and the selectivity of Fe-N-C for CO was only 80%.<sup>219</sup> With the assistance of Zn, the Ni-Fe atomic pair was successfully synthesized with ZIF-8, where the distance between Fe and Ni was 4.1 Å (Fig. 18e–g). After the introduction of Ni, the charge transfer of Fe to CO in the Fe-Ni- $\text{N}_6$  catalyst was less than that in the corresponding catalyst without Ni. In  $\text{Fe}_1\text{-Ni}_1\text{-N-C}$ , the adsorption of  $\text{CO}_2$  occurred at the Fe site, while the adjacent Ni atom promoted the formation of  $\text{COOH}^*$  on the iron atom through a remote electron interaction *via* the N atom. At a low voltage of  $-0.5$  V,  $\text{Fe}_1\text{-Ni}_1\text{-N-C}$  still has 96.2% FE against CO. When the atomic pair was composed of Ni and Zn atoms, Ni was the main adsorption site. The addition of Zn at the Ni site reduced the gap between the d band center of Ni and the Fermi level, enhanced the bonding between the metal and C, and presented an obvious





acceleration effect in both kinetic and thermodynamic aspects.<sup>220</sup> The FE for CO was more than 90% in the wide voltage range ( $-0.5$  to  $-1.0$  V), and the maximum reached 99%.

From the view of theoretical calculations, the in-depth analysis of the nature of ECO<sub>2</sub>RR activity gain in polymetallic systems can be performed. Atomic-level control of the coordination environment and electron distribution of electrocatalysts is an effective strategy to improve the electrocatalytic performance, but there are still significant challenges.<sup>222</sup> Previous work has shown that synergistic interactions between atoms in a catalyst can locally tune the electronic structure, weakening the adsorption energy of the reaction intermediates and effectively lowering the energy barrier of the catalytic reaction.<sup>223</sup> Theoretical calculations showed that the co-catalytic strategy affects the adsorption or desorption of adsorbates on the catalyst surface, influencing the d-band centers of the metal atoms and thus changing the free energy barriers.<sup>220</sup> Lu *et al.* used nickel–zinc diatomic coordination to change the d-state of

the metal atoms, resulting in significantly enhanced synergistic effect compared to monoatomic catalysts. DFT calculations showed that this synergistic effect enhances the catalytic performance due to the reduction of the distance between the center of the d-band of Ni–Zn orbitals and Fermi energy level and the enhancement of the intermediate's electronic interactions with the active center (Fig. 19a). This lowers the free energy barrier in the thermodynamic pathway, reduces the activation energy, and strengthens the metal–carbon bond in the kinetic pathway. Ni–Zn diatomic catalyst can achieve 99% Faraday efficiency at  $-0.8$  V.<sup>220</sup> Wang *et al.* designed an efficient catalyst with CoPc traced on Fe–N–C. After the positioning of CoPc molecules, the synergistic interaction resulted in the movement of the d-band of the Fe center toward the Fermi energy level, which enhanced the reactivity of the Fe center, and this electronic interaction was reflected in the adsorption of reactive intermediate species (Fig. 19b and c). As a result, CO desorption on the catalyst's surface was promoted, and the

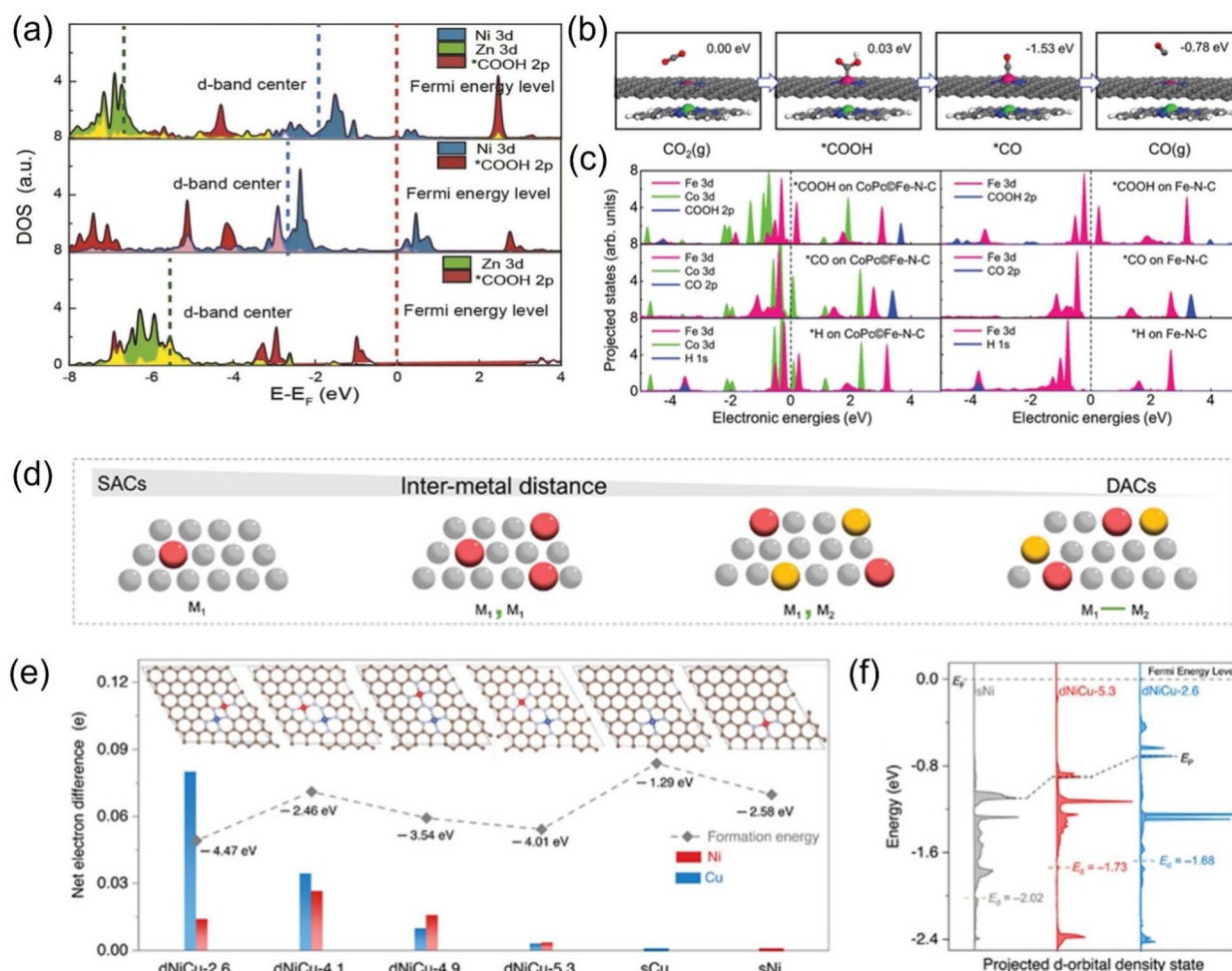


Fig. 19 (a) Projected DOS (PDOS) for Zn/Ni 3d orbitals and oxide 2p orbitals in COOH. (b) Schematic atomic structure of the CO<sub>2</sub>RR process on the Fe site in CoPc@Fe-N-C (C: gray; N: blue; O: red; H: white; Fe: pink; Co: green). (c) PDOS of adsorption structures of \*COOH, \*CO, and \*H on CoPc@Fe-N-C and Fe-N-C. (d) Schematic of SACs and DACs showing the change in the site proximity with different models. (e) Net electron difference of Ni and Cu sites in different dNiCu models. (f) Calculated DOS diagram of the Ni d-orbital for dNiCu-5.3, dNiCu-2.6, and sNi models. (a) Reproduced with permission.<sup>220</sup> Copyright 2021, Wiley-Blackwell. (b and c) Reproduced with permission.<sup>224</sup> Copyright 2019, Wiley-Blackwell. (d–f) Reproduced with permission.<sup>225</sup> Copyright 2023, Wiley-Blackwell.





competing HER on the Fe-N site was suppressed, realizing a high CO Faraday efficiency.<sup>224</sup> Qiao *et al.* investigated the relationship between synergistic and intermetallic interactions using a combination of theoretical simulations and experiments. In the case of NiCu DACs, the electronic contribution from the Cu center is transferred through the NC substrate to the Ni center and finally reaches the \*COOH intermediate. This electron transfer through the structure is likely to be the result of non-bonding synergies between neighboring DACs (Fig. 19d-f). Moreover, the synergistic effect modulates the electronic structure and promotes intermediate layer adsorption, thus improving the electroreduction activity and selectivity.<sup>225</sup>

**4.1.3. ADMCs for ECO<sub>2</sub>RR to generate other products.** In addition to CO, atomically-dispersed catalysts can catalyze CO<sub>2</sub> reduction to produce higher value products such as formic acid, methane, and ethanol. The p-block metal, Sb, Sn, Bi, and In can be used for the formation of formic acid.<sup>84,226</sup> By freeze-drying, Zu *et al.* synthesized a kilogram-scale Sn-SAC, in which positively charged Sn atoms were uniformly dispersed onto N-doped graphene (Fig. 20a-c).<sup>227</sup> At a small overpotential of 60 mV, the Sn-SAC reduced CO<sub>2</sub> to formate on account of both enhanced CO<sub>2</sub> adsorption and diminished HCOO\* adsorption. Mo-based SACs have the potential to produce high-value formate.<sup>228</sup> For multiple electron transfer products and C<sub>2+</sub> products, dispersed

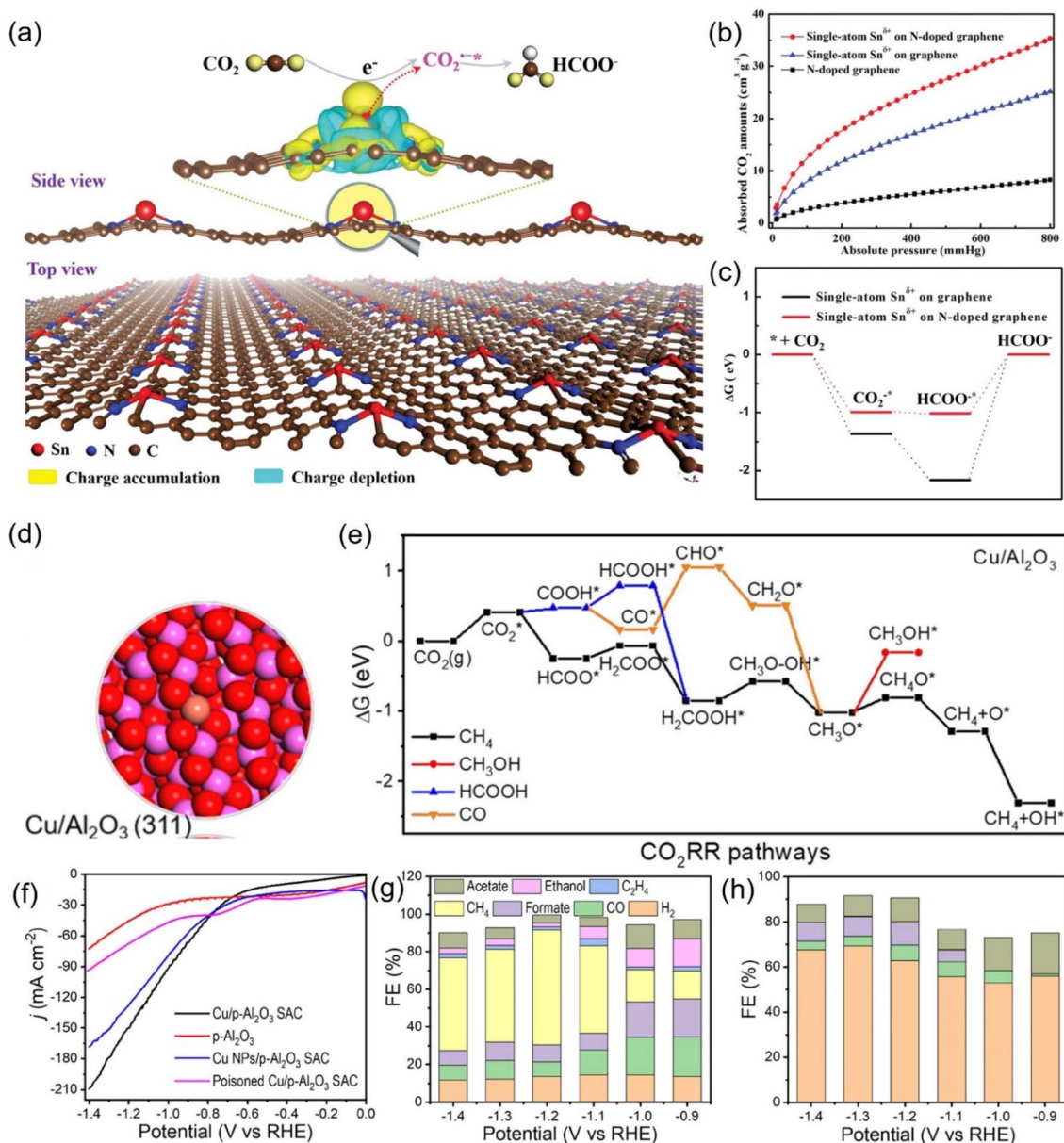


Fig. 20 (a) 3D differential charge densities of single-atom Sn<sup>δ+</sup> on N-doped graphene for CO<sub>2</sub>RR into formate. (b) CO<sub>2</sub> adsorption isotherms and (c) calculated free energy diagrams. (d) Electronic structure of Cu/Al<sub>2</sub>O<sub>3</sub> SAC. (e) Calculated free-energy diagrams for the CO<sub>2</sub>RR over Cu/Al<sub>2</sub>O<sub>3</sub> SAC. (f) LSV curves and FEs of various products for (g) Cu/p-Al<sub>2</sub>O<sub>3</sub> SAC and (h) p-Al<sub>2</sub>O<sub>3</sub>. (a-c) Reproduced with permission.<sup>227</sup> Copyright 2019, Wiley-Blackwell. (d-h) Reproduced with permission.<sup>229</sup> Copyright 2021, American Chemical Society.





alloying with a high faradaic efficiency of  $\sim 96\%$  at  $1 \text{ A cm}^{-2}$ .<sup>232</sup> What counts is that isolated Pd atoms were not active sites but rather acted more as modulators to adjust the local geometric and electronic structure of the neighboring Cu sites, making them highly selective and active for formate evolution. Shen *et al.* synthesized Zn single-atom alloyed metallic Bi (SAA-Zn<sub>1</sub>Bi), an ideal CO<sub>2</sub>RR catalyst screened under the guidance of DFT calculations for the production of formate, by a two-step *in situ* electrochemical reduction strategy (Fig. 21a).<sup>233</sup> Wang *et al.* accelerated the prediction of Cu-based single-atom alloy catalysts for CO<sub>2</sub>RR by machine learning.<sup>234</sup> Several SAAs, including PCu, AgCu, GaCu, ZnCu, SnCu, GeCu, InCu and SiCu, were identified as promising CO<sub>2</sub>RR catalysts through the high-throughput calculations of 2669 CO adsorption configurations on 43 types of Cu-based SAAs with various surfaces.

**4.2.2. Bimetallic/trimetallic alloys.** The effective electronic interactions between two/three metals and the special interfacial structure in bimetallic/trimetallic catalysts often make them exhibit better performance.<sup>235</sup> Inspired by the motivation, the increasing attention has been concentrated on the development of bimetallic/trimetallic alloys, showing promising catalytic activity for CO<sub>2</sub>RR. For example, Kim *et al.* fabricated Cu<sub>x</sub>Ir<sub>1-x</sub> alloy NPs with oxophilic Ir-rich surfaces to convert CO<sub>2</sub> into high value C<sub>4</sub> product *t*-BuOH [(CH<sub>3</sub>)<sub>3</sub>COH] with an FE of 14.8% at a  $j_{\text{partial}}$  of  $0.207 \text{ mA cm}^{-2}$ , which showed the best performance toward C<sub>4</sub> production so far.<sup>236</sup> Furthermore, they proposed a probable mechanism of *t*-BuOH formation (Fig. 21b). The strong electronic interactions between Cu and Ir as well as the high pro-oxidative nature of Ir-rich surfaces promoted the generation of C<sub>4</sub>, which enhanced the binding strength of the oxygen-bound intermediates. Okatenko *et al.* reported that CuGa alloy NPs containing 17 at% Ga preserved most of their CO<sub>2</sub>RR activity for at least 20 h, which was attributed to the higher oxophilicity and lower electronegativity of Ga, reducing the propensity of Cu to oxidize at open-circuit potential (ocp) and enhancing the bond strength in the alloyed nanocatalysts (Fig. 21c).<sup>237</sup> In addition, Chen *et al.* synthesized several Cu<sub>x</sub>Zn<sub>y</sub>Mn<sub>z</sub> ternary alloy electrocatalysts and tuned the surface coverage of \*CO and \*H, including Cu<sub>8</sub>-ZnMn, Cu<sub>8</sub>Zn<sub>6</sub>Mn and Cu<sub>8</sub>ZnMn<sub>2</sub>, by varying the doping amounts of Zn and Mn.<sup>238</sup> In which, the Cu<sub>8</sub>ZnMn catalyst presented a high CO<sub>2</sub>-to-CH<sub>4</sub> partial current density, while the Cu<sub>8</sub>Zn<sub>6</sub>Mn catalyst exhibited a high CO<sub>2</sub>-to-C<sub>2</sub>H<sub>4</sub> partial current density. Meanwhile, they found that the increase in the \*H coverage allowed promotion of CH<sub>4</sub> and H<sub>2</sub> formation, while the increase in the \*CO coverage facilitated the production of C<sub>2</sub>H<sub>4</sub> and CO.

**4.2.3. High-entropy alloys.** High-entropy alloys (HEAs) have emerged as a novel material in the field of electrocatalysis, showing excellent performance for CO<sub>2</sub>RR, which is related to the intrinsic properties such as high entropy effect, lattice distortion, sluggish diffusion and cocktail effect.<sup>239</sup> Nellaippan *et al.* synthesized AuAgPtPdCu for the conversion of CO<sub>2</sub> into gaseous hydrocarbons (CO, CH<sub>4</sub>, C<sub>2</sub>H<sub>4</sub>, and H<sub>2</sub>) with an FE of about 100% (Fig. 21d).<sup>240</sup> Although many elements were present in the catalyst, the electrocatalytic activity was predominantly described by the presence of redox-active Cu metal (Cu<sup>2+</sup>/Cu<sup>0</sup>),

and other metals only provided a synergistic effect. Cavin *et al.* predicted four HEAs, (MoWNBv)S<sub>2</sub>, (MoWNBt)S<sub>2</sub>, (MoWVNBt)S<sub>2</sub> and (MoVNBt)S<sub>2</sub>, subsequently synthesized the first three of these alloys with approximately equimolar stoichiometries and found that (MoWVNBt)S<sub>2</sub> HEA showed an exceptionally high electrocatalytic performance for CO<sub>2</sub> conversion to CO (Fig. 21e).<sup>241</sup> Besides, Roy *et al.* used screening criteria considering pure Cu (111) surface as a reference catalyst and found 34 active and selective HEA catalysts for CH<sub>3</sub>OH formation from the entire CuCoNiZnSn-based data set with the help of contour plots for the adsorption energies of \*CO, \*H<sub>2</sub>CO, \*H, and \*O.<sup>242</sup>

### 4.3. Metal-organic frameworks

It is well known that porous carbon-based materials with good chemical and thermal stability are favorable catalysts or supports for CO<sub>2</sub> capture.<sup>243,244</sup> Among porous carbon-based materials, MOFs are porous materials with well-defined crystallinity constructed from a diversity of organic linkers and feasible synthesis methods.<sup>245,246</sup> MOFs are superb catalyst templates due to their outstanding physicochemical stability, structure diversity, highly ordered porous structure, uniform pore sizes and environments, high internal surface areas, and functional organic linkers.<sup>247,248</sup> Benefiting from these unique physical and chemical properties, MOF derivatives exhibit the superiorities of higher stability, conductivity, and catalytic activity, which have been widely applied in CO<sub>2</sub>RR.

**4.3.1. Zinc-based MOFs.** Zinc-based MOFs were historically reported to catalyze CO<sub>2</sub>-to-CO conversion, and Zn is a promising metal to replace precious metals in CO<sub>2</sub>RR. The tuning of peripheral components, such as ligands and heteroatom doping, has been studied in the context of CO<sub>2</sub>RR.<sup>202</sup> Al-Attas and colleagues synthesized Zn-based MOFs containing different azolate functional ligands (1,2,4-triazole (Calgary Framework 20, CALF20)) and 2-methylimidazole (zeolitic imidazolate framework-8, ZIF-8) and found that CALF20 showed the highest CO partial current density of  $53.2 \text{ mA cm}^{-2}$ , with faradaic efficiency of  $\sim 94\%$  at  $-0.97 \text{ V}$  (*versus* RHE) and a turnover frequency (TOF) of  $1360.8 \text{ h}^{-1}$  due to faster charge transfer (Fig. 22a-c).<sup>249</sup> Zinc imidazolate framework-8 (ZIF-8) is a subclass of zinc-based MOF based on zeolite topologies and containing Zn<sup>2+</sup> and imidazolate ligands as the building units. The CO<sub>2</sub> reduction performance of ZIF-8 can be tuned *via* heteroatom doping, such as N-,<sup>250</sup> Fe-,<sup>251</sup> Co-,<sup>134</sup> and Ni-doping.<sup>202</sup> Qiu and co-workers adopted Fe, N co-doping to enhance the CO<sub>2</sub>RR reactivity of ZIF-8.<sup>252</sup> An increase in the FE and current density for CO production from *ca.* 75.0 to 98.8% in a concentrated KHCO<sub>3</sub> solution ( $1 \text{ mol L}^{-1}$ ) was observed, and the total current densities are more than 3 times higher than those of the less porous ones for electrochemical CO<sub>2</sub> reduction (Fig. 22d and e).

**4.3.2. Copper-based MOFs.** Cu-based nanomaterials are the most effective electrocatalysts due to their possible production of various hydrocarbon fuels including HCOOH, CO, CH<sub>4</sub>, C<sub>2</sub>H<sub>4</sub>, C<sub>2</sub>H<sub>5</sub>OH, and even C<sub>3</sub>H<sub>7</sub>OH.<sup>253</sup> Cu-BTC is a class of Cu-MOF formed by the self-assembly of Cu precursor dissolved in *N,N*-





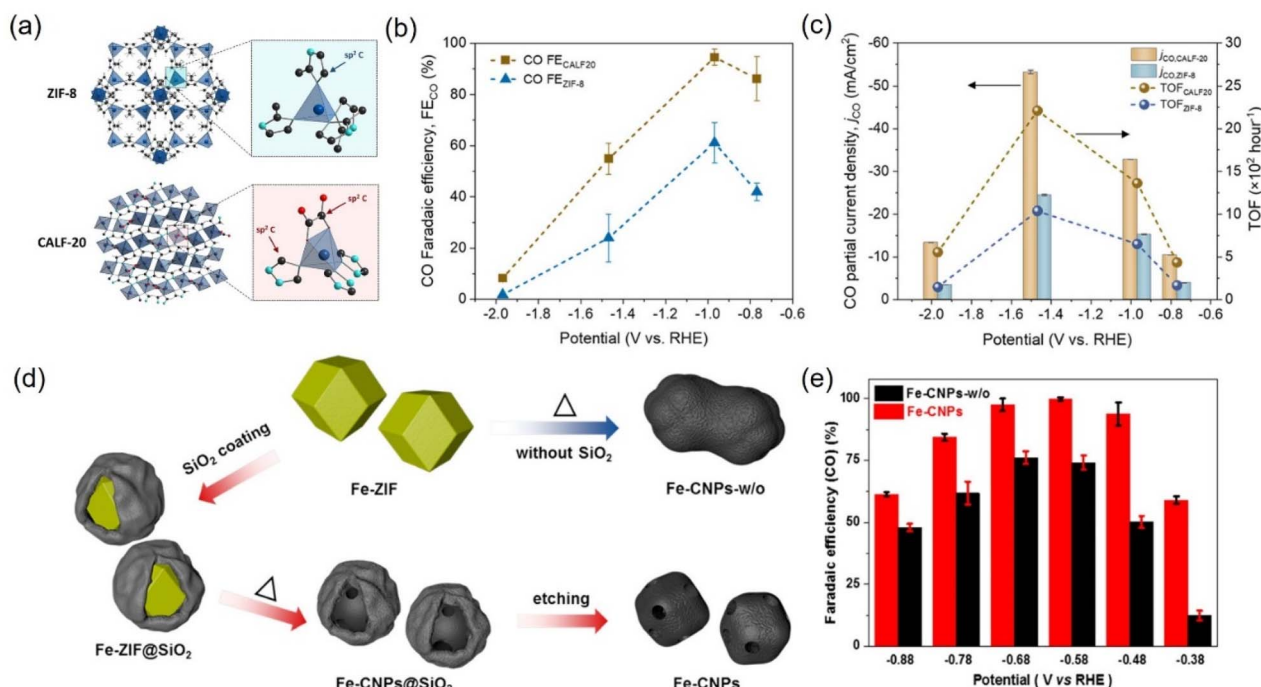


Fig. 22 (a) Schematic illustration of the crystal structure of ZIF-8 and CALF20. (b) FE<sub>CO</sub> and (c) CO partial current densities and TOF at different applied potentials for CALF20 and ZIF-8 in 1.0 M KOH. (d) Synthetic illustration of Fe-CNPs and Fe-CNPs-w/o. (e) FE<sub>CO</sub> at different potentials. (a–c) Reproduced with permission.<sup>249</sup> Copyright 2021, American Chemical Society. (d and e) Reproduced with permission.<sup>252</sup> Copyright 2019, American Chemical Society.

dimethylformamide (DMF) with benzene-1,3,5-tricarboxylic acid (H<sub>3</sub>BTC). Fang and co-workers used Cu-BTC as a sacrificial template to synthesize a series of Cu-carbon-based catalysts (Cu-pC, Cu<sub>2</sub>O-pC, and Cu<sub>2</sub>O/Cu-pC) with various valence states and mesoporous structures and found that Cu<sub>2</sub>O/Cu-pC with higher oxidation state can effectively enhance the CO<sub>2</sub>RR activity.<sup>254</sup> In addition, multi-site tandem electrocatalytic CO<sub>2</sub> reduction can be realized by tuning the geometry of Cu-BTC. Cao *et al.* prepared a series of Cu-based nanoreactors by adjusting the geometrical morphology of MOF precursors. Among them, the cuboctahedron nanoreactor containing Cu-N<sub>4</sub>/Cu<sub>2</sub>O/Cu multiple active sites exhibited excellent CO<sub>2</sub>RR selectivity towards the deep reduction product (80%) at a high current density (Fig. 23a and b).<sup>255</sup> Because Cu edge atoms prefer to adsorb protons in water, single metal Cu tends to show intense activity for the paradoxical reaction (HER) rather than for the CO<sub>2</sub>RR.<sup>256</sup> Cu–In bimetallic catalysts were prepared by pyrolyzing Cu–In MOF (Cu–In BTC) for the CO<sub>2</sub>RR (Fig. 23c). Cu<sub>90</sub>In<sub>10</sub>/C exhibits up to 85% selectivity of CO at –0.75 V *versus* RHE, higher than that of 3.1% and 10.8% for Cu/C and In/C, respectively.<sup>257</sup> The alkaline microenvironment during the CO<sub>2</sub>RR process rapidly destroys the Cu–O coordination bond of MOF, leading to the rapid aggregation of *in situ*-generated Cu-based nanoclusters and thus leading to the gradual loss of the CO<sub>2</sub>RR activity.<sup>258</sup> Meanwhile, Cu–N coordination is more stable than Cu–O coordination in MOFs, which is attributed to the matching between Cu<sup>2+</sup> as a borderline acid and N-heterocycle as borderline bases.<sup>258</sup> Gu *et al.* prepared highly active Cu/Cu<sub>2</sub>O nanoclusters *via in situ* electrochemical reconstruction using Cu–N coordinated MOF CuPZ<sub>2</sub> as precursors for the highly selective

C<sub>2</sub>H<sub>4</sub> synthesis, showing a faradaic efficiency of  $70.2 \pm 1.7\%$  toward C<sub>2</sub>H<sub>4</sub> with a partial current density of  $12.38 \text{ mA cm}^{-2}$  at –1.03 V *vs.* RHE in the CO<sub>2</sub>RR. *In situ* infrared spectroscopy with the observation of \*CO\*CO and \*CO\*COH intermediates confirmed the C<sub>2</sub>H<sub>4</sub> formation pathway, while *in situ* Raman spectroscopy and HRTEM evidenced that the coexisting Cu<sub>2</sub>O and Cu nanoclusters were the active sites (Fig. 23d and e).<sup>258</sup> Besides, Cu-based MOF (MOF-74) was used as the precursor of highly isolated Cu NPs to achieve enhanced CH<sub>4</sub> production in the CO<sub>2</sub>RR.<sup>245</sup> Furthermore, Irabien *et al.* tested the ECO<sub>2</sub>RR catalytic activity of various Cu-based organic porous materials, including HKUST-1 MOF, CuAdeAce MOF, CuDTA mesoporous metal–organic aerogel (MOA) and CuZnDTA MOA, verifying their ECO<sub>2</sub>RR application potential in gas diffusion electrodes (GDEs).<sup>13</sup> Among them, the GDEs constructed by HKUST-1 and CuZnDTA can utilize and convert CO<sub>2</sub> more efficiently into liquid methanol/ethanol products, and the Faraday efficiency of ethanol with high economic value can be as high as 15.9% and 9.9%, respectively, which can be attributed to the unsaturated coordination environment of the porous metal–organic frameworks. Notably, when the conversion rate was normalized to the active metal surface available for each material, the ECO<sub>2</sub>RR activity of CuAdeAce was second to none. The donor ligand-constructed paddle-wheel motifs play an important role in stabilizing the square plane coordination geometry around the Cu<sup>2+</sup> atom, which allows for the generation of open metal sites throughout the porous network that is prone to strong interaction with guest molecules. Since the local structure of the metal–organic porous material is hard to be destroyed, even though the crystallinity of



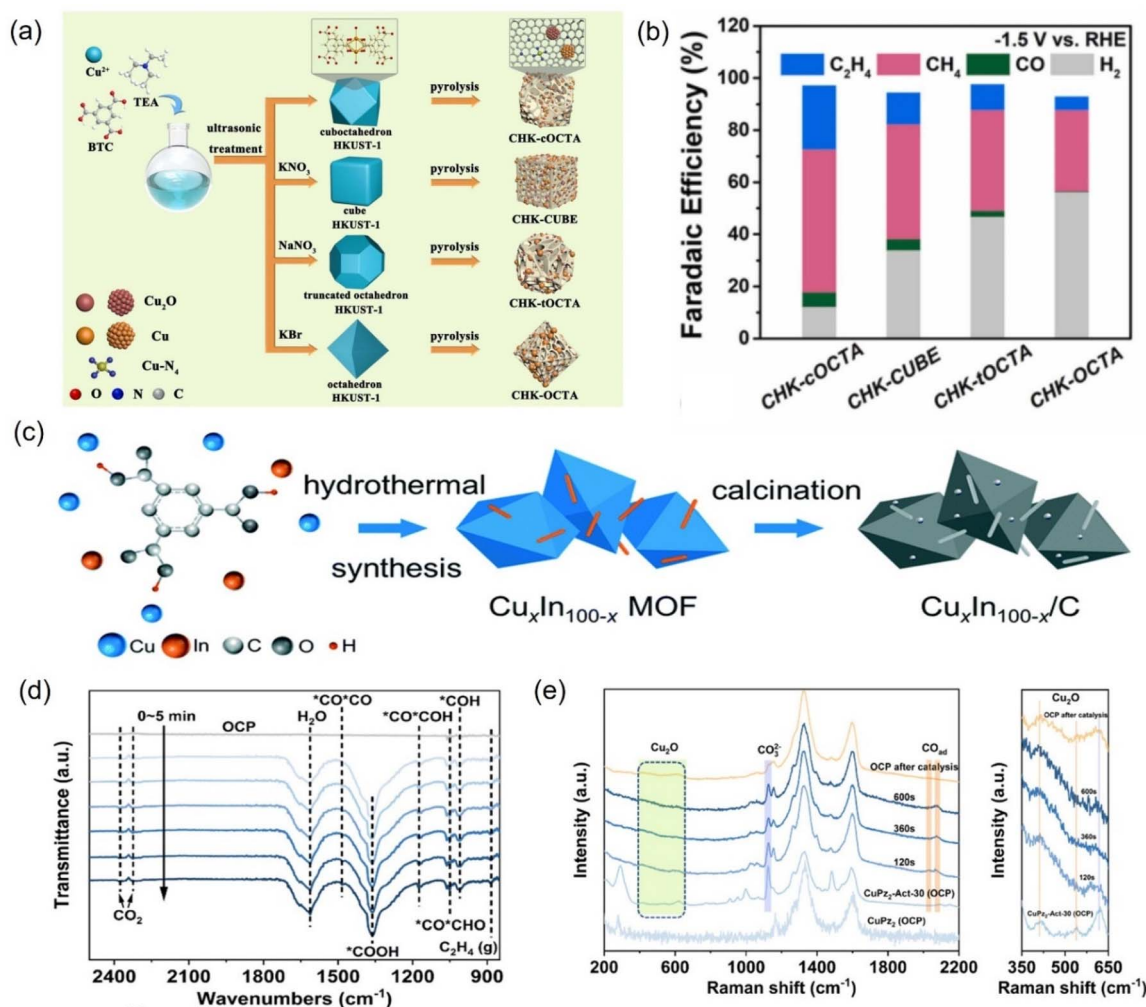


Fig. 23 (a) Illustration of the fabrication of different Cu-based nanoreactors and (b) faradaic efficiency at  $-1.5\text{ V vs. RHE}$ . (c) Synthetic diagram of Cu–In bimetallic catalysts. (d) *In situ* ATR-FTIR spectra of  $\text{CuPz}_2\text{-Act-30}$  collected at  $-1.03\text{ V vs. RHE}$  and (e) *in situ* Raman spectra of  $\text{CuPz}_2$  (OCP),  $\text{CuPz}_2\text{-Act-30}$  (OCP), and  $\text{CuPz}_2\text{-Act-30}$ . (a and b) Reproduced with permission.<sup>255</sup> Copyright 2022, Elsevier. (c) Reproduced with permission.<sup>257</sup> Copyright 2021, the Royal Society of Chemistry. (d and e) Reproduced with permission.<sup>258</sup> Copyright 2022, American Chemical Society.

the material is significantly reduced, HKUST-1 GDE exhibited excellent stability for continuous operation for 17 hours. On this basis, they introduced another metal Bi to synthesize bimetallic MOF materials and tested their ability to convert  $\text{CO}_2$  into alcoholic products.<sup>9</sup> Compared with single Cu/Bi-based MOFs, the synergistic effect between Cu and Bi optimizes the electronic structure of the active center and the energy barriers of the key reaction intermediates and promotes the formation of methanol and the C–C coupling step of ethanol. After a series of comparisons, it was found that the ratio of Cu and Bi loadings in the MOFs and the current density of the system significantly control the selectivity of the generated alcoholic products, which, above or below the optimal values of both, will weaken the catalytic performance of  $\text{ECO}_{2\text{RR}}$ .

**4.3.3. Other metal-based MOFs.** There are some reports on cobalt-, iron-, zirconium-, bismuth- and nickel-based MOFs-derived catalysts. A series of MOFs with different morphologies (abbreviated as Ni-MOF-525) with zirconia clusters as

nodes and nickel porphyrin complexes as bridging ligands were synthesized by Zheng *et al.*<sup>259</sup> Ni SACs in an H-cell possessed an urchin-like hierarchical structure with internal voids, with rapid and highly selective electroreduction of  $\text{CO}_2$  to CO ( $\text{FE}_{\text{CO}} = 98\%$ ) even at a current density as high as  $200\text{ mA cm}^{-2}$ . Fe-N-C catalyst derived from Fe-MOF was found to exhibit high Faraday efficiency (86.8%) for CO products at an overpotential of 496 mV and excellent long-term stability due to the good inheritance of the Fe-MOF precursor.<sup>260</sup> Recently, MOF thin films as electrocatalytically active units have been shown to be functional for electrochemical  $\text{CO}_2$  reduction.<sup>261</sup> Hupp *et al.* embedded copper nanoparticles into a zirconium-MOF film (NU-1000). The catalyst was obtained by installing  $\text{Cu(II)}$  clusters in NU-1000 films by a solvothermal deposition method, followed by the electrochemical reduction of  $\text{Cu(II)}$  to metallic copper, which exhibited good electrocatalytic activity.<sup>262</sup> Li *et al.* reported the synthesis of Bi SAs/NC catalysts using Bi-MOFs as the precursors, which exhibited high intrinsic  $\text{CO}_2$  reduction



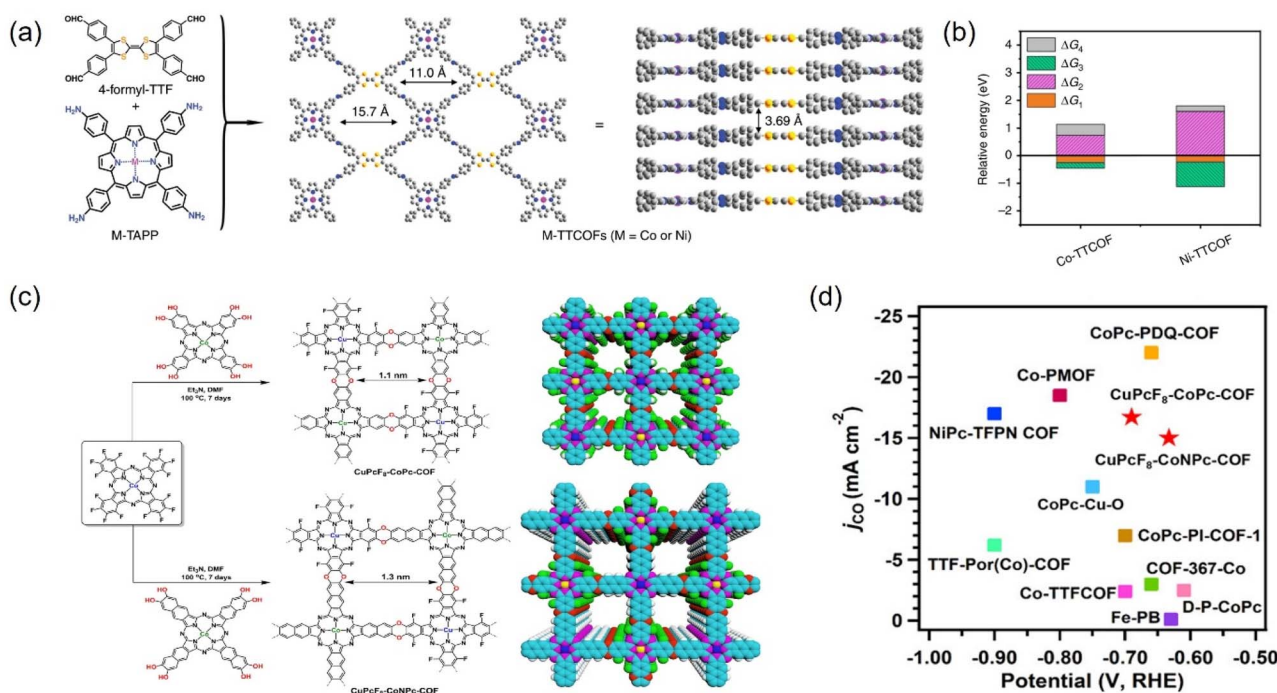


Fig. 24 (a) The structure of M-TTCOFs obtained through the condensation of 4-formyl-TTF and M-TAPP. (b) Comparison of the relative energy of each elementary reaction ( $\Delta G_1$ ,  $\Delta G_2$ , and  $\Delta G_3$  represent the free energy of  $^*CO_2$ ,  $^*COOH$ , and  $^*CO$  formation, respectively, and  $\Delta G_4$  stands for the free energy of CO desorption process) in the electrocatalytic CO<sub>2</sub>RR for M-TTCOFs (M = Co or Ni). (c) Schematic representation for the synthesis of CuPcF<sub>8</sub>-CoPc-COF and CuPcF<sub>8</sub>-CoNpc-CO. (d) Comparison of  $j_{CO}$ . (a and b) Reproduced with permission.<sup>265</sup> Copyright 2020, Springer Nature. (c and d) Reproduced with permission.<sup>266</sup> Copyright 2021, American Chemical Society.

activity for CO conversion, with a high FE<sub>CO</sub> of 97% and high turnover frequency of 5535 h<sup>-1</sup> at a low overpotential of 0.39 V.<sup>82</sup>

#### 4.4. Covalent organic frameworks

COFs are reticulated crystalline solids with a periodic structure consisting of molecular units connected by functional organic ligands.<sup>202,263,264</sup> COFs, as promising alternative materials for electrocatalytic CO<sub>2</sub>RR, are mainly attributed to more exposed surface area and active sites, tunable structure, and the possibility of modifying a wide range of metal types (*e.g.*, Co, Cu, and Ni) into their structure to confer the COFs with tunable catalytic centers.<sup>265</sup> These materials allow the integration of various organic building blocks into two-dimensional (2D) or three-dimensional (3D) mesh networks. Over the past decade, hundreds of COFs have been developed and used in a variety of applications, including gas adsorption, multiphase catalysis, photonics, photoemission, and wastewater treatment.<sup>266</sup>

**4.4.1. Two-dimensional COFs.** Two-dimensional (2D) COFs exhibit polymeric sheet-like structures composed of well-ordered polygons, endowing them with impressive stability for device application.<sup>267</sup> In CO<sub>2</sub>RR electrocatalysis, optimized 2D frameworks electrocatalysts would be an ideal choice to control the catalytic activity, selectivity and efficiency in a single catalytic system with high performance toward the target products.<sup>268</sup> Lan *et al.* prepared a series of stable and highly crystalline metalloporphyrin tetrathiafulvalene-based COFs (M-TTCOFs), in which Co-TTCOF was able to selectively convert CO<sub>2</sub> to CO, with an FE<sub>CO</sub> of 91.3% at -0.7 V. Moreover, DFT

calculations showed that Co-TTCOF displayed the lowest activation energy (Fig. 24a and b).<sup>265</sup> However, the poor electrical conductivity of monometallic COFs limits their electrocatalytic performance.<sup>269</sup> Huang *et al.* synthesized two novel ultra-stable bimetallic polyphthalocyanine-based 2D COFs, CuPcF<sub>8</sub>-CoPc-COF and CuPcF<sub>8</sub>-CoNpc-COF by rational design using dioxin as the bond.<sup>266</sup> The structure of the metal phthalocyanine units in overlapping stacking mode provides a high-speed pathway for electron transfer. Notably, the CuPcF<sub>8</sub>-CoNpc-COF possessed a Faraday efficiency of 97%, which is superior to most COF-based electrocatalysts (Fig. 24c and d). In addition, constructing interlayer hydrogen bonds in 2D COFs can enhance the interlayer interactions of COFs, thereby improving the electrical conductivity, thermal stability, and chemical stability.<sup>270</sup> Three new 2D polyimide-conjugated phthalocyanine COFs, namely, NiPc-OH-COF, NiPc-OMe-COF, and NiPc-H-COF, were synthesized by Jiang *et al.* Owing to the introduction of additional interlayer hydrogen-bonding interactions between the O-H of the 4-phenylene diols and the hydroxyl "O" atoms of the neighboring layers, the NiPc-OH-COFs showed enhanced chemical stability, which could be stabilized for 2 weeks even under a 1 M aqueous sodium hydroxide solution.<sup>271</sup>

**4.4.2. Three-dimensional COFs.** The active sites are usually hidden in the layers of 2D COF materials due to the face-to-face lamellar stacking that limits their proximity to the electrolyte and CO<sub>2</sub>, thus reducing the concentration of surface active sites in the electrocatalytic process.<sup>272</sup> 3D COFs could maximize active electrocatalytic sites by spatially separating molecular





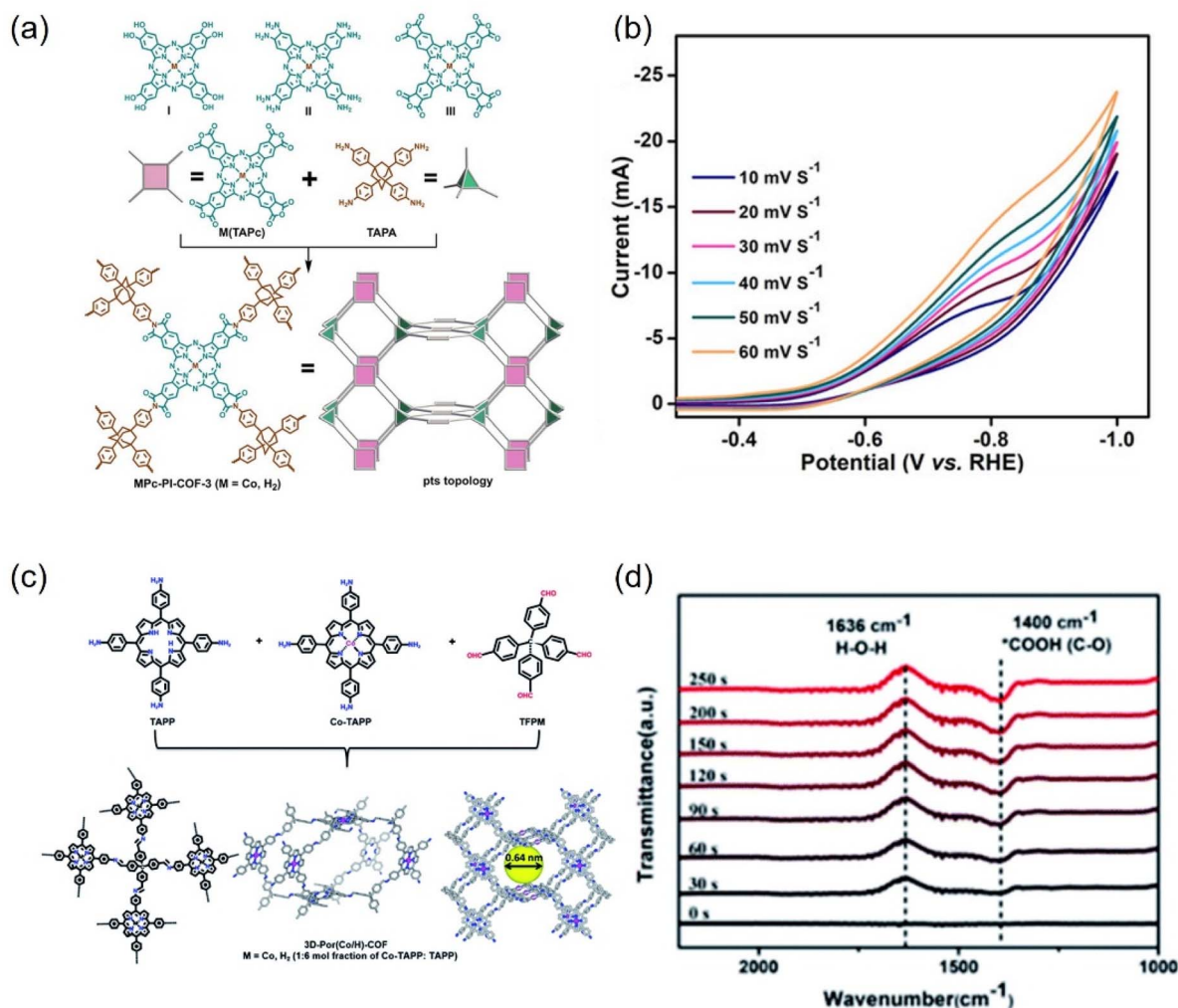


Fig. 25 (a) Synthesis of MPC-PI-COF-3 ( $M = \text{Co}^{\text{II}}$  or  $\text{H}_2$ ) and (b) scan rate dependence of cyclic voltammetry response of CoPc-PI-COF-3. (c) Schematic representation of the synthesis of 3D-Por(Co/H)-COF and the simulated network. (d) *In situ* ATR-IR of 3D-Por(Co/H)-COF at  $-0.9$  V. (a and b) Reproduced with permission.<sup>274</sup> Copyright 2022, John Wiley and Sons Ltd. (c and d) Reproduced with permission.<sup>275</sup> Copyright 2022, Royal Society of Chemistry.

building blocks.<sup>273</sup> Jiang *et al.* constructed 3D phthalocyanine (Pc) polyimide (PI) COFs (M-Pc-PI-COFs-3 ( $M = \text{Co}^{\text{II}}$ ,  $\text{H}_2$ )), in which the unique 3D porous structure of CoPc-PI-COF-3 ensured an electrochemical surface concentration of up to  $183 \text{ nmol cm}^{-2}$  at the electrode, *i.e.*, 32.7% of the metal phthalocyanine substituent as the active center (Fig. 25a and b).<sup>274</sup> Besides, a porous 3D cobalt porphyrinic COF, denoted as 3D-Por(Co/H)-COF, was synthesized by Cao and coworkers, which exhibited high activity for  $\text{CO}_2\text{RR}$  with a CO faradaic efficiency of 92.4% at  $-0.6$  V *versus* RHE.<sup>275</sup> ATR-IR spectra showed that the formation of the  $^*\text{COOH}$  intermediate was the rate-determining step for the  $\text{CO}_2\text{RR}$  (Fig. 25c and d).

## 5. Challenges and perspectives

Metal-based electrocatalysts have been widely studied for the  $\text{CO}_2\text{RR}$  due to their controllable composition and structure, excellent chemical stability and clear catalytically active sites. In

this review, we summarize the basic research and current research progress of catalyst structure regulation and carrier selection involved in  $\text{CO}_2\text{RR}$ . Although significant progress has been made in electrocatalytic  $\text{CO}_2\text{RR}$ , the actual related research is still in its infancy. As a promising way to close the carbon cycle and generate value-added products,  $\text{CO}_2\text{RR}$  is attracting more and more attention. However,  $\text{CO}_2\text{RR}$  is extremely sensitive to the reaction environment, which makes it difficult to accurately grasp the reaction process. Physical and chemical changes may occur during the catalytic process as well as morphological evolution such as surface recombination and roughening on the catalyst surface. In order to obtain efficient target products, there are still several crucial challenges to be overcome.

(1) Compared with the easily available  $\text{C}_1$  product, the reduction reactions of  $\text{C}_2$  and  $\text{C}_3$  products remain to be further studied. For two-electron products, high Faraday efficiency can be achieved at a given potential, but the overpotential is still



unsatisfactory compared with the theoretical value. Hence, improving the Faraday efficiency of multi-carbon products is the main direction of future research. Commercially, the reduction products are required to have high Faraday efficiency (>90%) and current density (>200 mA cm<sup>-2</sup>). Increasing the selectivity for high-value products remains a major challenge and there is still a huge room for progress.

It is necessary, on the one hand, to develop the catalytic activity and product possibilities of more metal elements, and, on the other hand, to improve the specific Faraday efficiency of metals known to produce multi-carbon products. Besides, most of the reported electrocatalysts are usually designed as powders, which may lead to the serious agglomeration of the material, thereby reducing the utilization of active sites. Furthermore, excessive pursuit of performance improvement while ignoring the cost considerations is also not conducive to practical application. Therefore, people are eager to minimize the use of expensive precursors and surfactants and simplify the synthesis processes to obtain catalytic systems with both low cost and high efficiency. On the basis of clarifying the active sites by experiments and theoretical calculations, the core of the solution needs to be considered from the perspective of the catalyst itself. Optimization strategies including heteroatom doping, defect engineering, and morphology design are useful for assisting electrocatalysts in achieving economical products with higher purity. Conceptualizing ingenious strategies is the golden key to meet the selectivity requirements in practical application. For example, as the material size is optimized for further reduction, the density of the active site along with the specific surface area will continue to expand, which can promote mass transport and improve the kinetic activity. Furthermore, the selective introduction of defects such as vacancies and grain boundaries can effectively contribute to the desired outcome. In addition, the hydrophilicity and hydrophobicity of the catalyst can be adjusted to optimize the binding energy of the intermediate, thus affecting the competitive relationship between CO<sub>2</sub>RR and HER.

(2) Compared with the success achieved in the catalytic activity of ECO<sub>2</sub>RR, the breakthrough in the stability has been more dismal. To date, almost all the reported materials have a lifetime of less than 1000 hours.<sup>14</sup> The peak achievement is that the operating time for CO and formic acid can reach 3800 and 2400 hours, respectively.<sup>276,277</sup> However, these existing catalysts are far from meeting the commercial threshold of more than 50 000 hours for the low-temperature operation of ECO<sub>2</sub>RR.<sup>278</sup> Therefore, on the road to the commercialization of ECO<sub>2</sub>RR, meeting the most troublesome difficulties of long-term stable operation is the core technical problem to be solved urgently. There are many factors that lead to the instability of electrocatalysis. For example, small perturbations in the electrochemical microenvironment may increase the difficulty of species mass transfer, thereby limiting the diffusion and adsorption of CO<sub>2</sub> molecules. In this regard, it is necessary to optimize the entire electrolysis system and alleviate flooding and carbonate problems. In addition, the active sites will undergo isomeric collapse as the ECO<sub>2</sub>RR continues, resulting in the inability of electrons to be quickly transferred, and the key intermediate species cannot be effectively adsorbed, which

has a devastating effect on both the stability and activity. The key to solving this thorny problem is to create more thermodynamic and kinetic barriers to atomic migration. Enhancing the bond strength of lattice atomic bonds to chemically improve the degree of bonding and wrapping casing materials to physically prevent atomic diffusion are effective strategies to avoid surface reconstruction, which can be achieved by ligand protection, doping/alloying, interface construction and protective layer encapsulation. Notably, the reasonable manipulation of operating conditions such as pulse electrolysis can also uniquely extend the durability of the material by repairing the active center and adjusting the interfacial chemistry. Specifically, pulse operation prolongs the ECO<sub>2</sub>RR process by inhibiting carbonate deposition, removing surface toxins/bubbles, and recovering active phases.

(3) In addition to the optimization of the catalyst itself, it is particularly critical to design a more suitable CO<sub>2</sub>RR electrolytic cell.<sup>279</sup> The setting of electrolytic cells will have a profound impact on the overall performance of ECO<sub>2</sub>RR.<sup>280</sup> With the improvement of this technical field, it is particularly critical to significantly reduce the overpotential of CO<sub>2</sub>RR in the electrolytic cell. Through the analysis and comparison of various types of electrolytic cells, in most of the current studies, the three reactors of H-type electrolytic cell,<sup>281</sup> flow type electrolytic cell<sup>282</sup> and membrane electrode electrolytic cell<sup>283</sup> are widely used. The H-type electrolytic cell is separated from the left and right chambers by an ion-exchange membrane.<sup>284</sup> The separation of electrolyte and cathode reaction gas can be achieved by exchange. However, the solubility of CO<sub>2</sub> in the environment containing water electrolyte is relatively low. Therefore, in the H-type reactor, the mass transfer process is greatly restricted. Due to the large interfacial tension between water and air, the gas cannot enter the cathode chamber through this area, thus affecting the electrolysis reaction. In addition, continuous carbon dioxide blowing may lead to an increase in the pH value of the electrolyte, which is more detrimental to the performance of the H-type battery. In order to solve the problems existing in the H-type electrolytic cell, researchers have designed a flow electrolytic cell for CO<sub>2</sub>RR. Compared with the H-type electrolytic cell, the flow cell adds a gas chamber, and the gas diffusion layer (GDL) is used to separate the cathode electrolyte and the CO<sub>2</sub> gas. The CO<sub>2</sub> gas can directly pass through the GDL and react on the surface of the catalyst. The flow cell also has the ability to utilize alkaline electrolytes, which is beneficial because it can inhibit HER in a high pH environment, thereby improving the performance of CO<sub>2</sub>RR. From the perspective of commercialization, membrane electrode electrolyzers are considered to be the most suitable equipment for commercial applications. However, some organic products may cause damage to solid electrolytes and ion-exchange membranes during long-term use, thereby reducing their durability. Therefore, for a variety of different products, we need to optimize and adjust the system of solid electrolyte electrolyzers in a timely manner. The careful design of electrodes and electrolytic reactors plays a vital role in achieving catalytic activity with industrial application value.

(4) DFT calculations can explore the electronic structure and directly identify the active sites at the atomic level. It is a favorable weapon for reasonably analyzing the reaction



mechanism and predicting the catalytic steps and has an indispensable inspiration and guidance for experimental preparation.<sup>285</sup> For ECO<sub>2</sub>RR, the intrinsic properties of CO<sub>2</sub> molecules are variable, the types of intermediates of CO<sub>2</sub>RR are multifarious, and the effects of solvation and ion on CO<sub>2</sub>RR at the solid–liquid interface are relatively complex. Theoretical calculations are increasingly being relied upon to reveal the mechanism of the tedious reaction steps and to screen for more optimized material compositions and structures. Due to the escalating difficulty, the theoretical insights of CO<sub>2</sub>RR are far less comprehensive and profound than other electrocatalytic reactions such as OER, HER, and ORR, and there is still a huge unknown space to be exploited. Typically, the calculation of the hydrogen electrode (CHE) is modeled under the assumption that the catalyst is charge-neutral to calculate the energy barrier of each intermediate step. However, ECO<sub>2</sub>RR usually occurs at the gas–liquid–solid interface with a constant electrode potential. The surface of the catalyst is charged and is balanced by electron exchange with the electrode, rather than without the electrode potential, which is a non-negligible influence factor in ECO<sub>2</sub>RR. For example, the basic step energy barrier of the proton–electron transfer of ECO<sub>2</sub>RR to CO on Cu (100) is profoundly affected by the electrode potential, and their change trend is opposite. In this regard, Wang *et al.* regulated the electrode potential of the system by introducing anions (Cl<sup>−</sup>) and cations (Na<sup>+</sup>) and detect their effects using constrained molecular dynamic (MD) sampling and thermodynamic integration.<sup>286</sup> They also elucidated the mechanism of electron transfer-proton transfer (ET-PT) decoupling and hydrogen bond-assisted CO<sub>2</sub> activation, indicating that the efficient adsorption and activation of CO<sub>2</sub> are closely related to the electron transfer of active sites, demonstrating that the electrode potential is the key to achieving efficient capture of CO<sub>2</sub>. In addition, the hydrogen bond network between the water solvent molecules interacts strongly with the key species adsorbed on the catalyst surface, and this solvent effect almost determines the stability of ECO<sub>2</sub>RR intermediates. In summary, it is of great significance to construct a clear model of aqueous solution system and introduce the consideration of electrode potential into the calculation simultaneously. In the future, the influencing factors included in the theoretical research on ECO<sub>2</sub>RR need to be more comprehensive to fit the actual reaction in the experiment as much as possible.

Looking ahead, ECO<sub>2</sub>RR research will mainly focus on the system design of the electrolyzer and the optimization and evaluation of electrochemical performance, especially in the design of the reactor, the nature of the electrode, electrolyte, ion exchange membrane, voltage, current density, energy efficiency and the service life of the electrolyzer. These research results will provide a strong impetus and guidance for the commercial application of ECO<sub>2</sub>RR.

## Author contributions

All of the authors contributed to the literature search, writing and editing of this review.

## Conflicts of interest

There are no conflicts to declare.

## Acknowledgements

This work was supported by the National Natural Science Foundation of China (No. 22075099), and the Natural Science Foundation of Jilin Province (No. 20220101051JC).

## Notes and references

- S. Gao, Y. Zhu, M. Umar, B. Kchouri and A. Safi, *Technol. Forecast. Soc.*, 2024, **201**, 123177.
- R. Huang, *Sci. Total Environ.*, 2024, **913**, 169775.
- J. Rogelj and R. D. Lamboll, *Commun. Earth Environ.*, 2024, **5**, 35.
- Z.-C. Zeng, T. Pongetti, S. Newman, T. Oda, K. Gurney, P. I. Palmer, Y. L. Yung and S. P. Sander, *Nat. Commun.*, 2023, **14**, 5353.
- M. Umar, S. Farid and M. A. Naeem, *Energy*, 2022, **240**, 122702.
- Y. Y. Birdja, E. Pérez-Gallent, M. C. Figueiredo, A. J. Göttle, F. Calle-Vallejo and M. T. M. Koper, *Nat. Energy*, 2019, **4**, 732–745.
- A. D. Handoko, F. Wei, Jenndy, B. S. Yeo and Z. W. Seh, *Nat. Catal.*, 2018, **1**, 922–934.
- D. Gao, R. M. Arán-Ais, H. S. Jeon and B. Roldan Cuenya, *Nat. Catal.*, 2019, **2**, 198–210.
- J. Albo, M. Perfecto-Irigaray, G. Beobide and A. Irabien, *J. CO<sub>2</sub> Util.*, 2019, **33**, 157–165.
- Z. Wang, Y. Zhou, P. Qiu, C. Xia, W. Fang, J. Jin, L. Huang, P. Deng, Y. Su, R. Crespo-Otero, X. Tian, B. You, W. Guo, D. Di Tommaso, Y. Pang, S. Ding and B. Y. Xia, *Adv. Mater.*, 2023, **35**, 2303052.
- Y. Zou and S. Wang, *Adv. Sci.*, 2021, **8**, 2003579.
- X. Zhang, Z. Zhang, H. Li, R. Gao, M. Xiao, J. Zhu, M. Feng and Z. Chen, *Adv. Energy Mater.*, 2022, **12**, 2201461.
- J. Albo, D. Vallejo, G. Beobide, O. Castillo, P. Castaño and A. Irabien, *ChemSusChem*, 2016, **10**, 1100–1109.
- W. Lai, Y. Qiao, Y. Wang and H. Huang, *Adv. Mater.*, 2023, **35**, 2306288.
- H. Wu, A. Singh-Morgan, K. Qi, Z. Zeng, V. Mougel and D. Voiry, *ACS Catal.*, 2023, **13**, 5375–5396.
- S. Kumar De, D.-I. Won, J. Kim and D. H. Kim, *Chem. Soc. Rev.*, 2023, **52**, 5744–5802.
- I. Merino-Garcia, J. Albo, J. Solla-Gullón, V. Montiel and A. Irabien, *J. CO<sub>2</sub> Util.*, 2019, **31**, 135–142.
- B. Kumar, M. Llorente, J. Froehlich, T. Dang, A. Sathrum and C. P. Kubiak, *Annu. Rev. Phys. Chem.*, 2012, **63**, 541–569.
- X. Chang, T. Wang and J. Gong, *Energy Environ. Sci.*, 2016, **9**, 2177–2196.
- I. Merino-Garcia, J. Albo and A. Irabien, *Nanotechnology*, 2018, **29**, 014001.
- L. Zhang, Z. J. Zhao and J. Gong, *Angew. Chem., Int. Ed.*, 2017, **56**, 11326–11353.





- 22 L. R. L. Ting and B. S. Yeo, *Curr. Opin. Electrochem.*, 2018, **8**, 126–134.
- 23 C. Shi, K. Chan, J. S. Yoo and J. K. Nørskov, *Org. Process Res. Dev.*, 2016, **20**, 1424–1430.
- 24 S. Back, M. S. Yeom and Y. Jung, *ACS Catal.*, 2015, **5**, 5089–5096.
- 25 A. Dutta, A. Kuzume, M. Rahaman, S. Vesztergom and P. Broekmann, *ACS Catal.*, 2015, **5**, 7498–7502.
- 26 W. Zhang, Y. Hu, L. Ma, G. Zhu, Y. Wang, X. Xue, R. Chen, S. Yang and Z. Jin, *Adv. Sci.*, 2017, **5**, 1700275.
- 27 G. Marcandalli, M. C. O. Monteiro, A. Goyal and M. T. M. Koper, *Acc. Chem. Res.*, 2022, **55**, 1900–1911.
- 28 J. Y. Yang, T. A. Kerr, X. S. Wang and J. M. Barlow, *J. Am. Chem. Soc.*, 2020, **142**, 19438–19445.
- 29 X. Zhou, J. Shan, L. Chen, B. Y. Xia, T. Ling, J. Duan, Y. Jiao, Y. Zheng and S.-Z. Qiao, *J. Am. Chem. Soc.*, 2022, **144**, 2079–2084.
- 30 L. Deng, Z. Wang, X. Jiang, J. Xu, Z. Zhou, X. Li, Z. You, M. Ding, T. Shishido, X. Liu and M. Xu, *Appl. Catal., B*, 2023, **322**, 122124.
- 31 H. Yang, Y. Wu, G. Li, Q. Lin, Q. Hu, Q. Zhang, J. Liu and C. He, *J. Am. Chem. Soc.*, 2019, **141**, 12717–12723.
- 32 R. Kortlever, J. Shen, K. J. P. Schouten, F. Calle-Vallejo and M. T. M. Koper, *J. Phys. Chem. Lett.*, 2015, **6**, 4073–4082.
- 33 M. F. Baruch, J. E. Pander, J. L. White and A. B. Bocarsly, *ACS Catal.*, 2015, **5**, 3148–3156.
- 34 X. Min and M. W. Kanan, *J. Am. Chem. Soc.*, 2015, **137**, 4701–4708.
- 35 H. A. Hansen, J. B. Varley, A. A. Peterson and J. K. Nørskov, *J. Phys. Chem. Lett.*, 2013, **4**, 388–392.
- 36 C. Chen, J. F. Khosrowabadi Kotyk and S. W. Sheehan, *Chem*, 2018, **4**, 2571–2586.
- 37 L. Wang, W. Chen, D. Zhang, Y. Du, R. Amal, S. Qiao, J. Wu and Z. Yin, *Chem. Soc. Rev.*, 2019, **48**, 5310–5349.
- 38 A. A. Peterson, F. Abild-Pedersen, F. Studt, J. Rossmeisl and J. K. Nørskov, *Energy Environ. Sci.*, 2010, **3**, 1311–1315.
- 39 Y. Lin, T. Wang, L. Zhang, G. Zhang, L. Li, Q. Chang, Z. Pang, H. Gao, K. Huang, P. Zhang, Z.-J. Zhao, C. Pei and J. Gong, *Nat. Commun.*, 2023, **14**, 3575.
- 40 C.-T. Dinh, T. Burdyny, Md G. Kibria, S. Ali, C. M. Gabardo, F. Pelayo García de Arquer, A. Kiani, J. P. Edwards, P. De Luna, O. S. Bushuyev, C. Zou, R. Quintero-Bermudez, Y. Pang, D. Sinton and E. H. Sargent, *Science*, 2018, **360**, 783–787.
- 41 X. Nie, M. R. Esopi, M. J. Janik and A. Asthagiri, *Angew. Chem., Int. Ed.*, 2013, **52**, 2459–2462.
- 42 K. D. Yang, C. W. Lee, K. Jin, S. W. Im and K. T. Nam, *J. Phys. Chem. Lett.*, 2017, **8**, 538–545.
- 43 E. Pérez-Gallent, M. C. Figueiredo, F. Calle-Vallejo and M. T. M. Koper, *Angew. Chem., Int. Ed.*, 2017, **56**, 3621–3624.
- 44 Y. Hori, R. Takahashi, Y. Yoshinami and A. Murata, *J. Phys. Chem. B*, 1997, **101**, 7075–7081.
- 45 Z. Sun, T. Ma, H. Tao, Q. Fan and B. Han, *Chem*, 2017, **3**, 560–587.
- 46 X. Li, M. Qin, X. Wu, X. Lv, J. Wang, Y. Wang and H. B. Wu, *Small*, 2023, **19**, 2302530.
- 47 J. Zhang, Y. Wang, Z. Li, S. Xia, R. Cai, L. Ma, T. Zhang, J. Ackley, S. Yang, Y. Wu and J. Wu, *Adv. Sci.*, 2022, **9**, 2200454.
- 48 T. T. H. Hoang, S. Verma, S. Ma, T. T. Fister, J. Timoshenko, A. I. Frenkel, P. J. A. Kenis and A. A. Gewirth, *J. Am. Chem. Soc.*, 2018, **140**, 5791–5797.
- 49 P. Wang, H. Yang, C. Tang, Y. Wu, Y. Zheng, T. Cheng, K. Davey, X. Huang and S.-Z. Qiao, *Nat. Commun.*, 2022, **13**, 3754.
- 50 C. Peng, X. Zhu, Z. Xu, S. Yan, L. Y. Chang, Z. Wang, J. Zhang, M. Chen, T. K. Sham, Y. Li and G. Zheng, *Small*, 2021, **18**, 2106433.
- 51 C. Peng, G. Luo, Z. Xu, S. Yan, J. Zhang, M. Chen, L. Qian, W. Wei, Q. Han and G. Zheng, *Adv. Mater.*, 2021, **33**, 2103150.
- 52 D. Zhong, Z. J. Zhao, Q. Zhao, D. Cheng, B. Liu, G. Zhang, W. Deng, H. Dong, L. Zhang, J. Li, J. Li and J. Gong, *Angew. Chem., Int. Ed.*, 2021, **60**, 4879–4885.
- 53 H. Li, T. Liu, P. Wei, L. Lin, D. Gao, G. Wang and X. Bao, *Angew. Chem., Int. Ed.*, 2021, **60**, 14329–14333.
- 54 J. J. Lv, M. Jouny, W. Luc, W. Zhu, J. J. Zhu and F. Jiao, *Adv. Mater.*, 2018, **30**, 1803111.
- 55 P. Wang, H. Yang, Y. Xu, X. Huang, J. Wang, M. Zhong, T. Cheng and Q. Shao, *ACS Nano*, 2020, **15**, 1039–1047.
- 56 X. Wang, K. Klingan, M. Klingenhof, T. Möller, J. Ferreira de Araújo, I. Martens, A. Bagger, S. Jiang, J. Rossmeisl, H. Dau and P. Strasser, *Nat. Commun.*, 2021, **12**, 794.
- 57 Q. Zhu, Y. Hu, H. Chen, C. Meng, Y. Shang, C. Hao, S. Wei, Z. Wang, X. Lu and S. Liu, *Nanoscale*, 2023, **15**, 2106–2113.
- 58 J. Wu, S. Ma, J. Sun, J. I. Gold, C. Tiwary, B. Kim, L. Zhu, N. Chopra, I. N. Odeh, R. Vajtai, A. Z. Yu, R. Luo, J. Lou, G. Ding, P. J. A. Kenis and P. M. Ajayan, *Nat. Commun.*, 2016, **7**, 13869.
- 59 J. Yuan, W.-Y. Zhi, L. Liu, M.-P. Yang, H. Wang and J.-X. Lu, *Electrochim. Acta*, 2018, **282**, 694–701.
- 60 X. Zou, M. Liu, J. Wu, P. M. Ajayan, J. Li, B. Liu and B. I. Yakobson, *ACS Catal.*, 2017, **7**, 6245–6250.
- 61 C. Liang, B. Kim, S. Yang, Y. L. Yang Liu, C. Francisco Woellner, Z. Li, R. Vajtai, W. Yang, J. Wu, P. J. A. Kenis and P. M. Ajayan, *J. Mater. Chem. A*, 2018, **6**, 10313–10319.
- 62 M. Yu, P. F. Sui, X. Z. Fu, J. L. Luo and S. Liu, *Adv. Energy Mater.*, 2022, **13**, 2203191.
- 63 L. Xiao, X. Bai, J. Han, T. Tang, S. Chen, H. Qi, C. Hou, F. Bai, Z. Wang and J. Guan, *Nano Res.*, 2023, **17**, 2429–2437.
- 64 L. Xiao, L. Qi, J. Sun, A. Husile, S. Zhang, Z. Wang and J. Guan, *Nano Energy*, 2024, **120**, 109155.
- 65 S. Chen, T. Zhang, J. Han, H. Qi, S. Jiao, C. Hou and J. Guan, *Nano Res. Energy*, 2024, **3**, e9120106.
- 66 Y. Huang, F. Rehman, M. Tamtaji, X. Li, Y. Huang, T. Zhang and Z. Luo, *J. Mater. Chem. A*, 2022, **10**, 5813–5834.
- 67 T. Tang, Z. Wang and J. Guan, *Acta Phys.-Chim. Sin.*, 2022, 2208033.
- 68 T. Tang, Z. Wang and J. Guan, *Adv. Funct. Mater.*, 2022, **32**, 2111504.
- 69 X. Bai, Y. Wang, J. Han, X. Niu and J. Guan, *Appl. Catal., B*, 2023, **337**, 122966.



- 70 T. Tang, Z. Wang and J. Guan, *Coord. Chem. Rev.*, 2023, **492**, 215288.
- 71 J. Han and J. Guan, *Nano Res.*, 2023, **16**, 1913–1966.
- 72 T. Zhang, J. Sun and J. Guan, *Nano Res.*, 2023, **16**, 8684–8711.
- 73 L. Li, X. Li, Y. Sun and Y. Xie, *Chem. Soc. Rev.*, 2022, **51**, 1234–1252.
- 74 D. Gao, W. Li, H. Wang, G. Wang and R. Cai, *Trans. Tianjin Univ.*, 2022, **28**, 245–264.
- 75 H. Yao, M.-Y. Wang, C. Yue, B. Feng, W. Ji, C. Qian, S. Wang, S. Zhang and X. Ma, *Trans. Tianjin Univ.*, 2023, **29**, 254–274.
- 76 T. Tang, J. Han, Z. Wang, X. Niu and J. Guan, *Nano Res.*, 2023, **17**, 3794–3800.
- 77 J. Zhang, W. Cai, F. X. Hu, H. Yang and B. Liu, *Chem. Sci.*, 2021, **12**, 6800–6819.
- 78 J. Ma, C. Liu, M. Bai, Z. Fu, P. Zhao, Y. Gao, M. Zhao, Y. He, H. Xiao and J. Jia, *Mol. Catal.*, 2023, **551**, 113632.
- 79 M. Li, H. Wang, W. Luo, P. C. Sherrell, J. Chen and J. Yang, *Adv. Mater.*, 2020, **32**, 2001848.
- 80 W. Zheng, F. Chen, Q. Zeng, Z. Li, B. Yang, L. Lei, Q. Zhang, F. He, X. Wu and Y. Hou, *Nano-Micro Lett.*, 2020, **12**, 108.
- 81 G. Qu, K. Wei, K. Pan, J. Qin, J. Lv, J. Li and P. Ning, *Nanoscale*, 2023, **15**, 3666–3692.
- 82 E. Zhang, T. Wang, K. Yu, J. Liu, W. Chen, A. Li, H. Rong, R. Lin, S. Ji, X. Zheng, Y. Wang, L. Zheng, C. Chen, D. Wang, J. Zhang and Y. Li, *J. Am. Chem. Soc.*, 2019, **141**, 16569–16573.
- 83 W. Guo, X. Tan, J. Bi, L. Xu, D. Yang, C. Chen, Q. Zhu, J. Ma, A. Tayal, J. Ma, Y. Huang, X. Sun, S. Liu and B. Han, *J. Am. Chem. Soc.*, 2021, **143**, 6877–6885.
- 84 Z. Jiang, T. Wang, J. Pei, H. Shang, D. Zhou, H. Li, J. Dong, Y. Wang, R. Cao, Z. Zhuang, W. Chen, D. Wang, J. Zhang and Y. Li, *Energy Environ. Sci.*, 2020, **13**, 2856–2863.
- 85 H. Xie, T. Wang, J. Liang, Q. Li and S. Sun, *Nano Today*, 2018, **21**, 41–54.
- 86 D. Gao, T. Liu, G. Wang and X. Bao, *ACS Energy Lett.*, 2021, **6**, 713–727.
- 87 Y. Jiang, Y. Wang, R. Chen, Y. Li and C. Li, *Energy Fuels*, 2023, **37**, 17951–17965.
- 88 A. Vasileff, C. Xu, Y. Jiao, Y. Zheng and S.-Z. Qiao, *Chem*, 2018, **4**, 1809–1831.
- 89 W. Ren, X. Tan, W. Yang, C. Jia, S. Xu, K. Wang, S. C. Smith and C. Zhao, *Angew. Chem., Int. Ed.*, 2019, **58**, 6972–6976.
- 90 W. Zhu, L. Zhang, S. Liu, A. Li, X. Yuan, C. Hu, G. Zhang, W. Deng, K. Zang, J. Luo, Y. Zhu, M. Gu, Z. J. Zhao and J. Gong, *Angew. Chem., Int. Ed.*, 2020, **59**, 12664–12668.
- 91 C. Jia, K. Dastafkan and C. Zhao, *Curr. Opin. Electrochem.*, 2022, **31**, 100854.
- 92 Z. Wu, Y. Zhao, W. Jin, B. Jia, J. Wang and T. Ma, *Adv. Funct. Mater.*, 2020, **31**, 2009070.
- 93 Y. Li, M. Wen, Y. Wang, G. Tian, C. Wang and J. Zhao, *Angew. Chem., Int. Ed.*, 2020, **60**, 910–916.
- 94 Z. Niu, X. Gao, S. Lou, N. Wen, J. Zhao, Z. Zhang, Z. Ding, R. Yuan, W. Dai and J. Long, *ACS Catal.*, 2023, **13**, 2998–3006.
- 95 Z. Li, A. Cao, Q. Zheng, Y. Fu, T. Wang, K. T. Arul, J. L. Chen, B. Yang, N. M. Adli, L. Lei, C. L. Dong, J. Xiao, G. Wu and Y. Hou, *Adv. Mater.*, 2020, **33**, 2005113.
- 96 H. Wang, N. Wen, Y. Wang, X. Jiao, Y. Xia and D. Chen, *Adv. Funct. Mater.*, 2023, **33**, 2303473.
- 97 B. Jia, L. Li, C. Xue, J. Kang, L. M. Liu, T. Guo, Z. Wang, Q. Huang and S. Guo, *Adv. Mater.*, 2023, **35**, 2305587.
- 98 Y. He, H. Rao, K. Song, J. Li, Y. Yu, Y. Lou, C. Li, Y. Han, Z. Shi and S. Feng, *Adv. Funct. Mater.*, 2019, **29**, 1905153.
- 99 X. Rong, H. J. Wang, X. L. Lu, R. Si and T. B. Lu, *Angew. Chem., Int. Ed.*, 2019, **59**, 1961–1965.
- 100 R. Chen, X. Zu, J. Zhu, Y. Zhao, Y. Li, Z. Hu, S. Wang, M. Fan, S. Zhu, H. Zhang, B. Ye, Y. Sun and Y. Xie, *Adv. Mater.*, 2024, 2314209, DOI: [10.1002/adma.202314209](https://doi.org/10.1002/adma.202314209).
- 101 W. Ding, S. Yuan, Y. Yang, X. Li and M. Luo, *J. Mater. Chem. A*, 2023, **11**, 23653–23682.
- 102 H. Yu, F. Chen, X. Li, H. Huang, Q. Zhang, S. Su, K. Wang, E. Mao, B. Mei, G. Mul, T. Ma and Y. Zhang, *Nat. Commun.*, 2021, **12**, 4594.
- 103 Y. Liang, C. Wu, S. Meng, Z. Lu, R. Zhao, H. Wang, Z. Liu and J. Wang, *ACS Appl. Mater. Interfaces*, 2023, **15**, 30262–30271.
- 104 S. Gao, Z. Sun, W. Liu, X. Jiao, X. Zu, Q. Hu, Y. Sun, T. Yao, W. Zhang, S. Wei and Y. Xie, *Nat. Commun.*, 2017, **8**, 14503.
- 105 Z. Geng, X. Kong, W. Chen, H. Su, Y. Liu, F. Cai, G. Wang and J. Zeng, *Angew. Chem., Int. Ed.*, 2018, **57**, 6054–6059.
- 106 B. Qin, Y. Li, H. Wang, G. Yang, Y. Cao, H. Yu, Q. Zhang, H. Liang and F. Peng, *Nano Energy*, 2019, **60**, 43–51.
- 107 L. Cheng, Y. Li, A. Chen, Y. Zhu and C. Li, *Chem. Commun.*, 2020, **56**, 563–566.
- 108 D. Yan, C. Xia, W. Zhang, Q. Hu, C. He, B. Y. Xia and S. Wang, *Adv. Energy Mater.*, 2022, **12**, 2202317.
- 109 D. Qu, X. Peng, Y. Mi, H. Bao, S. Zhao, X. Liu and J. Luo, *Nanoscale*, 2020, **12**, 17191–17195.
- 110 H. Liang, A. N. Gandi, D. H. Anjum, X. Wang, U. Schwingenschlögl and H. N. Alshareef, *Nano Lett.*, 2016, **16**, 7718–7725.
- 111 S. Dou, L. Tao, R. Wang, S. El Hankari, R. Chen and S. Wang, *Adv. Mater.*, 2018, **30**, 1705850.
- 112 S. Dou, L. Tao, J. Huo, S. Wang and L. Dai, *Energy Environ. Sci.*, 2016, **9**, 1320–1326.
- 113 C. Kong, F. Zhang, Y. Wang and J. Huang, *J. Alloys Compd.*, 2021, **876**, 160165.
- 114 H. Bi, S. Zhu, Y. Liang, H. Jiang, Z. Li, S. Wu, H. Wei, C. Chang and Z. Cui, *Chem. Eng. J.*, 2022, **442**, 136146.
- 115 J. Zhang, Y. Zhao, X. Guo, C. Chen, C.-L. Dong, R.-S. Liu, C.-P. Han, Y. Li, Y. Gogotsi and G. Wang, *Nat. Catal.*, 2018, **1**, 985–992.
- 116 F. Wang, W. Zhang, H. Wan, C. Li, W. An, X. Sheng, X. Liang, X. Wang, Y. Ren, X. Zheng, D. Lv and Y. Qin, *Chin. Chem. Lett.*, 2022, **33**, 2259–2269.
- 117 S. S. A. Shah, M. Sufyan Javed, T. Najam, C. Molochas, N. A. Khan, M. A. Nazir, M. Xu, P. Tsiakaras and S.-J. Bao, *Coord. Chem. Rev.*, 2022, **471**, 214716.
- 118 Y.-H. Luo, L.-Z. Dong, J. Liu, S.-L. Li and Y.-Q. Lan, *Coord. Chem. Rev.*, 2019, **390**, 86–126.



- 119 R. Reske, M. Duca, M. Oezaslan, K. J. P. Schouten, M. T. M. Koper and P. Strasser, *J. Phys. Chem. Lett.*, 2013, **4**, 2410–2413.
- 120 Z. Chang, S. Huo, W. Zhang, J. Fang and H. Wang, *J. Phys. Chem. C*, 2017, **121**, 11368–11379.
- 121 H. Xie, S. Chen, F. Ma, J. Liang, Z. Miao, T. Wang, H.-L. Wang, Y. Huang and Q. Li, *ACS Appl. Mater. Interfaces*, 2018, **10**, 36996–37004.
- 122 Q. Li, J. Fu, W. Zhu, Z. Chen, B. Shen, L. Wu, Z. Xi, T. Wang, G. Lu, J.-j. Zhu and S. Sun, *J. Am. Chem. Soc.*, 2017, **139**, 4290–4293.
- 123 J. Hao, S. Xie, Q. Huang, Z. Ding, H. Sheng, C. Zhang and J. Yao, *CCS Chem.*, 2023, **5**, 2046–2058.
- 124 M. He, W. An, Y. Wang, Y. Men and S. Liu, *Small*, 2021, **17**, 2104445.
- 125 Y. Xie, N. Liu, X. Li, X. Qin, X. Luo, Y. Wang and X. Chen, *J. Phys. Chem. C*, 2021, **125**, 21460–21470.
- 126 Z. Wang, R. Shi, S. Lu, K. Zhang and T. Zhang, *Rep. Prog. Phys.*, 2022, **85**, 026501.
- 127 Z. L. Wang, J. Choi, M. Xu, X. Hao, H. Zhang, Z. Jiang, M. Zuo, J. Kim, W. Zhou, X. Meng, Q. Yu, Z. Sun, S. Wei, J. Ye, G. G. Wallace, D. L. Officer and Y. Yamauchi, *ChemSusChem*, 2020, **13**, 929–937.
- 128 X. Zhao and Y. Liu, *J. Am. Chem. Soc.*, 2020, **142**, 5773–5777.
- 129 Q. Qu, S. Ji, Y. Chen, D. Wang and Y. Li, *Chem. Sci.*, 2021, **12**, 4201–4215.
- 130 Md Delowar Hossain, Y. Huang, T. H. Yu, W. A. Goddard and Z. Luo, *Nat. Commun.*, 2020, **11**, 2256.
- 131 Y. Pan, R. Lin, Y. Chen, S. Liu, W. Zhu, X. Cao, W. Chen, K. Wu, W.-C. Cheong, Y. Wang, L. Zheng, J. Luo, Y. Lin, Y. Liu, C. Liu, J. Li, Q. Lu, X. Chen, D. Wang, Q. Peng, C. Chen and Y. Li, *J. Am. Chem. Soc.*, 2018, **140**, 4218–4221.
- 132 H. Zhang, J. Li, S. Xi, Y. Du, X. Hai, J. Wang, H. Xu, G. Wu, J. Zhang, J. Lu and J. Wang, *Angew. Chem., Int. Ed.*, 2019, **58**, 14871–14876.
- 133 C. Yan, H. Li, Y. Ye, H. Wu, F. Cai, R. Si, J. Xiao, S. Miao, S. Xie, F. Yang, Y. Li, G. Wang and X. Bao, *Energy Environ. Sci.*, 2018, **11**, 1204–1210.
- 134 X. Wang, Z. Chen, X. Zhao, T. Yao, W. Chen, R. You, C. Zhao, G. Wu, J. Wang, W. Huang, J. Yang, X. Hong, S. Wei, Y. Wu and Y. Li, *Angew. Chem., Int. Ed.*, 2018, **57**, 1944–1948.
- 135 W. Zheng, J. Yang, H. Chen, Y. Hou, Q. Wang, M. Gu, F. He, Y. Xia, Z. Xia, Z. Li, B. Yang, L. Lei, C. Yuan, Q. He, M. Qiu and X. Feng, *Adv. Funct. Mater.*, 2019, **30**, 1907658.
- 136 J. Yang, Z. Qiu, C. Zhao, W. Wei, W. Chen, Z. Li, Y. Qu, J. Dong, J. Luo, Z. Li and Y. Wu, *Angew. Chem., Int. Ed.*, 2018, **57**, 14095–14100.
- 137 J. Feng, H. Gao, L. Zheng, Z. Chen, S. Zeng, C. Jiang, H. Dong, L. Liu, S. Zhang and X. Zhang, *Nat. Commun.*, 2020, **11**, 4341.
- 138 E. Jung, H. Shin, B.-H. Lee, V. Efremov, S. Lee, H. S. Lee, J. Kim, W. Hooch Antink, S. Park, K.-S. Lee, S.-P. Cho, J. S. Yoo, Y.-E. Sung and T. Hyeon, *Nat. Mater.*, 2020, **19**, 436–442.
- 139 Y. Cai, J. Fu, Y. Zhou, Y.-C. Chang, Q. Min, J.-J. Zhu, Y. Lin and W. Zhu, *Nat. Commun.*, 2021, **12**, 586.
- 140 H. Kim, D. Shin, W. Yang, D. H. Won, H.-S. Oh, M. W. Chung, D. Jeong, S. H. Kim, K. H. Chae, J. Y. Ryu, J. Lee, S. J. Cho, J. Seo, H. Kim and C. H. Choi, *J. Am. Chem. Soc.*, 2021, **143**, 925–933.
- 141 S. Cao, S. Wei, X. Wei, S. Zhou, H. Chen, Y. Hu, Z. Wang, S. Liu, W. Guo and X. Lu, *Small*, 2021, **17**, 2100949.
- 142 Y. Chen, R. Gao, S. Ji, H. Li, K. Tang, P. Jiang, H. Hu, Z. Zhang, H. Hao, Q. Qu, X. Liang, W. Chen, J. Dong, D. Wang and Y. Li, *Angew. Chem., Int. Ed.*, 2020, **60**, 3212–3221.
- 143 Y. Wu, C. Chen, X. Yan, X. Sun, Q. Zhu, P. Li, Y. Li, S. Liu, J. Ma, Y. Huang and B. Han, *Angew. Chem., Int. Ed.*, 2021, **60**, 20803–20810.
- 144 J. Wang, X. Huang, S. Xi, H. Xu and X. Wang, *Angew. Chem., Int. Ed.*, 2020, **59**, 19162–19167.
- 145 X. Wang, Y. Pan, H. Ning, H. Wang, D. Guo, W. Wang, Z. Yang, Q. Zhao, B. Zhang, L. Zheng, J. Zhang and M. Wu, *Appl. Catal., B*, 2020, **266**, 118630.
- 146 K. K. Patra, S. Park, H. Song, B. Kim, W. Kim and J. Oh, *ACS Appl. Energy Mater.*, 2020, **3**, 11343–11349.
- 147 Y. Zhou, F. Che, M. Liu, C. Zou, Z. Liang, P. De Luna, H. Yuan, J. Li, Z. Wang, H. Xie, H. Li, P. Chen, E. Bladt, R. Quintero-Bermudez, T.-K. Sham, S. Bals, J. Hofkens, D. Sinton, G. Chen and E. H. Sargent, *Nat. Chem.*, 2018, **10**, 974–980.
- 148 J. Gui, L. Li, B. Yu, D. Wang, B. Yang, Q. Gu, Y. Zhao, Y. Zhu and Y. Zhang, *ACS Appl. Mater. Interfaces*, 2023, **15**, 25516–25523.
- 149 W. Rong, H. Zou, W. Zang, S. Xi, S. Wei, B. Long, J. Hu, Y. Ji and L. Duan, *Angew. Chem., Int. Ed.*, 2021, **60**, 466–472.
- 150 A. Guan, Z. Chen, Y. Quan, C. Peng, Z. Wang, T.-K. Sham, C. Yang, Y. Ji, L. Qian, X. Xu and G. Zheng, *ACS Energy Lett.*, 2020, **5**, 1044–1053.
- 151 J. Dong, Y. Liu, J. Pei, H. Li, S. Ji, L. Shi, Y. Zhang, C. Li, C. Tang, J. Liao, S. Xu, H. Zhang, Q. Li and S. Zhao, *Nat. Commun.*, 2023, **14**, 6849.
- 152 Z.-Q. Liang, T.-T. Zhuang, A. Seifitokaldani, J. Li, C.-W. Huang, C.-S. Tan, Y. Li, P. De Luna, C. T. Dinh, Y. Hu, Q. Xiao, P.-L. Hsieh, Y. Wang, F. Li, R. Quintero-Bermudez, Y. Zhou, P. Chen, Y. Pang, S.-C. Lo, L.-J. Chen, H. Tan, Z. Xu, S. Zhao, D. Sinton and E. H. Sargent, *Nat. Commun.*, 2018, **9**, 3828.
- 153 C. Peng, G. Luo, Z. Xu, S. Yan, J. Zhang, M. Chen, L. Qian, W. Wei, Q. Han and G. Zheng, *Adv. Mater.*, 2021, **33**, 2103150.
- 154 C. A. Downes, N. J. Libretto, A. E. Harman-Ware, R. M. Happs, D. A. Ruddy, F. G. Baddour, J. R. Ferrell III, S. E. Habas and J. A. Schaidle, *ACS Appl. Energy Mater.*, 2020, **3**, 10435–10446.
- 155 H. Chen, Z. Wang, X. Wei, S. Liu, P. Guo, P. Han, H. Wang, J. Zhang, X. Lu and B. Wei, *Appl. Surf. Sci.*, 2021, **544**, 148965.
- 156 X. Kong, C. Wang, H. Zheng, Z. Geng, J. Bao and J. Zeng, *Sci. China: Chem.*, 2021, **64**, 1096–1102.
- 157 Y. Lum and J. W. Ager, *Angew. Chem., Int. Ed.*, 2018, **57**, 551–554.





- 158 A. M. Asiri, J. Gao, S. B. Khan, K. A. Alamry, H. M. Marwani, M. S. J. Khan, W. A. Adeosun, S. M. Zakeeruddin, D. Ren and M. Grätzel, *J. Phys. Chem. Lett.*, 2022, **13**, 345–351.
- 159 C. Peng, G. Luo, J. Zhang, M. Chen, Z. Wang, T.-K. Sham, L. Zhang, Y. Li and G. Zheng, *Nat. Commun.*, 2021, **12**, 1580.
- 160 T.-T. Zhuang, Z.-Q. Liang, A. Seifitokaldani, Y. Li, P. De Luna, T. Burdyny, F. Che, F. Meng, Y. Min, R. Quintero-Bermudez, C. T. Dinh, Y. Pang, M. Zhong, B. Zhang, J. Li, P.-N. Chen, X.-L. Zheng, H. Liang, W.-N. Ge, B.-J. Ye, D. Sinton, S.-H. Yu and E. H. Sargent, *Nat. Catal.*, 2018, **1**, 421–428.
- 161 S. Li, H. Duan, J. Yu, C. Qiu, R. Yu, Y. Chen, Y. Fang, X. Cai and S. Yang, *ACS Catal.*, 2022, **12**, 9074–9082.
- 162 J. Liu, P. Li, J. Bi, Y. Wang, Q. Zhu, X. Sun, J. Zhang, Z. Liu and B. Han, *Chin. J. Chem.*, 2023, **41**, 1443–1449.
- 163 X. Su, Z. Jiang, J. Zhou, H. Liu, D. Zhou, H. Shang, X. Ni, Z. Peng, F. Yang, W. Chen, Z. Qi, D. Wang and Y. Wang, *Nat. Commun.*, 2022, **13**, 1322.
- 164 D. Karapinar, N. T. Huan, N. Ranjbar Sahraie, J. Li, D. Wakerley, N. Touati, S. Zanna, D. Taverna, L. H. Galvão Tizei, A. Zitolo, F. Jaouen, V. Mougél and M. Fontecave, *Angew. Chem., Int. Ed.*, 2019, **58**, 15098–15103.
- 165 H. Wang, X. Bi, Y. Yan, Y. Zhao, Z. Yang, H. Ning and M. Wu, *Adv. Funct. Mater.*, 2023, **33**, 2214946.
- 166 D. Yang, Q. Zhu, C. Chen, H. Liu, Z. Liu, Z. Zhao, X. Zhang, S. Liu and B. Han, *Nat. Commun.*, 2019, **10**, 677.
- 167 J. Duan, T. Liu, Y. Zhao, R. Yang, Y. Zhao, W. Wang, Y. Liu, H. Li, Y. Li and T. Zhai, *Nat. Commun.*, 2022, **13**, 2039.
- 168 A. Saxena, W. Liyanage, J. Masud, S. Kapila and M. Nath, *J. Mater. Chem. A*, 2021, **9**, 7150–7161.
- 169 S. Das, S. Senapati, G. K. Pradhan, S. Varadharajanperumal and R. Naik, *ACS Appl. Nano Mater.*, 2023, **6**, 5298–5312.
- 170 Z. Gu, N. Yang, P. Han, M. Kuang, B. Mei, Z. Jiang, J. Zhong, L. Li and G. Zheng, *Small Methods*, 2019, **3**, 1800449.
- 171 K. Jiang, Y. Huang, G. Zeng, F. M. Toma, W. A. Goddard III and A. T. Bell, *ACS Energy Lett.*, 2020, **5**, 1206–1214.
- 172 M. Li, Y. Ma, J. Chen, R. Lawrence, W. Luo, M. Sacchi, W. Jiang and J. Yang, *Angew. Chem., Int. Ed.*, 2021, **60**, 11487–11493.
- 173 S. Lee, D. Kim and J. Lee, *Angew. Chem., Int. Ed.*, 2015, **54**, 14701–14705.
- 174 T. Kim and G. T. R. Palmore, *Nat. Commun.*, 2020, **11**, 3622.
- 175 H. Mistry, A. S. Varela, C. S. Bonifacio, I. Zegkinoglou, I. Sinev, Y.-W. Choi, K. Kisslinger, E. A. Stach, J. C. Yang, P. Strasser and B. R. Cuenya, *Nat. Commun.*, 2016, **7**, 12123.
- 176 J. Fu, H. Bao, Y. Liu, Y. Mi, Y. Qiu, L. Zhuo, X. Liu and J. Luo, *Small*, 2020, **16**, 1905825.
- 177 X. Rong, H.-J. Wang, X.-L. Lu, R. Si and T.-B. Lu, *Angew. Chem., Int. Ed.*, 2020, **59**, 1961–1965.
- 178 X. Yang, P. Deng, D. Liu, S. Zhao, D. Li, H. Wu, Y. Ma, B. Y. Xia, M. Li, C. Xiao and S. Ding, *J. Mater. Chem. A*, 2020, **8**, 2472–2480.
- 179 Y. Ma, M. Chen, H. Geng, H. Dong, P. Wu, X. Li, G. Guan and T. Wang, *Adv. Funct. Mater.*, 2020, **30**, 2000561.
- 180 J. Zhang, R. Yin, Q. Shao, T. Zhu and X. Huang, *Angew. Chem., Int. Ed.*, 2019, **58**, 5609–5613.
- 181 T. Gao, A. Kumar, Z. Shang, X. Duan, H. Wang, S. Wang, S. Ji, D. Yan, L. Luo, W. Liu and X. Sun, *Chin. Chem. Lett.*, 2019, **30**, 2274–2278.
- 182 L. Cheng, Y. Li, A. Chen, Y. Zhu and C. Li, *Chem. Commun.*, 2020, **56**, 563–566.
- 183 S. B. Varandili, J. Huang, E. Oveisi, G. L. De Gregorio, M. Mensi, M. Strach, J. Vavra, C. Gadiyar, A. Bhowmik and R. Buonsanti, *ACS Catal.*, 2019, **9**, 5035–5046.
- 184 W. Zhu, L. Zhang, P. Yang, C. Hu, H. Dong, Z.-J. Zhao, R. Mu and J. Gong, *ACS Energy Lett.*, 2018, **3**, 2144–2149.
- 185 X. Ren, X. Zhang, X. Cao and Q. Wang, *J. CO<sub>2</sub> Util.*, 2020, **38**, 125–131.
- 186 D. Wu, G. Huo, W. Chen, X.-Z. Fu and J.-L. Luo, *Appl. Catal., B*, 2020, **271**, 118957.
- 187 H. He, K. Liu, K. Liang, A. Mustapha, Z. Wang, L. Wu, C. Yang, L. Deng, S. Guo and Y.-N. Liu, *J. Catal.*, 2020, **385**, 246–254.
- 188 A. Yoon, J. Poon, P. Grosse, S. W. Chee and B. R. Cuenya, *J. Mater. Chem. A*, 2022, **10**, 14041–14050.
- 189 H. Li, T. Liu, P. Wei, L. Lin, D. Gao, G. Wang and X. Bao, *Angew. Chem., Int. Ed.*, 2021, **60**, 14329–14333.
- 190 R. Cai, M. Sun, J. Ren, M. Ju, X. Long, B. Huang and S. Yang, *Chem. Sci.*, 2021, **12**, 15382–15388.
- 191 P. Li, J. Bi, J. Liu, Q. Zhu, C. Chen, X. Sun, J. Zhang and B. Han, *Nat. Commun.*, 2022, **13**, 1965.
- 192 X. Tan, C. Yu, C. Zhao, H. Huang, X. Yao, X. Han, W. Guo, S. Cui, H. Huang and J. Qiu, *ACS Appl. Mater. Interfaces*, 2019, **11**, 9904–9910.
- 193 Q. Zhu, X. Sun, D. Yang, J. Ma, X. Kang, L. Zheng, J. Zhang, Z. Wu and B. Han, *Nat. Commun.*, 2019, **10**, 3851.
- 194 S. Lee, G. Park and J. Lee, *ACS Catal.*, 2017, **7**, 8594–8604.
- 195 J. Wu, F. G. Risalvato, S. Ma and X.-D. Zhou, *J. Mater. Chem. A*, 2014, **2**, 1647–1651.
- 196 W. Zhang, Q. Qin, L. Dai, R. Qin, X. Zhao, X. Chen, D. Ou, J. Chen, T. T. Chuong, B. Wu and N. Zheng, *Angew. Chem., Int. Ed.*, 2018, **57**, 9475–9479.
- 197 S. Huo, Z. Weng, Z. Wu, Y. Zhong, Y. Wu, J. Fang and H. Wang, *ACS Appl. Mater. Interfaces*, 2017, **9**, 28519–28526.
- 198 K. Wang, D. Liu, P. Deng, L. Liu, S. Lu, Z. Sun, Y. Ma, Y. Wang, M. Li, B. Y. Xia, C. Xiao and S. Ding, *Nano Energy*, 2019, **64**, 103954.
- 199 X. Bai, J. Han, S. Chen, X. Niu and J. Guan, *Chin. J. Catal.*, 2023, **54**, 212–219.
- 200 X. Bai, J. Han, X. Niu and J. Guan, *Nano Res.*, 2023, **16**, 10796–10802.
- 201 Q. Wang, K. Liu, J. Fu, C. Cai, H. Li, Y. Long, S. Chen, B. Liu, H. Li, W. Li, X. Qiu, N. Zhang, J. Hu, H. Pan and M. Liu, *Angew. Chem., Int. Ed.*, 2021, **60**, 25241–25245.
- 202 C. Zhao, X. Dai, T. Yao, W. Chen, X. Wang, J. Wang, J. Yang, S. Wei, Y. Wu and Y. Li, *J. Am. Chem. Soc.*, 2017, **139**, 8078–8081.
- 203 Y. Zhang, L. Jiao, W. Yang, C. Xie and H.-L. Jiang, *Angew. Chem., Int. Ed.*, 2021, **60**, 7607–7611.
- 204 X. Li, S. Xi, L. Sun, S. Dou, Z. Huang, T. Su and X. Wang, *Adv. Sci.*, 2020, **7**, 2001545.
- 205 J. Gu, C.-S. Hsu, L. Bai, H. M. Chen and X. Hu, *Science*, 2019, **364**, 1091–1094.



- 206 H. B. Yang, S.-F. Hung, S. Liu, K. Yuan, S. Miao, L. Zhang, X. Huang, H.-Y. Wang, W. Cai, R. Chen, J. Gao, X. Yang, W. Chen, Y. Huang, H. M. Chen, C. M. Li, T. Zhang and B. Liu, *Nat. Energy*, 2018, **3**, 140–147.
- 207 X. Chen, D.-D. Ma, B. Chen, K. Zhang, R. Zou, X.-T. Wu and Q.-L. Zhu, *Appl. Catal., B*, 2020, **267**, 118720.
- 208 F. Yang, P. Song, X. Liu, B. Mei, W. Xing, Z. Jiang, L. Gu and W. Xu, *Angew. Chem., Int. Ed.*, 2018, **57**, 12303–12307.
- 209 J. Liu, X. Kong, L. Zheng, X. Guo, X. Liu and J. Shui, *ACS Nano*, 2020, **14**, 1093–1101.
- 210 T. Tang, Y. Wang, J. Han, Q. Zhang, X. Bai, X. Niu, Z. Wang and J. Guan, *Chin. J. Catal.*, 2023, **46**, 48–55.
- 211 J. Han and J. Guan, *Chin. J. Catal.*, 2023, **47**, 1–31.
- 212 T. Tang, Z. Duan, D. Baimanov, X. Bai, X. Liu, L. Wang, Z. Wang and J. Guan, *Nano Res.*, 2023, **16**, 2218–2223.
- 213 Y. Wang, L. Cao, N. J. Libretto, X. Li, C. Li, Y. Wan, C. He, J. Lee, J. Gregg, H. Zong, D. Su, J. T. Miller, T. Mueller and C. Wang, *J. Am. Chem. Soc.*, 2019, **141**, 16635–16642.
- 214 N. Zhang, X. Zhang, Y. Kang, C. Ye, R. Jin, H. Yan, R. Lin, J. Yang, Q. Xu, Y. Wang, Q. Zhang, L. Gu, L. Liu, W. Song, J. Liu, D. Wang and Y. Li, *Angew. Chem., Int. Ed.*, 2021, **60**, 13388–13393.
- 215 Y. Li, C. Chen, R. Cao, Z. Pan, H. He and K. Zhou, *Appl. Catal., B*, 2020, **268**, 118747.
- 216 J. Jiao, R. Lin, S. Liu, W.-C. Cheong, C. Zhang, Z. Chen, Y. Pan, J. Tang, K. Wu, S.-F. Hung, H. M. Chen, L. Zheng, Q. Lu, X. Yang, B. Xu, H. Xiao, J. Li, D. Wang, Q. Peng, C. Chen and Y. Li, *Nat. Chem.*, 2019, **11**, 222–228.
- 217 Y. Wang, B. J. Park, V. K. Paidi, R. Huang, Y. Lee, K.-J. Noh, K.-S. Lee and J. W. Han, *ACS Energy Lett.*, 2022, **7**, 640–649.
- 218 T. Ding, X. Liu, Z. Tao, T. Liu, T. Chen, W. Zhang, X. Shen, D. Liu, S. Wang, B. Pang, D. Wu, L. Cao, L. Wang, T. Liu, Y. Li, H. Sheng, M. Zhu and T. Yao, *J. Am. Chem. Soc.*, 2021, **143**, 11317–11324.
- 219 A. S. Varela, N. Ranjbar Sahraie, J. Steinberg, W. Ju, H.-S. Oh and P. Strasser, *Angew. Chem., Int. Ed.*, 2015, **54**, 10758–10762.
- 220 Y. Li, B. Wei, M. Zhu, J. Chen, Q. Jiang, B. Yang, Y. Hou, L. Lei, Z. Li, R. Zhang and Y. Lu, *Adv. Mater.*, 2021, **33**, 2102212.
- 221 L. Jiao, J. Zhu, Y. Zhang, W. Yang, S. Zhou, A. Li, C. Xie, X. Zheng, W. Zhou, S.-H. Yu and H.-L. Jiang, *J. Am. Chem. Soc.*, 2021, **143**, 19417–19424.
- 222 Z. Pei, H. Zhang, Z.-P. Wu, X. Feng Lu, D. Luan and X. W. D. Lou, *Sci. Adv.*, 2023, **9**, eadh1320.
- 223 T. Tang, Z. Wang and J. Guan, *Adv. Funct. Mater.*, 2022, **32**, 2111504.
- 224 L. Lin, H. Li, C. Yan, H. Li, R. Si, M. Li, J. Xiao, G. Wang and X. Bao, *Adv. Mater.*, 2019, **31**, 1903470.
- 225 D. Yao, C. Tang, X. Zhi, B. Johannessen, A. Slattery, S. Chern and S. Z. Qiao, *Adv. Mater.*, 2023, **35**, 2209386.
- 226 H. Shang, T. Wang, J. Pei, Z. Jiang, D. Zhou, Y. Wang, H. Li, J. Dong, Z. Zhuang, W. Chen, D. Wang, J. Zhang and Y. Li, *Angew. Chem., Int. Ed.*, 2020, **59**, 22465–22469.
- 227 X. Zu, X. Li, W. Liu, Y. Sun, J. Xu, T. Yao, W. Yan, S. Gao, C. Wang, S. Wei and Y. Xie, *Adv. Mater.*, 2019, **31**, 1808135.
- 228 P. Huang, M. Cheng, H. Zhang, M. Zuo, C. Xiao and Y. Xie, *Nano Energy*, 2019, **61**, 428–434.
- 229 S. Chen, B. Wang, J. Zhu, L. Wang, H. Ou, Z. Zhang, X. Liang, L. Zheng, L. Zhou, Y.-Q. Su, D. Wang and Y. Li, *Nano Lett.*, 2021, **21**, 7325–7331.
- 230 Y. Wang, Z. Chen, P. Han, Y. Du, Z. Gu, X. Xu and G. Zheng, *ACS Catal.*, 2018, **8**, 7113–7119.
- 231 J.-C. Jiang, J.-C. Chen, M.-D. Zhao, Q. Yu, Y.-G. Wang and J. Li, *Nano Res.*, 2022, **15**, 7116–7123.
- 232 T. Zheng, C. Liu, C. Guo, M. Zhang, X. Li, Q. Jiang, W. Xue, H. Li, A. Li, C.-W. Pao, J. Xiao, C. Xia and J. Zeng, *Nat. Nanotechnol.*, 2021, **16**, 1386–1393.
- 233 H. Shen, T. Wang, H. Jiang, P. Zhao, Z. Chen, Y. Feng, Y. Cao, Y. Guo, Q. Zhang and H. Zhang, *Appl. Catal., B*, 2023, **339**, 123140.
- 234 D. Wang, R. Cao, S. Hao, C. Liang, G. Chen, P. Chen, Y. Li and X. Zou, *Green Energy Environ.*, 2023, **8**, 820–830.
- 235 W. Wu, J. Zhu, Y. Tong, S. Xiang and P. Chen, *Nano Res.*, 2024, **17**, 3684–3692.
- 236 M. G. Kim, J. Park, Y. Choi, H. C. Song, S. H. Kim, K. M. Bang, H. C. Ham, N. K. Kim, D. H. Won, B. K. Min, S. J. Yoo and W. Kim, *Adv. Energy Mater.*, 2023, **13**, 2300749.
- 237 V. Okatenko, A. Loiudice, M. A. Newton, D. C. Stoian, A. Blokhina, A. N. Chen, K. Rossi and R. Buonsanti, *J. Am. Chem. Soc.*, 2023, **145**, 5370–5383.
- 238 Y. Chen, N. Lyu, J. Zhang, S. Yan, C. Peng, C. Yang, X. Lv, C. Hu, M. Kuang and G. Zheng, *Small*, 2023, **2308004**, DOI: [10.1002/smll.202308004](https://doi.org/10.1002/smll.202308004).
- 239 L. Xiao, Z. Wang and J. Guan, *Chem. Sci.*, 2023, **14**, 12850–12868.
- 240 S. Nellaiappan, N. K. Katiyar, R. Kumar, A. Parui, K. D. Malviya, K. G. Pradeep, A. K. Singh, S. Sharma, C. S. Tiwary and K. Biswas, *ACS Catal.*, 2020, **10**, 3658–3663.
- 241 J. Cavin, A. Ahmadiparidari, L. Majidi, A. S. Thind, S. N. Misal, A. Prajapati, Z. Hemmat, S. Rastegar, A. Beukelman, M. R. Singh, K. A. Unocic, A. Salehi-Khojin and R. Mishra, *Adv. Mater.*, 2021, **33**, 2100347.
- 242 D. Roy, S. C. Mandal and B. Pathak, *J. Phys. Chem. Lett.*, 2022, **13**, 5991–6002.
- 243 H. Tian, T. Wang, F. Zhang, S. Zhao, S. Wan, F. He and G. Wang, *J. Mater. Chem. A*, 2018, **6**, 12816–12841.
- 244 Z. Zhang, Z. P. Cano, D. Luo, H. Dou, A. Yu and Z. Chen, *J. Mater. Chem. A*, 2019, **7**, 20985–21003.
- 245 M. K. Aslam, K. Yang, S. Chen, Q. Li and J. Duan, *EES Catal.*, 2023, **1**, 179–229.
- 246 D. Yang and B. C. Gates, *ACS Catal.*, 2019, **9**, 1779–1798.
- 247 J. Li, H. Luo, B. Li, J.-G. Ma and P. Cheng, *Mater. Chem. Front.*, 2023, **7**, 6107–6129.
- 248 Z. Li, M. Song, W. Zhu, W. Zhuang, X. Du and L. Tian, *Coord. Chem. Rev.*, 2021, **439**, 213946.
- 249 T. A. Al-Attas, N. N. Marei, X. Yong, N. G. Yasri, V. Thangadurai, G. Shimizu, S. Siahrostami and M. G. Kibria, *ACS Catal.*, 2021, **11**, 7350–7357.
- 250 Y. Guo, H. Yang, X. Zhou, K. Liu, C. Zhang, Z. Zhou, C. Wang and W. Lin, *J. Mater. Chem. A*, 2017, **5**, 24867–24873.



- 251 Y. Ye, F. Cai, H. Li, H. Wu, G. Wang, Y. Li, S. Miao, S. Xie, R. Si, J. Wang and X. Bao, *Nano Energy*, 2017, **38**, 281–289.
- 252 C. Hu, S. Bai, L. Gao, S. Liang, J. Yang, S.-D. Cheng, S.-B. Mi and J. Qiu, *ACS Catal.*, 2019, **9**, 11579–11588.
- 253 C. W. Lee, K. D. Yang, D. H. Nam, J. H. Jang, N. H. Cho, S. W. Im and K. T. Nam, *Adv. Mater.*, 2018, **30**, 1704717.
- 254 J. Wang, Y. Chen, S. Zhang, C. Yang, J. Y. Zhang, Y. Su, G. Zheng and X. Fang, *Small*, 2022, **18**, 2202238.
- 255 W. Xiong, D. Si, J. Yi, Y. Huang, H. Li and R. Cao, *Appl. Catal., B*, 2022, **314**, 121498.
- 256 Y. J. Jang, J. Lee, J. H. Kim, B. J. Lee and J. S. Lee, *J. Power Sources*, 2018, **378**, 412–417.
- 257 X. Ma, J. Tian, M. Wang, X. Jin, M. Shen and L. Zhang, *Catal. Sci. Technol.*, 2021, **11**, 6096–6102.
- 258 C. Liu, X.-D. Zhang, J.-M. Huang, M.-X. Guan, M. Xu and Z.-Y. Gu, *ACS Catal.*, 2022, **12**, 15230–15240.
- 259 L. Li, Z. Jiang, Y. Li, F. Li, Y. Pan, X. Zhang, Y. Liang and Z. Zheng, *Small Methods*, 2022, **7**, 2201213.
- 260 Q.-H. Zheng, C. Chen, S.-M. Cao, M.-T. Peng, B.-X. Dong and Y.-L. Teng, *Chin. Chem. Lett.*, 2023, **34**, 107273.
- 261 I. Hod, M. D. Sampson, P. Deria, C. P. Kubiak, O. K. Farha and J. T. Hupp, *ACS Catal.*, 2015, **5**, 6302–6309.
- 262 C.-W. Kung, C. O. Audu, A. W. Peters, H. Noh, O. K. Farha and J. T. Hupp, *ACS Energy Lett.*, 2017, **2**, 2394–2401.
- 263 P. C. Adrien, A. I. Benin, N. W. Ockwig, M. O'Keeffe, A. J. Matzger and O. M. Yaghi, *Science*, 2005, **310**, 1166–1170.
- 264 L. Xiao, Z. Wang and J. Guan, *Adv. Funct. Mater.*, 2024, **34**, 2310195.
- 265 H.-J. Zhu, M. Lu, Y.-R. Wang, S.-J. Yao, M. Zhang, Y.-H. Kan, J. Liu, Y. Chen, S.-L. Li and Y.-Q. Lan, *Nat. Commun.*, 2020, **11**, 497.
- 266 Y. Yue, P. Cai, K. Xu, H. Li, H. Chen, H.-C. Zhou and N. Huang, *J. Am. Chem. Soc.*, 2021, **143**, 18052–18060.
- 267 X.-F. Qiu, J.-R. Huang, C. Yu, Z.-H. Zhao, H.-L. Zhu, Z. Ke, P.-Q. Liao and X.-M. Chen, *Angew. Chem., Int. Ed.*, 2022, **61**, e202206470.
- 268 A. Schneemann, R. Dong, F. Schwotzer, H. Zhong, I. Senkowska, X. Feng and S. Kaskel, *Chem. Sci.*, 2021, **12**, 1600–1619.
- 269 M. Liu, S. Liu, Q. Xu, Q. Miao, S. Yang, S. Hanson, G. Z. Chen, J. He, Z. Jiang and G. Zeng, *Carbon Energy*, 2023, **5**, 1–12.
- 270 S. B. Alahakoon, K. Tan, H. Pandey, S. D. Diwakara, G. T. McCandless, D. I. Grinffiel, A. Durand-Silva, T. Thonhauser and R. A. Smaldone, *J. Am. Chem. Soc.*, 2020, **142**, 12987–12994.
- 271 M. Li, B. Han, S. Li, Q. Zhang, E. Zhang, L. Gong, D. Qi, K. Wang and J. Jiang, *Small*, 2024, 2310147, DOI: [10.1002/sml.202310147](https://doi.org/10.1002/sml.202310147).
- 272 Q. Wu, R.-K. Xie, M.-J. Mao, G.-L. Chai, J.-D. Yi, S.-S. Zhao, Y.-B. Huang and R. Cao, *ACS Energy Lett.*, 2020, **5**, 1005–1012.
- 273 R. Matheu, E. Gutierrez-Puebla, M. A. Monge, C. S. Diercks, J. Kang, M. S. Prévot, X. K. Pei, N. Hanikel, B. Zhang, P. D. Yang and O. M. Yaghi, *J. Am. Chem. Soc.*, 2019, **141**, 17081–17085.
- 274 B. Han, Y. Jin, B. Chen, W. Zhou, B. Yu, C. Wei, H. Wang, K. Wang, Y. Chen, B. Chen and J. Jiang, *Angew. Chem., Int. Ed.*, 2022, **61**, e202114244.
- 275 S.-Y. Chi, Q. Chen, S.-S. Zhao, D.-H. Si, Q.-J. Wu, Y.-B. Huang and R. Cao, *J. Mater. Chem. A*, 2022, **10**, 4653–4659.
- 276 H. Shin, K. U. Hansen and F. Jiao, *Nat. Sustain.*, 2021, **4**, 911–919.
- 277 W. Lai, Y. Qiao, J. Zhang, Z. Lin and H. Huang, *Energy Environ. Sci.*, 2022, **15**, 3603–3629.
- 278 I. E. L. Stephens, K. Chan, A. Bagger, S. W. Boettcher, J. Bonin, E. Boutin, A. K. Buckley, R. Buonsanti, E. R. Cave, X. Chang, S. W. Chee, A. H. M. da Silva, P. de Luna, O. Einsle, B. Endrődi, M. Escudero-Escribano, J. V. Ferreira de Araujo, M. C. Figueiredo, C. Hahn, K. U. Hansen, S. Haussener, S. Hunegnaw, Z. Huo, Y. J. Hwang, C. Janáky, B. S. Jayathilake, F. Jiao, Z. P. Jovanov, P. Karimi, M. T. M. Koper, K. P. Kuhl, W. H. Lee, Z. Liang, X. Liu, S. Ma, M. Ma, H.-S. Oh, M. Robert, B. R. Cuenya, J. Rossmeisl, C. Roy, M. P. Ryan, E. H. Sargent, P. Sebastián-Pascual, B. Seger, L. Steier, P. Strasser, A. S. Varela, R. E. Vos, X. Wang, B. Xu, H. Yadegari and Y. Zhou, *JPhys Energy*, 2022, **4**, 042003.
- 279 C. Ampelli, F. Tavella, D. Giusi, A. M. Ronsisvalle, S. Perathoner and G. Centi, *Catal. Today*, 2023, **421**, 114217.
- 280 N. Fujinuma, A. Ikoma and S. E. Lofland, *Adv. Energy Mater.*, 2020, **10**, 2001645.
- 281 S. Liang, N. Altaf, L. Huang, Y. Gao and Q. Wang, *J. CO<sub>2</sub> Util.*, 2020, **35**, 90–105.
- 282 Q. Chen, X. Wang, Y. Zhou, Y. Tan, H. Li, J. Fu and M. Liu, *Adv. Mater.*, 2023, **36**, 2303902.
- 283 D. A. Salvatore, C. M. Gabardo, A. Reyes, C. P. O'Brien, S. Holdcroft, P. Pintauro, B. Bahar, M. Hickner, C. Bae, D. Sinton, E. H. Sargent and C. P. Berlinguette, *Nat. Energy*, 2021, **6**, 339–348.
- 284 D. Gao, P. Wei, H. Li, L. Lin, G. Wang and X. Bao, *Acta Phys.-Chim. Sin.*, 2020, 2009021.
- 285 Y. Meng, H. Huang, Y. Zhang, Y. Cao, H. Lu and X. Li, *Front. Chem.*, 2023, **11**, 1172146.
- 286 H. Cao, Z. Zhang, J.-W. Chen and Y.-G. Wang, *ACS Catal.*, 2022, **12**, 6606–6617.

